Excess Noise of Amorphous Selenium Used in X-ray Detectors

A Thesis Submitted to the

College of Graduate Studies and Research

in Partial Fulfillment of the Requirements

for the degree of Doctor of Philosophy

in the Department of Electrical and Computer Engineering

University of Saskatchewan

Saskatoon

By

Shaikh Hasibul Majid

Permission to Use

In presenting this thesis in partial fulfilment of the requirements for a Postgraduate degree from the University of Saskatchewan, I agree that the Libraries of this University may make it freely available for inspection. I further agree that permission for copying of this thesis in any manner, in whole or in part, for scholarly purposes may be granted by the professor or professors who supervised my thesis work or, in their absence, by the Head of the Department or the Dean of the College in which my thesis work was done. It is understood that any copying or publication or use of this thesis or parts thereof for financial gain shall not be allowed without my written permission. It is also understood that due recognition shall be given to me and to the University of Saskatchewan in any scholarly use which may be made of any material in my thesis.

Requests for permission to copy or to make other use of material in this thesis in whole or part should be addressed to:

Head of the Department of Electrical and Computer Engineering

57 Campus Drive

University of Saskatchewan

Saskatoon, Saskatchewan

Canada

S7N 5A9

Abstract

Amorphous selenium based digital radiography has attracted much attention because of selenium's high X-ray absorption and excellent charge transport properties, and the ability to be created thick (typically 100 to 1000 μm) uniform layers over a large area (typically 30 cm $\times$ 30 cm) at low processing temperatures (typically at around 50^{o}C substrate temperature). In this work, the excess noise in amorphous selenium has been studied. A number of device parameters were altered to study the noise characteristics, such as the metal of the electrodes, bulk material composition, device volume, surface conditions and substrate temperature. All the samples had a transverse geometry with 20 to 200-μm thick layers of amorphous selenium electroded with metal at the top and at the bottom. Sample devices were fabricated by conventional vacuum deposition.

Noise power was measured over a limited bandwidth of 1 kHz. The fluctuations for one sample amounted to 1% of the bias current. The excess noise was mainly $1/f^{\alpha}$ noise with α ranging from 0.77 to 1.4. Interpretation of the noise spectra was complicated due to the samples' highly non-linear I-V relation and long time transients.

The metals of the electrode clearly showed a large effect on both the magnitude and shape of the noise spectrum. Of the metals studied, aluminum produced the least normalized noise and platinum the most. The addition of arsenic caused a decrease in the normalized noise. An additional 0.2% (% wt.) arsenic decreased the $1/f$ noise magnitude by more than a decade, but did not change the slope. The addition of chlorine did not affect the noise magnitude. Amorphous selenium is quite vulnerable to stress and in particular, external mechanical stress causes crystallization. The surface of the sample was gently abraded, applying the least possible amount of stress to the selenium layer. A change in the surface condition before the top electrode was deposited showed that a roughened surface decreased the noise magnitude substantially. These results strongly indicate that the noise is controlled by the metal-semiconductor interface.

Noise characteristics in multilayered samples were examined. The p-i-n and n-i-p structures consisted of 200 μm i-layer with 2 to 6 μm p- and n-like layers. The noise

fluctuation in the current are typical of $1/f$ noise showing a power-law spectrum with slopes between -0.9 to -1.1. These samples showed a substantial decrease in the noise power compared to single layer samples; the additional n-like and p-like layers acted as carrier sources so that the current was not controlled by the metal interface. Hence, the measurements are closer to the intrinsic noise of a-Se. After exposure to 14 R (Roentgen) of X-rays, the normalized noise decreased by a factor of 1.6 for the n-i-p structure.

Acknowledgements

I extend my sincerest gratitude towards my supervisor, Dr. Robert E. Johanson, for his patience, encouragement and the leadership throughout the course of this project. It would have been impossible for me to carry out this project without his intellectual and financial support through the entire period. I also thank Professor Safa O. Kasap for allowing me to use the experimental facilities at the Electronic Materials and Devices group, at the University of Saskatchewan, Dr. George Belev for his time to time valuable suggestions on sample deposition and dark current. My extended thanks to the members of the thesis committee, Professors Dr. Ha Nguyen and Dr. Ike Oguocha, and the external member Professor Dr. Andrei Sazonov for their valuable time. To Thomas Meyer I extend my gratitude for the help with LaTeX. This thesis would not have been possible without the financial support from the University of Saskatchewan. Finally, I would like to thank my family, especially my parents Archt. Shaikh Abdul Mazid and Mrs. Hosne Ara Begum, my wife Nadia Tahmin and our son Ayman for their outmost patience during the days of my studies. I also would like to thank my colleagues and friends, especially my ex-colleagues Dr. Z. Kabir, Mr. M. Yunus and Mr. Zahid Shakoor for their time to time support and encouragement.

To my parents,

Shaikh Abdul Mazid

and

Hosne Ara Begum

Contents

Permission to Use i

Abstract ii

Acknowledgements iv

Contents vi

List of Tables x

List of Figures xi

List of Abbreviations xvii

1 Introduction 1

1.1 Radiographic Imaging 1

1.1.1 Film Based Radiographic Imaging 2

1.1.2 Digital Radiographic Imaging 3

1.2 Principles of Radiographic Imaging 4

1.3 Flat Panel Detectors 7

1.3.1 Direct Conversion Detector 7

1.3.2 Active Matrix Readout 10

1.4 Requirements of FPDs 14

1.5 Ideal X-ray Photoconductors 14

1.6 a-Se as a Photoconductive Material 16

1.7 Other X-ray Photoconductor Materials 20

1.8 Research Objectives 21

1.8.1 Effect of metal contacts on excess noise 22

1.8.2 Effect of composition of the a-Se on excess noise 22

1.8.3 Effect of surface condition on excess noise 22
1.8.4 Effect of X-ray exposure on excess noise 23
1.8.5 Using the measurements of excess noise to calculate (SNR) of a device 23
1.9 Thesis Outline 23

2 The Physics of Amorphous Selenium 25

2.1 Introduction 25
2.2 Properties of Amorphous Semiconductors 26
2.2.1 Growth and Atomic Structure 27
2.2.2 State of Disorder 29
2.2.3 Band Theory 29
2.2.4 Density of States Model for Amorphous Selenium 33
2.2.5 Electrical Properties of Amorphous Selenium 36
2.2.6 Glass Transition Temperature 38
2.3 Stabilized Amorphous Selenium as a Glass 40
2.4 Summary 41

3 Electrical Noise 42

3.1 Sources of Electrical Noise 43
3.2 Mathematics of Noise Spectra 43
3.3 Types of Electrical Noise 46
3.3.1 Thermal Noise 46
3.3.2 Shot Noise 51
3.3.3 Random Telegraphic Noise 55
3.3.4 $1/f$ Noise 58

4 Experimental Procedure and Measurements 60

4.1 Introduction 60
4.2 Sample Preparation 61
4.2.1 Substrate Cleaning 62

4.2.2 Metal Deposition for Both the Electrodes 63
4.2.3 Deposition of Amorphous Selenium Layer 66
4.3 Circuit Analysis of the Experimental Setup 69
4.4 Noise Measurement Apparatus 72
4.4.1 High Voltage DC Source 74
4.4.2 Low-pass Butterworth Filter 76
4.4.3 High Pass Filter 77
4.4.4 Circuit elements of the filters and the sample enclosure 78
4.4.5 Current Pre-Amplifier 81
4.4.6 Voltage Pre-Amplifier 82
4.4.7 Spectrum Analyzer with Built in Anti-Aliasing Filter 83
4.4.8 Software to Collect Data and Measure Noise Spectra 86
4.5 X-ray Apparatus 86
4.6 Noise System Calibration 92
4.6.1 Response Curves 93
4.6.2 System testing with the Johnson noise of a known resistance . 97
4.6.3 Testing the system for $1/f$ noise with pure resistive load . . . 100
4.6.4 Data Analysis 101
4.6.5 Normalization 104
4.7 Summary 105

5 Results and Discussion **106**

5.1 Introduction 107
5.2 DC Measurements 109
5.2.1 Current-time (I-t) Curve 109
5.2.2 Current-voltage (I-V) Curve 111
5.2.3 Basic Characteristics of the $1/f$ Noise Spectra of a-Se 113
5.3 Non-Linearity of Noise Spectra in a-Se samples 117
5.4 Various Factors Affecting Excess Noise 120
5.4.1 Effect of Metal Contacts 120

5.4.2 Effect of the Bulk Material . . . 125
5.4.3 Thickness of the a-Se layer and effective device volume . . . 126
5.4.4 Substrate temperature . . . 133
5.4.5 Material composition . . . 135
5.4.6 Surface Effect . . . 139
5.5 Noise Behavior in Multilayer Structures . . . 143
5.6 Calculation of $1/f$ Noise Power . . . 152
5.7 SNR Calculations and the Detector Performance . . . 154
5.8 Summary . . . 155

6 Summary and Conclusions **156**

6.1 Goals . . . 156
6.2 Apparatus and Sample Preparation . . . 157
6.3 Results . . . 158
6.4 Suggestions for Future Work . . . 159
6.4.1 Other Metals Used as Electrodes . . . 160
6.4.2 Investigation of RTN . . . 160
6.4.3 Noise Measurement at Lower Frequencies . . . 160
6.4.4 Noise Measurement with X-ray Exposures . . . 161
6.4.5 Metal-Semiconductor Interface . . . 161

References **171**

List of Tables

Table 1.1 Required parameters for digital X-ray imaging systems. 14

Table 4.1 Maximum allowable number of exposure seconds in a 5 minute period. 88

Table 5.1 Dark current at different combinations of top and bottom electrodes showing the consistency of the change in dark current with the metal used for electrodes. In all the measurements, top electrodes of the samples were connected to the positive terminal of the dc supply. 124

Table 5.2 Relationship of arsenic and chlorine concentration with carrier mobility 136

List of Figures

Fig. 1.1 A traditional phosphor type X-ray system. 2

Fig. 1.2 X-ray image taken using traditional film technology (left) and using Photodetectors (right) [1]. 4

Fig. 1.3 Schematic illustration of a flat panel X-ray image detector [1]. . . 8

Fig. 1.4 Physical structure of an AMFPI with a-Se as a photoconductive layer and peripheral circuitry [Self taken picture, courtesy: ANRAD Corporation]. 9

Fig. 1.5 Thin film transistor (TFT) active matrix array (AMA) for use in X-ray image detectors with self scanned electronic readout [2]. G, S and D are the gate, source and drain of the TFT transistors. 11

Fig. 1.6 A schematic diagram of the cross sectional structure of two pixels, *(i,j)* and *(i, j+1)* of the a-Se image detector [2]. S_j is the source of (i, j)th TFT and G_j is the gate of the (i, j)th TFT. 12

Fig. 1.7 Mass attenuation and mass energy absorption coefficients of selenium for X-rays with energies from 1 keV to 20 MeV [3]. μ is the linear attenuation coefficient, μ_{en} is the energy attenuation coefficient and ρ is the material density. 17

Fig. 1.8 Electron-hole pair creation energy in a-Se for different applied fields and different beam energies [4]. 19

Fig. 2.1 Two dimensional representation of the structure of (a) a crystalline solid and (b) an amorphous solid. Atoms marked O represent over-coordinated atoms with more than usual numbers of bonding with adjacent atoms and U represent under-coordinated atoms with less than the usual number of bonds with adjacent atoms. 28

Fig. 2.2 Various stages in the development of the energy band model of amorphous semiconductors: a) Model for crystalline semiconductors, b) Model proposed by Mott, c) The Cohen, Fritzsche and Ovshinski (CFO) model, and d) The model of Marshall and Owen [5]. 31
Fig. 2.3 Density of electronic states in amorphous selenium proposed by Abkowitz 2.3. 34
Fig. 2.4 Density of electronic states in amorphous selenium proposed by Koughia 2.4. 35
Fig. 2.5 Band gap of amorphous material with an applied electric field. Drift of the carriers get affected by the shallow and the deep traps [6]. 37
Fig. 2.6 Graph showing different states of amorphous and crystalline material [7]. 39

Fig. 3.1 Johnson noise models for a physical resistor. 47
Fig. 3.2 Equivalent noise circuit of a single resistor. 48
Fig. 3.3 Steps in the development of the equation for shot noise. (a) Each electron gives rise to a current pulse, (b) An ideal pulse associated with each charge carrier and (c) The energy spectral density function. 53
Fig. 3.4 Typical RTN noise current waveform a) as observed with white noise superimposed and b) after low-pass filtering 56
Fig. 3.5 Sketch of an RTN signal [8] 56

Fig. 4.1 Schematic diagram of the evaporator unit used for metal evaporation. 63
Fig. 4.2 Schematic diagram of the sputterer used for depositing gold and platinum to prepare top and bottom electrodes. 65
Fig. 4.3 Schematic diagram of the amorphous selenium coater. 67
Fig. 4.4 Noise equivalent circuit model of the experimental setup. 69
Fig. 4.5 Simplified noise equivalent circuit model of the experimental setup. 71
Fig. 4.6 Schematic diagram of the experimental setup for noise measurement. 73

Fig. 4.7 Pictorial illustration of the bench-top experimental setup. (A) The sample holder, (B) Low noise voltage amplifier, (C) Low noise current amplifier, (D) Analog oscilloscope and (E) Spectrum Analyzer. 74

Fig. 4.8 The high voltage dc source. 75

Fig. 4.9 4-pole low pass Butterworth filter attenuating noise over 145 mHz. 76

Fig. 4.10 Sample enclosure (Uncovered). 79

Fig. 4.11 Schematic diagram of the Ithaco 564. 81

Fig. 4.12 Schematic diagram of the experimental setup for X-ray measurements on multilayer samples. 90

Fig. 4.13 Pictorial illustration of the X-ray chamber. i) The lead cabinet with the external control and the safety features, ii) The X-ray head inside the lead enclosure. 91

Fig. 4.14 Response curve of the EG&G 5182 amplifier at 10^8 V/A low noise setting, curve (A) no extra input capacitance, and curve (B) with 1nF input capacitance. 95

Fig. 4.15 Response curve of the Ithaco 564 current amplifier with 10^7 V/A gain setting. 95

Fig. 4.16 Response curve of the current amplifier set to the gain of 10^8 V/A. 96

Fig. 4.17 Noise floor of the *EG&G* 5182 at 10^8 V/A low noise setting. . . 98

Fig. 4.18 Measured Johnson noise power of a 90KΩ wire-wound resistor. (A) With amplifier response, and (B) without amplifier response. . . 99

Fig. 4.19 Measured Johnson noise power of a 90KΩ wire-wound resistor with the linear fit showing a straight line of 0.006 slope at 1.7×10^{-25} A^2/Hz. 100

Fig. 4.20 Current noise spectra showing the Johnson noise along with $1/f$ noise from 500 V and 2000 V biasing. 102

Fig. 4.21 Normalized noise spectra showing the linearity of $1/f$ noise after normalization at 500 V and 200 V biasing. 103

Fig. 5.1 Current drift after applying various bias voltages to a-Se photodetector sample with Au top and bottom electrodes. Material composition of this sample is a-Se with 0.5% As and 10ppm Cl and the sample thickness is 30 μm. Top electrode is biased with positive voltages. At a low applied electric field the decay of current is much lower than that of at high applied electric field. 110

Fig. 5.2 I-V relation for a-Se. Data was obtained by taking the time slice from Figure 5.1, at 10 s, 100 s and 1000 s. 112

Fig. 5.3 Current noise power spectra at room temperature showing $1/f$ noise of a measured slope $\alpha = 1.07$ with 10 V/μm electric field. Measured dark current is 51.7 nA. Both the top and bottom electrodes are sputtered gold. A positive dc voltage was applied at the top electrode. 115

Fig. 5.4 Noise power as a function of dark current. The sample is 20 μm thick with gold top electrode and aluminum bottom electrode. Slope of each set has been indicated as b. 118

Fig. 5.5 Noise power density spectra for a-Se sample with two different bias voltage. (a) Un normalized spectra showing Johnson noise, and (b) Normalized spectra. The sample is 60 μm thick with platinum top and bottom electrode. 119

Fig. 5.6 The dark current vs. electric field for four different types of metal combinations for top and bottom electrodes. Name of the metal stated in the left hand side is the top electrode. In all four cases a positive dc bias is applied at the top electrode. 122

Fig. 5.7 Normalized noise power spectrum with different metal contacts. (A) Top electrode is Al, (B) Top electrode is Au and (C) Top electrode is Pt. All three bottom electrodes are Al. The samples are 100 μm thick. A constant applied field of 4 V/μm was applied for all the measurements. Changes in noise magnitude and the slope are observed with different metals. 123

Fig. 5.8 Normalized noise spectra showing dependence on thickness with platinum electrodes. Samples were deposited in three separate depositions. All other deposition parameters except the deposition thickness was kept constant. Both top and bottom electrodes of each sample are platinum. Top electrode was biased with a positive voltage. . . . 128

Fig. 5.9 Normalized noise spectra showing dependence on thickness with gold electrodes. Samples were deposited in three separate depositions. All other deposition parameters except the deposition thickness was kept constant. Both top and bottom electrodes of each sample are gold. Top electrode was biased with a positive voltage. 129

Fig. 5.10 Normalized noise power spectral density with platinum electrodes of different size. The sample is 60 μm thick. Both top and bottom electrodes are platinum. Alloy composition of the bulk material is 0.5% As and 40 ppm Cl. 132

Fig. 5.11 Normalized noise spectra at 800 V and 1200 V biasing on two different amorphous selenium samples deposited at 50°C (Sample A) and 70°C (Sample B). Both the samples are 60 μm thick with gold top and bottom electrodes. 134

Fig. 5.12 Normalized noise spectra of two different samples with variation in arsenic concentration keeping the chlorine concentration constant. Both the samples are 60 μm thick with gold top and bottom electrodes. 137

Fig. 5.13 Normalized noise spectra of two different samples with the variations in chlorine concentration. Both the samples are 60 μm thick with gold top and bottom electrodes. Positive voltage were applied at the top electrodes. 138

Fig. 5.14 Normalized noise power spectra of a-Se sample with Rough surface and Regular as-deposited surface. One half of the top surface of the sample was roughened with 800 grade sand-paper and then both the top electrodes were deposited. 141

Fig. 5.15 Normalized noise power with two different biasing voltages at two different surface conditions. In both the cases the surface conditions were altered with sand paper by applying the least possible stress on the surface to prevent further crystallization of the surface. Samples are 100 μm thick with both gold electrodes. 142

Fig. 5.16 Normalized noise power spectral density showing the difference in magnitude at different types of multilayered structure. In all the samples the intrinsic a-Se layers are 100 μm thick. In the multilayered structures the top electrodes are made with aluminum and chromium, and the bottom electrodes are made with indium-tin-oxide (ITO). Positive voltages were applied at the top electrodes. 145

Fig. 5.17 Normalized noise power spectral density plot of n-i-p and p-i-n structures. For the n-i-p structure, the top electrode is deposited on top of n-like a-Se layer and for the p-i-n structure, the top electrode is deposited on top of the p-like layer. Thickness of the intrinsic layer is approximately 200 μm, while the n- and p- like layers are less than 10 μm thick. 146

Fig. 5.18 Plots of measured Johnson noise, measured excess noise and calculated shot noise for a multilayer sample. In this figure the sample is a p-i-n device. 148

Fig. 5.19 Normalized noise spectra of a p-i-n detector showing the effect of X-ray. 14 R of X-ray was exposed for a period of 5 minutes before the noise measurements were done. 149

Fig. 5.20 Normalized noise spectra of an n-i-p detector showing the effect of X-ray. 14 R of X-ray was exposed for a period of 5 minutes before the noise data were obtained. 150

Fig. 5.21 Noise power spectral density of a sample where the dark current is 192 nA. The sample is 60 μ thick with aluminum top and bottom electrodes. 152

List of Abbreviations

a-Se	Amorphous Selenium
a-Si	Amorphous Silicon
a-Si:H	Hydrogenated Amorphous Silicon
AMA	Active Matrix Array
AMFPI	Active Matrix Flat Panel Imager
B	Bandwidth
BNC	Bayonet Neill-Concelman, a regular coaxial cable connector
CCD	Charge Coupled Device
CVD	Chemical Vapor Deposition
CZT	Cadmium Zinc Telluride
DC	Direct current
DOS	Density of States
DR	Digital Radiography
EHP	Electron Hole Pair
FFT	Fast Fourier Transform
FPD	Flat Panel Detector
GPIB	General Purpose Interface Bus
HD	High Density
ITO	Indium-tin-oxide
kV_p	Kilo volts peak
LPF	Low pass filter
LW	Line Width of the FFT
PD	Photo Detector
pixel	Picture Element
ppm	Parts Per Million
poly	Poly-crystalline
PSD	Power Spectral Density
R	Roentgen
RTN	Random Telegraphic Noise
SHVC	Semi High Voltage Connector
SNR	Signal to Noise Ratio
T_g	Glass Transition Temperature
TFT	Thin Film Transistor

Chapter 1
Introduction

This thesis involves measurement and analysis of excess noise in the stabilized amorphous selenium (a-Se) photoconductive layer used in a Flat Panel Detector (FPD), a part of the X-ray imaging system of Digital Radiography (DR). The material structure of amorphous selenium is unstable and gets crystallized with environmental parameters such as, ambient temperature, and needs to be stabilized to maintain its amorphous state. In order to stabilize amorphous selenium a few percentage of arsenic is added. Stabilized amorphous selenium is widely used in direct-conversion FPDs. This chapter presents the fundamentals of digital radiography, materials used for the FPDs and their properties. In the concluding part, the objectives of this research work are described followed by the outline of this thesis.

1.1 Radiographic Imaging

The usefulness of X-rays for medical imaging and diagnostics was appreciated soon after its discovery by Wilhelm Roentgen in 1895 and led to the development of a new branch of medical sciences known as Diagnostic Radiology. Radiology is still a rapidly developing field of medical diagnostics. Nowadays, the field of X-ray

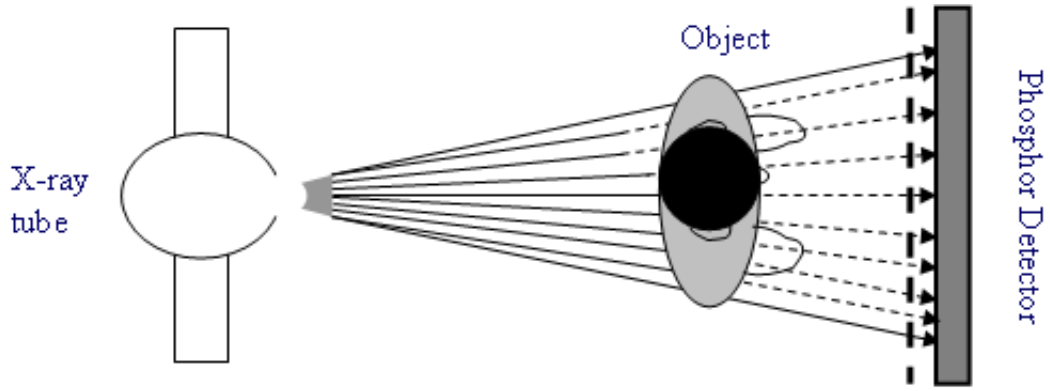

Figure 1.1: A traditional phosphor type X-ray system.

imaging is being researched and implemented in different ways, namely, conventional film based X-ray technology, direct and indirect digital X-ray technologies. One area of current development is the image acquisition system which has resulted in high quality images containing information not only about the topology of different organs inside the patients body but also about their functions. Diagnosis of some parts of the body requires X-ray images with high contrast due to similar mass density of tissues. Digital radiography has been successfully producing high-contrast images with a low dose of X-ray. The motion of different organs as well as the motion and the position of medical instruments inserted inside the human body can also be observed with the help of real time data streaming (image data) from a Digital Radiography system.

1.1.1 Film Based Radiographic Imaging

Currently, most X-ray imaging systems rely on a film-based technology; however, new technology is being developed that offers several advantages.

Figure 1.1 shows a conventional phosphor screen film based technology. The conventional detector consists of a cassette of photographic film held in position just behind a light emitting phosphor screen. X-rays impinging on the screen give off light that exposes the film creating a latent image that is subsequently made permanent by a chemical development process. The main disadvantages of this traditional system are:

1. A higher than necessary dose of X-rays due to inefficiencies

2. Limited image quality due to the limitation of a high contrast ratio

3. Delay between exposure and obtaining the image due to processing of the film

X-rays, like any other form of ionizing radiations, are harmful to the human body and exposure to X-rays must be limited.

1.1.2 Digital Radiographic Imaging

Digital radiography offers the potential of improved image quality with a low dose of X-rays as well as providing opportunities for better image management, computer-aided diagnosis, and teleradiology. For a digital system, image quality is determined by the pixel size and the bit-depth which can be engineered to be optimal for a particular application. A comparison of image quality between the conventional film based X-ray image and that of a digital X-ray image is shown in Figure 1.2. Both images are highly comparable, and are sufficient to be used for medical diagnosis. The main advantage of the direct conversion detectors, i.e. detectors that convert

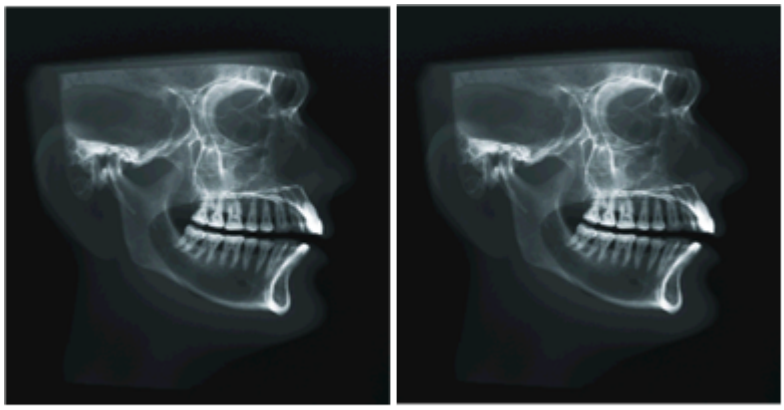

Figure 1.2: X-ray image taken using traditional film technology (left) and using Photodetectors (right) [1].

X-rays directly to electrical signals, is that these detectors have the potential to be more efficient than films leading to a lower dose to the patient.

Acquiring images in digital form has benefits such as Direct Computed Tomography, ease of storage in digital form, digital processing and manipulation of images, and ease of transmitting images from one location to another over communications networks.

1.2 Principles of Radiographic Imaging

To understand the basic principle of radiographic imaging, we have to go back to the traditional phosphor-based medical imaging system. This projection radiography is still the most commonly used medical imaging system. A typical radiographic measurement is shown in Figure 1.3 where the incident X-ray radiation from an X-ray tube forms a nearly-parallel beam. The object is then exposed to the beam and a part of the X-ray beam passes through the object onto the detector. The

detector then stores the information until the image is developed. In the traditional system, the detector is a photographic film. Ordinary photographic film consists of an emulsion of silver halide grains suspended in a gelatin matrix and supported with a backing of glass or cellulose acetate film.

In X-radiography, the transmitted high-energy photons must interact with the electrons of the inner shells (k th and l th shell electrons) of the atoms of the photoconductor to generate secondary electrons. The secondary charge carriers need to be collected at the charge collection electrodes of the flat panel detectors. The direct interaction probability of an X-ray photon within the emulsion itself is usually no more than a few percent. Therefore, these films are relatively insensitive to this radiation. At low exposures the emulsion remains under-exposed and, therefore, makes it difficult to build a system that is workable at lower doses of X-ray. By using a phosphor to convert the X-ray photons to visible light photons efficiency is greatly increased due to the film's greater sensitivity to visible wavelengths. However, there are problems with this system such as the quantum efficiency of the phosphor and a loss of resolution.

Nowadays, about 65% of X-ray imaging [6] is accomplished with film/screen systems. The cassettes are loaded with films and taken to the X-ray equipment in the examination room, and after exposure they are returned to the darkroom for development before a final image can be viewed. This is time consuming, where as the digital imaging system is a real time imaging system which gives the images instantly.

An ideal X-ray diagnostic system would permit the instantaneous acquisition of

an X-ray image in digital form with the use of the theoretical minimum number of X-ray photons. There are transitional digital systems based on the use of photo-stimulable phosphor plates optically coupled to electronic imager, such as a vidicon tube or a Charge Coupled Device (CCDs) [1]. With photo-stimulable plate systems, the X-ray image is captured on the plate, which is then scanned by a laser system in order to digitize the image information. This is just as time consuming as a conventional film-based system. With a vidicon image intensifier, the image is obtained instantaneously but the image quality for radiography is worse than that of a film-based system. Further, this system is bulky and extremely expensive. The basis of an optically coupled CCD system involves the use of a structured screen which is able to detect X-rays, converting them to light which in turn is collected by trapped optical fibers. This reduces the image size by a factor of 2 to 4 and matches the size of the CCD array - typically no larger than 2×2 cm - to the required field of view of the clinical task [2]. Thus, for fields of view larger than 10×10 cm, several CCDs must be used together in order to obtain a detector of sufficient size for many clinical studies.

There is still a need for a better digital X-ray imaging system meeting the following important requirements:

1. It should require a reduced X-ray exposure.

2. It should produce high quality images with the highest accuracy and almost immediately so that it can be used for real-time imaging.

3. It should be low cost.

4. It should be able to be conveniently incorporated into existing medical systems.

5. It should be able to record the X-ray image directly to a computer where it could be read, stored, and transmitted to a distant place using the Internet.

1.3 Flat Panel Detectors

It is believed that all properties of ideal digital X-ray imaging can be achieved using a flat panel X-ray image detector. In the recent years, extensive research has shown that the large area thin-film transistor based FPD is the most promising digital radiographic technique. This technique uses the self scanned active matrix array (AMA) and is quite suitable to replace the conventional film cassettes [1, 6, 9].

1.3.1 Direct Conversion Detector

As with any medical X-ray imager, the patient is exposed to X-rays, which then incident on the flat panel detector. The FPD sensor and a computer essentially retrofits the normal cassette film and the phosphor screen.

A typical Active Matrix Flat Panel Imager (AMFPI) is illustrated in Figure 1.3 where X-rays passing through a human body are incident on a large area flat panel sensor. The AMFPI consists of millions of pixels each of which acts as an individual detector. In a direct conversion detector, X-rays are directly converted to charge by an X-ray photoconductor and the charge is collected and measured. A typical direct conversion detector using amorphous selenium as the photoconductor is shown in Figure 1.4 [10]. The amount of charge produced in each pixel is proportional to

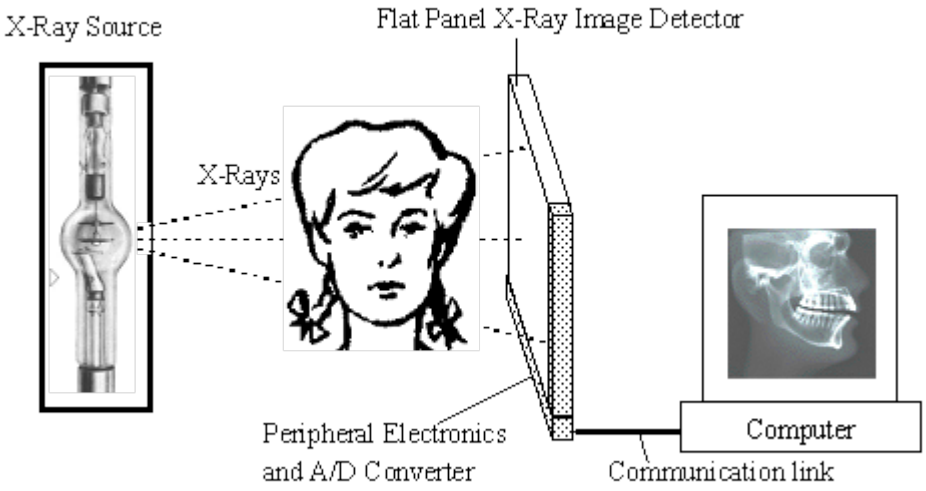

Figure 1.3: Schematic illustration of a flat panel X-ray image detector [1].

the amount of radiation received by that pixel. This converted charge is known as signal charge. In an indirect conversion detector a phosphor plate is used to first convert the X-rays to light which is then detected by the AMFPI, which uses p-i-n photodiodes which are sensitive to the visible light. For both approaches, the X-ray images are constructed by accumulating the signal charge on each pixel's electrode. The signal charges are read out by scanning the array row by row using peripheral electronics and multiplexing the parallel columns to a serial digital signal. This data is then forwarded to a computer system to construct the image. The disadvantage of indirect conversion over direct conversion is that the extra stage of converting the X-rays to light can introduce inefficiencies and noise and degrades resolution. In principle, the direct conversion method is superior, provided a suitable X-ray photoconductor is used that has a high conversion efficiency and low intrinsic noise.

An important step in the development of flat-panel X-ray detector technology

Figure 1.4: Physical structure of an AMFPI with a-Se as a photoconductive layer and peripheral circuitry [Self taken picture, courtesy: ANRAD Corporation].

was the development of flat panel Thin Film Transistor (TFT) arrays for the display market. Each TFT acts as a switching component that allows the signal charge for that pixel to be connected to a charge amplifier when that particular row is read. TFTs are arrayed in a large matrix that is called an active matrix array (AMA). The development of AMAs flourished when fabrication of hydrogenated amorphous silicon (a-Si:H) became technologically possible in 1990s. To produce a direct conversion imager the AMA is coated with the X-ray photoconductor instead of a liquid crystal for a Liquid Crystal Display (LCD).

1.3.2 Active Matrix Readout

Part of an active matrix display is shown in Figure 1.5. This AMA display is constructed with $M(i = 1 \text{ to } M)$ rows of pixels where each row consists of $N(j = 1 \text{ to } N)$ individual pixels. Each pixel consists of a pair of electrodes, a charge storage capacitor and a TFT. The TFT switch allows the signal charge stored in each pixel capacitor to pass onto the charge amplifier, also known as integrating amplifier. Each gate of the TFTs in a row is connected in common to the scanning control circuitry creating M control lines. The scanning controls allow row by row readout of the columns. Each column is connected to the multiplexer through its charge amplifier. The output is multiplexed and digitized and transmitted to a computer to display and manipulate the image.

During X-ray exposure, the photoconductor layer converts the X-ray photons to electrical charge that is collected by the capacitor of each pixel. Normally, all the TFTs are off during exposure permitting the latent image charge to accumulate on

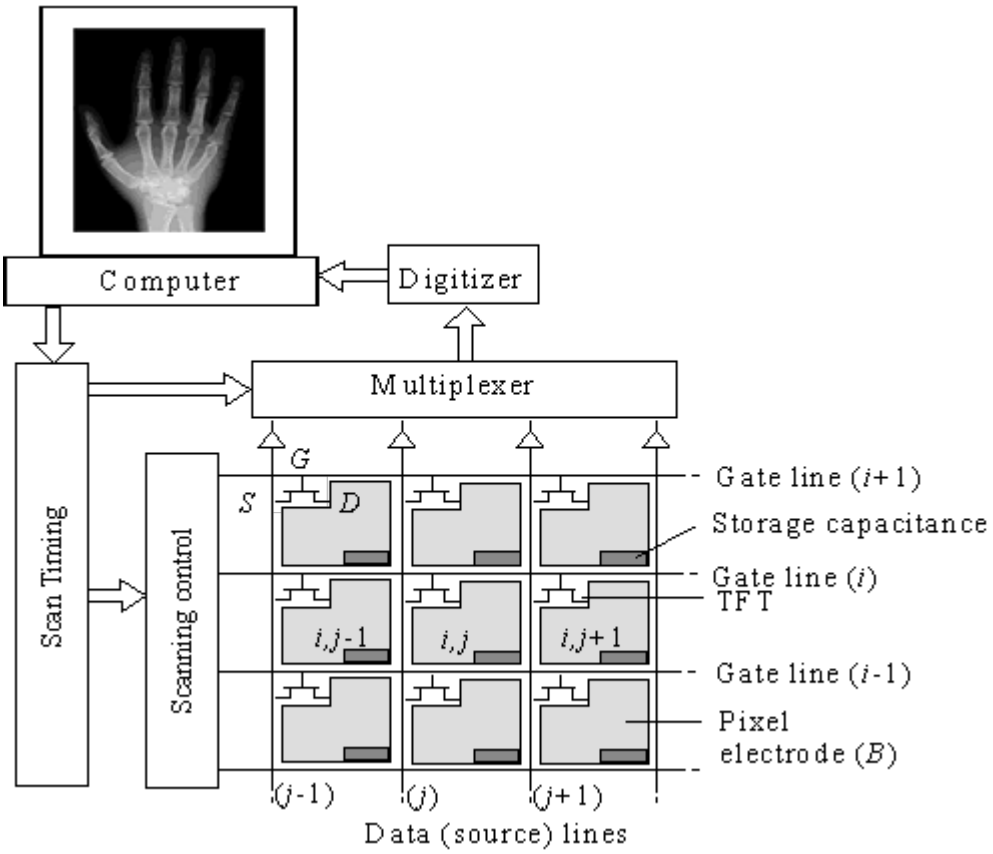

Figure 1.5: Thin film transistor (TFT) active matrix array (AMA) for use in X-ray image detectors with self scanned electronic readout [2]. G, S and D are the gate, source and drain of the TFT transistors.

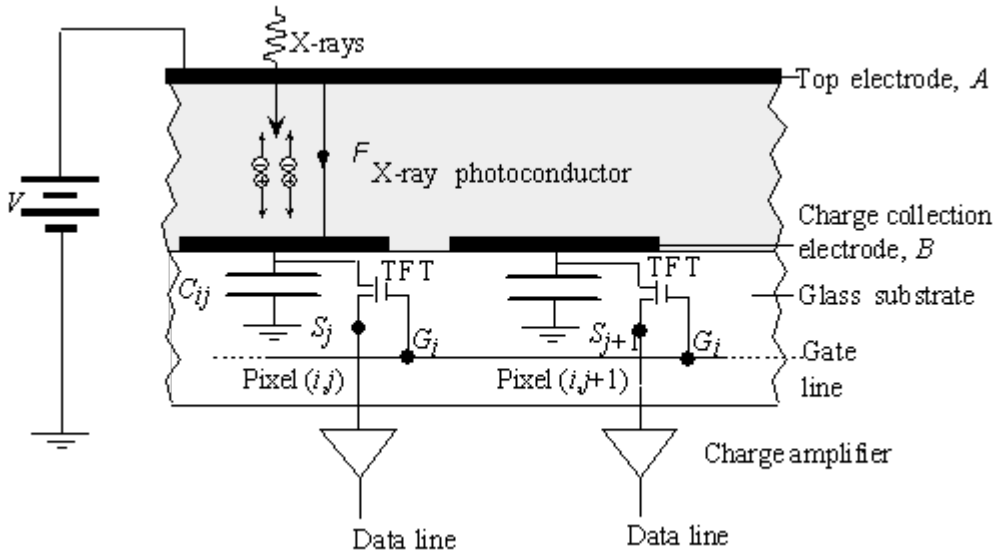

Figure 1.6: A schematic diagram of the cross sectional structure of two pixels, *(i,j)* and *(i, j+1)* of the a-Se image detector [2]. S_j is the source of (i, j)th TFT and G_j is the gate of the (i, j)th TFT.

the $M \times N$ array of pixel capacitors. The readout is achieved by external electronics and software controlling the state of the TFT switches. When gate i is activated, all TFTs in that particular row are turned ON and N data lines (from $j = 1$ to N) will read the charges on the pixel electrodes in row i. The parallel data from $j = 1$ to N are multiplexed into serial data, digitized and fed into the computer. Then the next row, $i + 1$, is activated by the scanning control and the process is repeated until all the rows have been activated and processed.

A simplified cross-sectional diagram of the direct conversion X-ray image detector is shown in Figure 1.6 where the photoconductor layer is made of stabilized a-Se and is coated onto the AMA. An incident X-ray photon, when absorbed by the a-Se layer, produces many (typically ~ 1000) electron hole pairs. A high electric field F is required to separate the electrons and holes; the sign of the F determines which

carrier is collected by the capacitor. The top metal electrode A and the bottom metal electrode B are deposited to facilitate applying the voltage across the a-Se layer. For a-Se photoconductors, typically the applied bias is several kilovolts. The capacitance of the a-Se layer over the pixel is much smaller that the pixel capacitance C_{ij}, so that the majority of the applied voltage drops across the photoconductor. Due to the high electric field, the generated electron-hole pairs travel along the field lines and the charge Q_{ij} is collected by the pixel electrode and stored on the pixel capacitor directly underneath where the X-ray were absorbed. The charge Q_{ij} is proportional to the amount of X-ray radiation incident on that pixels area. For a single X-ray image all the TFTs are required to be turned ON once to be readout, where as in the case of fluoroscopy, to readout the charge the appropriate TFT is turned on every t seconds and the charge signal is transferred to the data line and hence to the charge amplifier. These signals are then multiplexed into serial data, digitized, and sent to a computer for imaging.

The image resolution is determined by the pixel size, which in the present detectors is about 120 to 150 μm, but can be made smaller to achieve the necessary resolution for demanding applications like mammography. Both high resolution and high sensitivity make this system an attractive one among its competitors; it has recently been patented and has been discussed in literature [6].

The performance of direct conversion flat panel X-ray sensors critically depends on the choice of the X-ray photoconductor material. The following section describes the general requirements for X-ray photoconductors.

Table 1.1: Required parameters for digital X-ray imaging systems.

Type of X-ray	Chest radiology	Mammography	Fluoroscopy
Size of the detector	35 cm × 45 cm	18 cm × 24 cm	25 cm × 25 cm
Size of the pixel	200 μm × 200 μm	50 μm × 50 μm	250 μm × 250 μm
Readout time	∼1 s	∼1 s	1/30 s
Maximum X-ray energy	120 kV_p	30 kV_p	70 kV_p
Mean exposure	300 μR	112 mR	1 μR (per frame)

1.4 Requirements of FPDs

Depending on the type of X-ray imaging, the design of the flat panel detector must fulfill the specifications listed in the Table 1.1. In the table, kV_p is the maximum kV value applied across the X-ray tube. Data in Table 1.1 are taken from Rowlands and Yorkston [11].

1.5 Ideal X-ray Photoconductors

It is necessary to select a high quality photoconductive material to achieve the best quality X-ray imagery. Performance of the digital X-ray imaging system mostly depends on the selection and design of the photoconductor inside the Flat Panel Detectors. Ideally, a photoconductive layer should possess the following material properties:

1. Most of the incident X-ray should be absorbed within the photoconductor thickness. The absorption depth δ must be substantially less than the device layer thickness L. X-ray photons that pass through the FPD are considered as lost information. Materials with a higher X-ray absorbtion constant are more

suitable for the photoconductive layer. Typically an ideal photoconductive layer should be able to absorb more than 90% of the incident X-ray photons.

2. While the charge carriers are drifting towards the electrodes there should not be any bulk recombination of electrons and holes. Charge carriers generated by the incident photons must fully be collected by the pixel electrodes to construct an ideal X-ray image. Any recombination of the generated carriers in the bulk lowers the Signal to Noise Ratio (SNR).

3. The lateral diffusion of carriers should be negligible so that spatial resolution is not degraded. Ideally, the charge carrier should drift vertically towards the collecting electrode. Lateral diffusion of charge carriers affects the resolution of the image and its contrast.

4. The mean distance that a carrier drifts in an electric field before being trapped is called the Schubweg. In order for the majority of carriers to be collected by the electrodes, the Schubweg must be greater than the thickness of the photoconductive layer. Trapped carriers not only reduce the amount of charge collected but also cause other problems such as image ghosting on subsequent exposures. Schubweg is defined as $\mu\tau' F \gg L$ where, L is the photoconductor layer, μ is the drift mobility and τ' is the carrier lifetime and F is the electric field.

5. The dark current, that is the current due to the applied field in the absence of X-rays, should be small. The dark current adds charge to the electrode.

Although the charge due to the dark current can be measured and subtracted, the variance in this charge adds to the noise of the device. The dark current should preferably not exceed 10-1000 pA/cm^2 [2]. Limiting the dark current requires either non-injecting electrodes or a wide band gap semiconductor.

6. The photoconductor should have high intrinsic X-ray sensitivity. The amount of radiation energy ($W_{\pm}$) required to create a single free Electron Hope Pair (EHP) must be as low as possible. It must be able to generate as many collectable carriers as possible per unit of incident radiation [9].

7. The photoconductor should be easily coated directly onto a large active matrix array (AMA) panel of typically 30 cm $\times$ 30 cm or even larger without damaging the AMA.

8. The photoconductor should have uniform characteristics over its entire area.

9. The properties of the photoconductor should not change or deteriorate with time or with repeated exposure to X-rays.

1.6 a-Se as a Photoconductive Material

Amorphous selenium is considered one of the best-suited photoconductive materials because stabilized a-Se exhibits most of the required properties stated in the previous section [12].

The X-ray penetration depth can be calculated by the basic equation of the mass attenuation coefficient μ/ρ, where μ is the linear attenuation coefficient and ρ is the

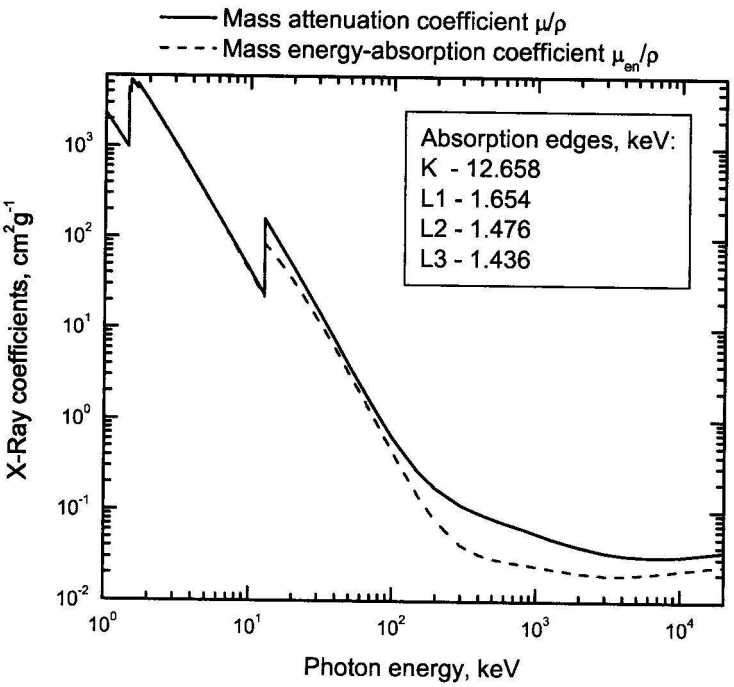

Figure 1.7: Mass attenuation and mass energy absorption coefficients of selenium for X-rays with energies from 1 keV to 20 MeV [3]. μ is the linear attenuation coefficient, μ_{en} is the energy attenuation coefficient and ρ is the material density.

density of the material. The mass attenuation coefficient of selenium for photons with energies in the range 1 keV to 1 MeV is plotted in the Figure 1.7. The location of the K edge makes selenium a suitable material for the detection of X-rays used in the 15 to 22 keV range, the range that is used especially for mammography.

Amorphous selenium photo-detectors are operated at a relatively high electric field, typically at around 10 V/μm. Due to the high electric field, lateral diffusion of the photo-generated carrier in a transverse device structure is limited.

Amorphous selenium is a highly resistive material. Because of its high resistivity, the dark current through the a-Se layer remains low even with a relatively high electric field, such as an applied field of 10 V/μm. Typically, the dark current in the a-Se layer remains in the range 10-1000 pA/cm^2.

The average energy ($W_{\pm}$) per photo-generated EHP in a-Se depends both on the applied electric field F and the energy of the incident photon E. Figure 1.8 shows the electron-hole pair creation energy in a-Se for different applied fields and different beam energies. Kasap and coworkers have reported [13] that for an average photon energy between 32 and 53 keV, the required ionization energy of a-Se is $\approx$ 6 eV.

One attractive feature, that makes a-Se a more suited photoconductor compared to the other competitors in the market is that a-Se can easily be coated as a thick film ranging from 100 to 1000 μm over an area as large as 30 cm $\times$ 30 cm without compromising with the material uniformity.

Due to the fact that amorphous selenium exhibits most of the required properties for a X-ray photoconductive material, it is now considered one of the most highly developed photoconductors for large area X-ray detectors. Amorphous selenium can

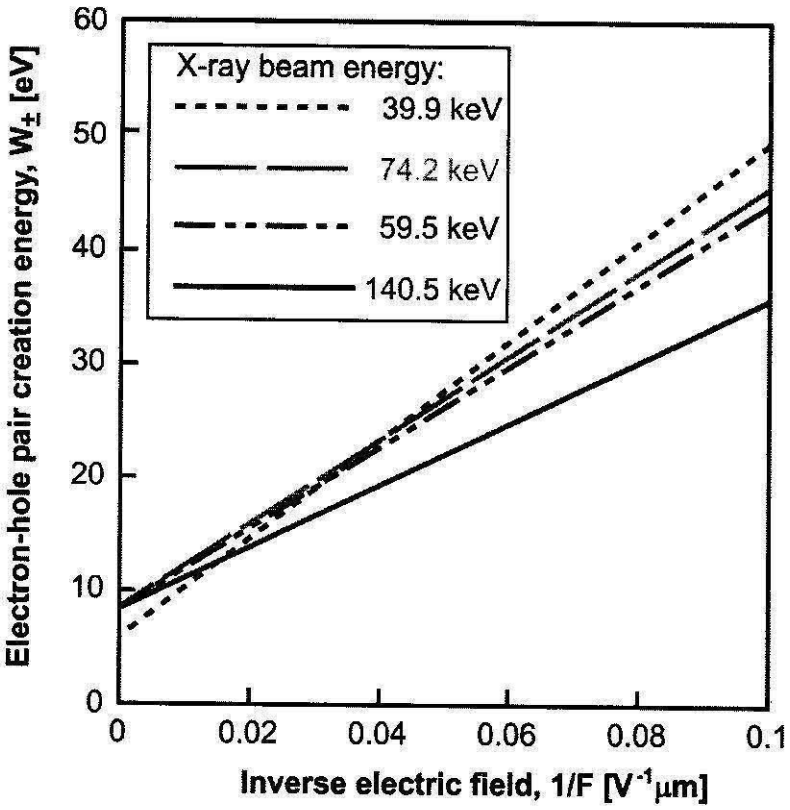

Figure 1.8: Electron-hole pair creation energy in a-Se for different applied fields and different beam energies [4].

easily be coated as thick films, ranging from 100 to 1000 μm which ensures that even high energy X-ray beams are absorbed within the photoconductive layer. This deposition thickness can easily be achieved without the need to raise the substrate temperature beyond 70^oC, so that the a-Si TFTs of the AMA would not be damaged during the deposition. Amorphous selenium is reasonably stable over time provided a small amount of arsenic is added (typically, 0.2% to 0.5% Arsenic by % wt.). This alloy is known as stabilized a-Se. Currently stabilized a-Se is still the preferred choice for X-ray image sensors because it has an acceptable X-ray absorption coefficient, good charge transport properties and low dark current [9].

1.7 Other X-ray Photoconductor Materials

The performance of a direct conversion X-ray detector mostly depends on the properties of the photoconductor layer used in flat-panel detectors. According to the required properties of an ideal photoconductor, stated in Section 1.5, only amorphous or poly-crystalline (poly) materials can be used. Stabilized a-Se is currently the best choice of photoconductor for clinical uses. The next competitor is the poly-crystalline mercuric-Iodide (poly-HgI_2). poly-HgI_2 shows excellent sensitivity, good resolution and acceptable dark current, however, it does not have the long term stability [14, 15]. Cadmium-Zinc-Telluride (CZT), Lead-Iodide (PbI_2) and Lead-Oxide (PbO) detectors are worse than those of poly-HgI_2. However, the X-ray detectors made of CZT photoconductive layers are mechanically and chemically more stable compared to HgI_2 based detectors [16]. The main drawback of a-Se detectors is its

low conversion gain, which specially affects the imaging sensor performance at low exposure [10].

1.8 Research Objectives

Over the past few years, amorphous selenium has gained interest among researchers due to its successful use as a photo-conductive layer in the Flat Panel Detectors used in digital radiography. Prior to the digital radiographic era a-Se had been used as a xerographic material, which generated interest among the researchers of that time. Because of these applications, many aspects of a-Se has been studied. However, no work on noise of a-Se or a-Se based devices has been reported prior to this work. The present work aims to measure the excess noise in photoconductive amorphous selenium layer.

When a layer of a-Se is used as a photoconductive layer in a detector, the noise from the material itself contributes to the overall noise figure of the detector and reduces the signal-to-noise ratio. In order to properly model these detectors, the excess noise from the detector layer must be properly analyzed and incorporated in the models. Excess noise from amorphous selenium with different types of electrodes was measured as well as different compositions of bulk materials and device volumes. The initial results obtained from this project pointed toward the surface or interface as being important so research on excess noise for different surface conditions was carried out. Samples were prepared using conditions known to produce a high quality material similar to that used commercially. The following sections describe the topics

of the research objectives.

1.8.1 Effect of metal contacts on excess noise

Different metals have different work functions and act differently when electroded with crystalline or non-crystalline materials. Some of the metals react with amorphous selenium or dissolve into the material. Special care was taken while choosing the electrode metal. Four different metals were used, namely platinum, gold, aluminum and chromium.

1.8.2 Effect of composition of the a-Se on excess noise

Noise research in other materials usually assumes that the excess noise, especially the $1/f$ noise occurs in the bulk of the material [17, 18]. Noise that has the power spectral density which follows a power law $1/f^{\alpha}$, where α ranges from 0.7 to 1.5 is known as $1/f$ noise. The spectra has a larger magnitude of power at the lower frequency ranges and a smaller magnitude at the higher frequencies. The details of $1/f$ noise is discussed in Chapter 3. It is reasonable to see if changing various aspects of the bulk a-Se has an effect on the $1/f$ noise. The properties varied include alloy composition and sample volume.

1.8.3 Effect of surface condition on excess noise

Based on preliminary results obtained in the beginning of this project, it became apparent that the surface or interface is very important for $1/f$ noise in a-Se. I examined the $1/f$ noise for different surface conditions and reported effect on the

noise.

1.8.4 Effect of X-ray exposure on excess noise

Since this work is motivated by the commercial application of a-Se in X-ray detectors, it is useful to see if X-ray exposure alters the $1/f$ noise. Multilayered devices similar to those used in X-ray detectors were measured before and after X-ray exposure.

1.8.5 Using the measurements of excess noise to calculate (SNR) of a device

Finally, it is useful to have an idea of the effect of $1/f$ noise on the performance of a device. Often, such devices integrate a current as is done in the X-ray detectors. A simple example of the effect of $1/f$ noise on the detector's signal-to-noise ratio (SNR) was calculated based on the experimental data.

1.9 Thesis Outline

This thesis is divided into six chapters. Following this introductory chapter, a brief overview of the various electrical properties of amorphous selenium is given in Chapter 2 and a brief overview of the associated noise is given in Chapter 3. A step-by-step description of how the various samples were prepared and measured is found in Chapter 4. Chapter 3 and Chapter 4 will describe the mathematical background for the measurements. The results and discussion of how these noise

properties vary with different parameters and conditions are given in Chapter 5. Chapter 6 summarizes all the findings and provides suggestions for future work.

Chapter 2
The Physics of Amorphous Selenium

2.1 Introduction

Before going into the analysis of noise of amorphous selenium, it is necessary to understand the electronic properties of amorphous materials. In order to understand the electronic properties, we need to have a theoretical grasp of the energy band structure.

Research on amorphous selenium grew in the mid to late 20th century when a-Se was widely commercialized as the xerographic material in photocopiers. Amorphous selenium was shown to be a photoconductor when Willoughby Smith, an electrician of a telegraph company, reported that the resistance of a-Se decreases with the intensity of ambient light [19]. Recently, research on a-Se has increased due to its successful implementation as a photoconductive layer in digital flat panel detectors for medical X-ray imaging applications. Nowadays, amorphous materials (e.g. amorphous selenium, hydrogenated a-Si etc.) are widely used for applications requiring a large area of uniform semiconductor.

There is a basic difference between the theoretical approaches to crystalline and

amorphous materials. In crystalline semiconductors the energy band structure can be predicted by quantum mechanical methods, which rely upon the long range atomic order of a crystalline solid. However, due to the long range disorder of amorphous semiconductors, these methods don't apply and a direct quantum calculation are mathematically intractable. Instead, researchers have determined the energy band structures of amorphous materials experimentally from a variety of rigorous experiments aided by theoretical models. In the beginning of this chapter, a brief description of amorphous materials is given so that the basic difference between crystalline and amorphous structures becomes clear and, gradually, the discussion will be narrowed down to amorphous selenium.

2.2 Properties of Amorphous Semiconductors

A solid consists of a three dimensional network of atoms. For the equilibrium, in ideal crystalline state, the electrons' energy is minimized. In a covalently bonded crystal, the probability density of the electron is maximum along the line connecting neighboring atoms - we call this a "bond". Every atom has a strict number of bonds to its immediate neighbors with a well defined bond length and bond angle. In the case of semiconductors and insulators, the bonding electrons form the valence band. Valence band states are sometimes called bonding states, whereas conduction band states are called anti-bonding states. For a covalently bonded amorphous solid, bond angles and lengths are no longer the same for all atoms, however, the solid still has bonding and anti-bonding states that in a semiconductor will form a valence and

conduction band.

2.2.1 Growth and Atomic Structure

Two-dimensional examples of crystalline and amorphous bonding arrangements are shown in Figure 2.1. Solids with a long range periodicity in the atomic arrangements are termed crystalline solids. Figure 2.1(a) shows a hypothetical two-dimensional crystal structure with three bonds per atom and a 120^o bonding angle. The crystalline solid has a high degree of long range spatial order in its atomic structure. Bonding angle is fixed for any atom with its adjacent atom throughout the structure. The position of any atom can be determined precisely once the structure is known. Solids that do not have long range periodicity in the arrangements of their atoms can be termed as amorphous or non-crystalline. Because individual atoms in an amorphous solid must still fulfill their requirement for valence bonding, there is a short-ranged order where most atoms have the correct number of nearest neighbors and approximately the correct bond lengths and angles. However, there are small deviations in the bond lengths and angles between adjacent atoms and this leads to a disruption of the periodicity in the material. As a result, the positions of the next nearest neighbor atoms and next, next nearest neighbors etc. become increasingly unpredictable. The inability to determine the positions of farther atoms is known as "long-range disorder". This long-range disorders are best defined when compared to crystalline solids. Although their structures appear random over the long range, amorphous networks still have a high degree of short range spatial order.

Figure 2.1(b) illustrates the structure where most of the atoms have three bonds

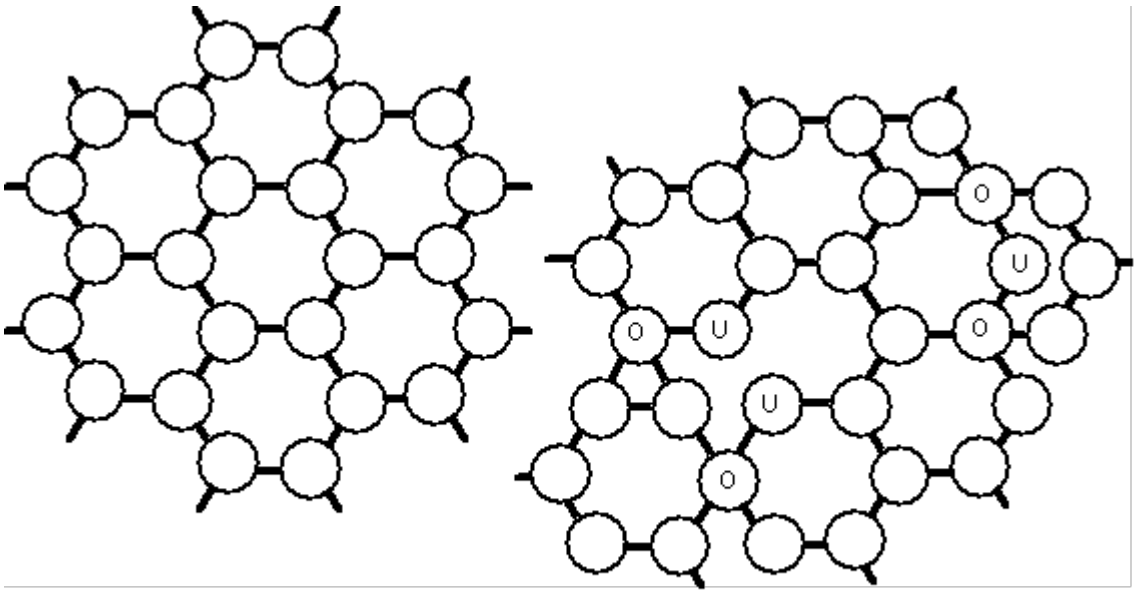

Figure 2.1: Two dimensional representation of the structure of (a) a crystalline solid and (b) an amorphous solid. Atoms marked O represent over-coordinated atoms with more than usual numbers of bonding with adjacent atoms and U represent under-coordinated atoms with less than the usual number of bonds with adjacent atoms.

but some atoms are over-coordinated, shown with the symbol "O" and some are under-coordinated, shown with the symbol "U". The state of disorder is described briefly in the following section.

2.2.2 State of Disorder

In amorphous semiconductors slight variations in the bond length and bond angle between the atoms destroy the spatial periodicity of the network. This phenomenon is known as state of disorder in the atomic network, which introduces localized states, also known as dangling bonds and is termed as defects in the material. This is the fundamental difference between a crystalline and an amorphous material that eventually adds a fair amount of mathematical complexity for analyzing the material. The energy location and the density of these localized states have an enormous impact on the electronic properties of amorphous materials.

Amorphous materials do not possess such crystalline imperfections such as grain boundaries and dislocations due to the lack of long range order. This unique behavior of amorphous materials has a distinct advantage in certain electrical and optical devices.

2.2.3 Band Theory

Despite being different than crystalline material, the electronic properties of the amorphous material is related to the band theory of its crystalline counterpart.

Bands of allowable energy states come about when the theory of quantum mechanics is applied to a crystal. In a crystal, the carriers have allowed energies that

are very closely spaced, which collectively are termed bands; the bands can be separated by energies with no allowed states. The band theory of semiconductors deals with two energy bands, known as the valence band (mostly occupied) and the conduction band (mostly unoccupied), where the charge carriers can exists; a bandgap region separates these two bands by an energy barrier where no charge carrier is allowed. The band-diagram that illustrates the band-theory is known as density of states (DOS) diagram and is often used to predict the properties of a material. Density of states denotes the number of carrier states per unit energy per volume in the material as a function of energy. Crystalline and amorphous semiconductors often show the same basic electronic and optical properties, which led researchers to conclude that these materials might have similar DOS.

In amorphous semiconductors, both the valance and the conduction bands are extended into the band gap region due to Anderson localization, hence the band gap region is named the mobility gap. Anderson showed that the long range disorder of an amorphous material leads to a randomly varying disordered potential. A disordered potential results in perturbations to the electron's wavefunction and if sufficiently strong will result in the wavefunction becoming localized, i.e. the electron is confined to a small volume rather than extending throughout the solid. Some of the deep localized states are created by defects, the majorities of them are created by the loss of long range order and are unique to solids which are amorphous. The three density of states models of amorphous semiconductors are shown in the Figure 2.2. These models are so far been widely accepted by the researchers of amorphous materials.

The difference in the energy band gap diagram between a crystalline semicon-

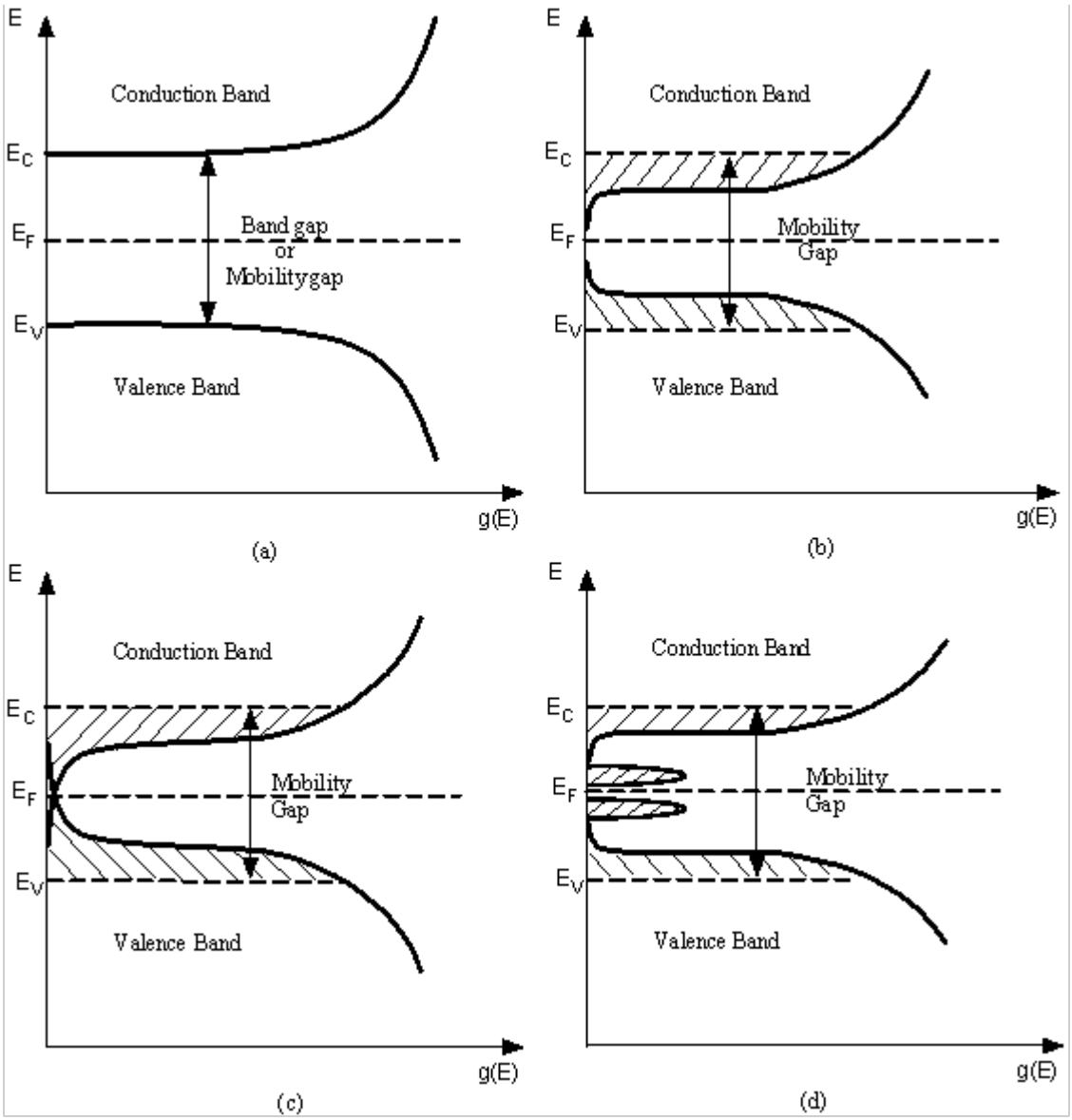

Figure 2.2: Various stages in the development of the energy band model of amorphous semiconductors: a) Model for crystalline semiconductors, b) Model proposed by Mott, c) The Cohen, Fritzsche and Ovshinski (CFO) model, and d) The model of Marshall and Owen [5].

ductor and an amorphous semiconductor is shown in Figure 2.2(a) and (b). For an amorphous semiconductor, there exists an energy level E_c, known as conduction band edge, above which the electronic states are extended and below which they are localized. Deep states are more strongly localized than shallow ones. There is a corresponding energy level for the valence band E_v. The region between E_c and E_v is known as the mobility gap.

Several models have been proposed for density of states in the mobility gap of an amorphous semiconductor. Initially, Mott proposed a density of localized states that decreased away from the band edges known as tail states (Figure 2.2(b)). Cohen, Fritzsche and Ovshinsky [5] suspected that the localized tail states would extend throughout the energy gap of the material and actually overlap in the region near the Fermi (Figure 2.2(c)) level. Though there exists a continuum of energy levels throughout the gap, metallic conduction is not possible because the tail states are localized in space, as in Mott's model. Marshall and Owen elaborated the model by including defect states. Amorphous semiconductors are thought to contain defects such as dangling bonds, chain ends, interstitials, vacancies, impurities etc. All these defects are known as coordination defects. These defects lead to additional localized energy states generally near the center of the bandgap (Figure 2.2(d)).

The localized states are important for electronic transport in amorphous semiconductors. Charge carriers are trapped in the tail states leading to a reduction in the drift mobility as compared to the crystalline material. Further, deep trapping levels enhance recombination causing a reduction in luminescence. A detailed density of state model for amorphous selenium is given in section 2.2.4.

2.2.4 Density of States Model for Amorphous Selenium

It is necessary to further study the density of states in the mobility gap of amorphous selenium to understand its electronic properties. An interesting fact is that selenium is the only material that shows "semiconducting" properties in its crystalline, amorphous and liquid states [20]. In this section, the DOS model of amorphous selenium is explained. In spite of extensively studies [21, 22, 23, 24, 25, 26, 27], the exact DOS of a-Se is still unknown. One of the most cited DOS models was proposed by Abkowitz [21] in 1988 shown in Figure 2.3. A later model was developed by Marshall and Owen [28].

The main features in the density of state distribution proposed by Abkowitz are illustrated in Figure 2.3. There are the usual tail states extending from the valence and conduction bands on which are imposed two features. There are also deep states present in the mobility gap. The states situated close to the mobility edges act as shallow traps. Mobility of charge carriers is affected by the shallow traps through multiple trapping and de-trapping during the period of charge collection. The traps near the Fermi level are the deep traps. Release of a charge carrier from the deep traps takes a much longer time than the time period of the associated experiment. Because of the longer release time, the charge carrier trapped in a deep trap is considered as a lost carrier. The concentration of both the shallow and deep traps determines the overall transport of charge carriers in amorphous selenium.

A group of researchers at the University of Saskatchewan led by Kasap under the influence of ideas presented by Koughia *et al.* [27, 29] has modeled the DOS

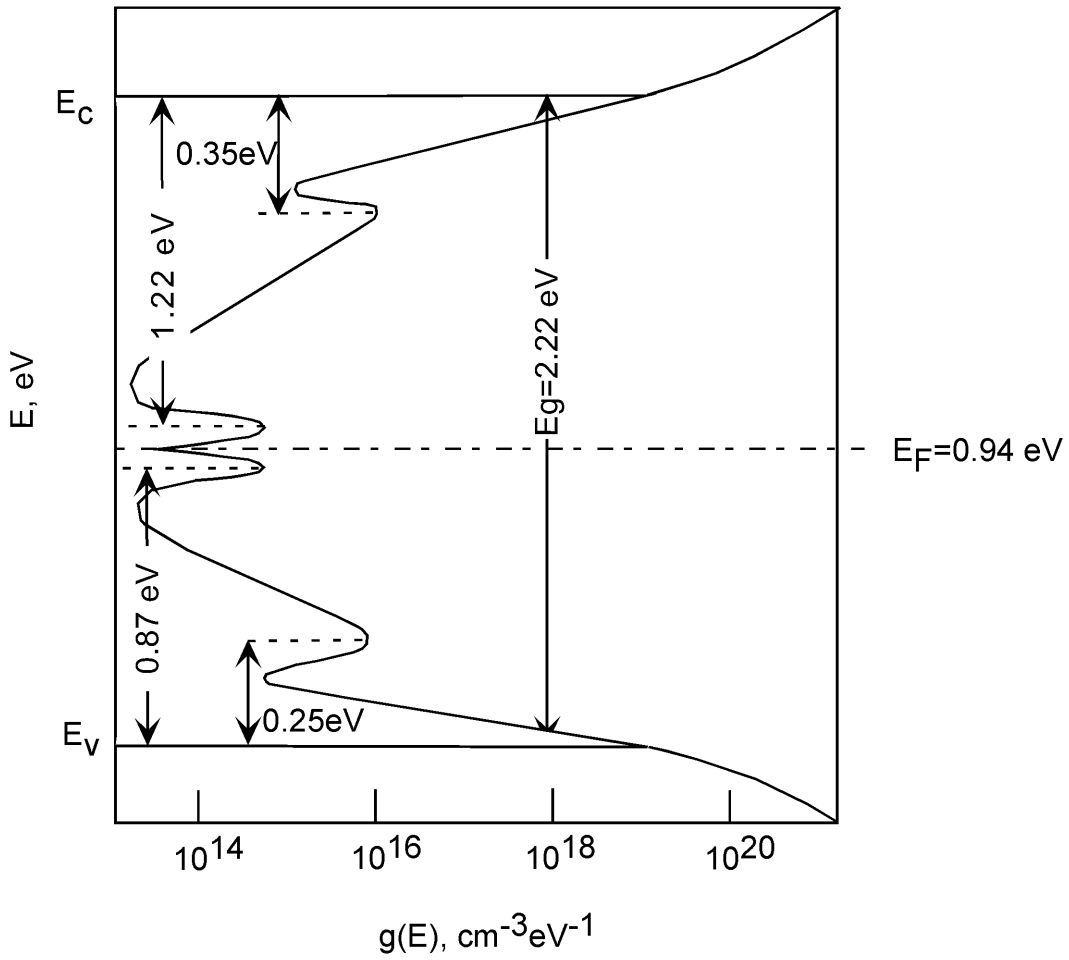

Figure 2.3: Density of electronic states in amorphous selenium proposed by Abkowitz 2.3.

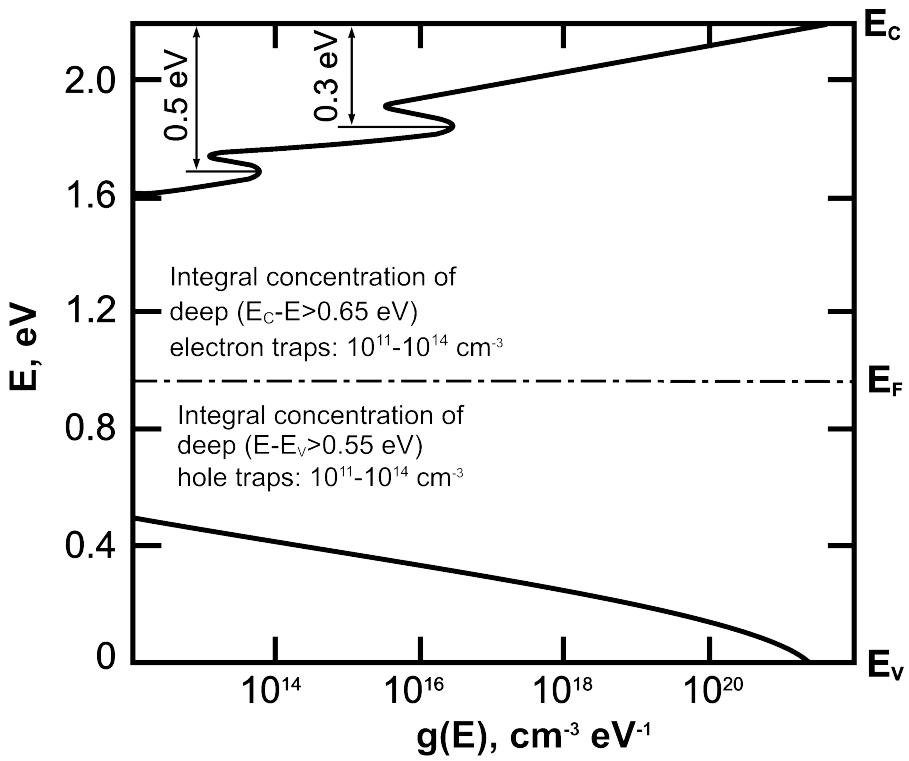

Figure 2.4: Density of electronic states in amorphous selenium proposed by Koughia 2.4.

distribution in the mobility gap of a-Se near the conduction band as a sum of an exponential distribution and three Gaussians [30], shown in Figure 2.4. They found that there exist three distinctly different sets of electron traps in the mobility gap near the conduction band. The positions were found to be 0.3 eV, 0.48 eV and 0.65 eV below the conduction band edge. The electron drift mobility μ_e is controlled primarily by the shallow traps at about 0.3 eV below the conduction band. In addition, deep states with a total concentration in the range 10^{11} to 10^{14} cm^{-3} are indicated by the analysis of the experimental data. However, the distribution near the valence band edge is almost a pure exponential, which is different from the models shown by Abkowitz and other researchers. This model is in good agreement with the model proposed by Naito *et al.* [31]. The DOS model proposed by Koughia correctly predicts the dependence of carrier drift mobility on temperature and electric field.

2.2.5 Electrical Properties of Amorphous Selenium

Amorphous selenium has many localized states in its energy bandgap region. Localized states are localized in space and are not extended throughout the material, and because the electron in a localized state is immobile, there states are known as traps. These localized states can be divided into two groups. Those located near to the mobility edges are called shallow traps and those located deep in the mobility bandgap, i.e. near to the midpoint are called deep traps. Both types of traps are due to various structural defects that are stable at room temperature.

Figure 2.5 illustrates the presence of shallow and deep trap centers and their effect on charge transport. Drift of charge carriers, both the electrons and the holes

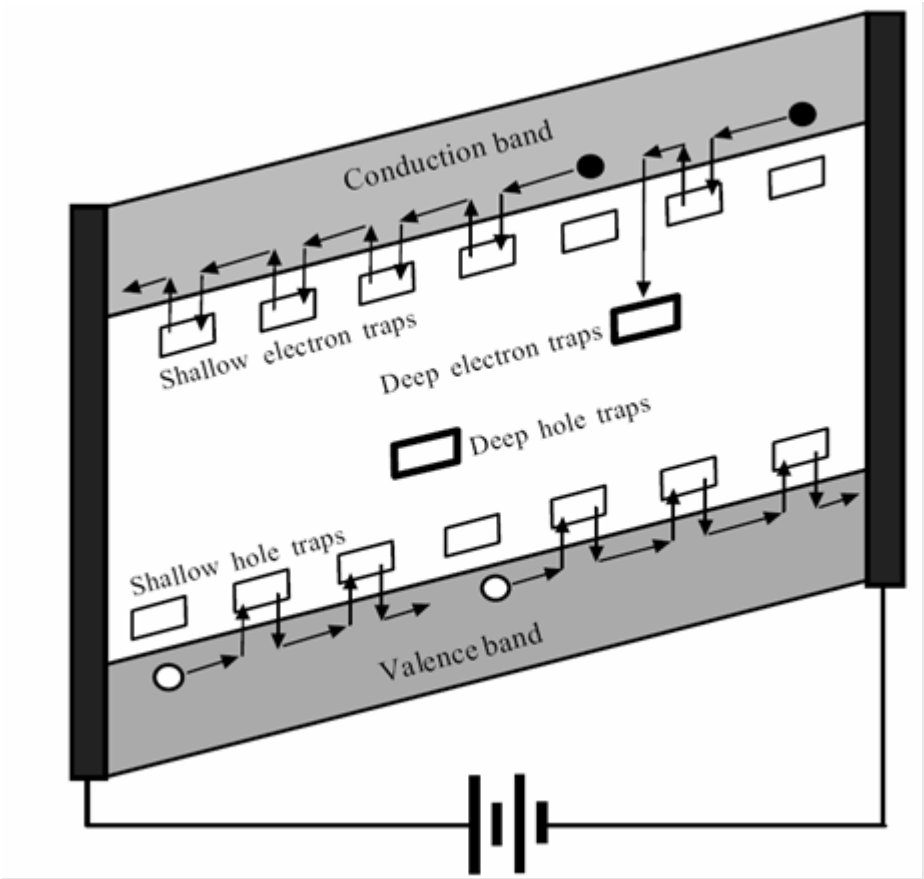

Figure 2.5: Band gap of amorphous material with an applied electric field. Drift of the carriers get affected by the shallow and the deep traps [6].

is affected by the trap centers. Shallow traps reduce the drift mobility. An electron or hole in a deep trap is not expected to be excited to the mobility edge and get collected by the electrode in an experimentally relevant time.With the presence of carrier traps in the structure, the drift mobility can be expressed as,

$$\mu_d = \mu_o \frac{n_{free}}{n_{free} + n_{trap}} = \mu_o \frac{\tau_{free}}{\tau_{free} + \tau_{trap}} \tag{2.1}$$

where, μ_o and μ_d are the absolute and drift mobility of the carriers respectively, n_{free} is the number of free carriers, n_{trap} number of trapped carriers in the shallow trap centers, τ_{free} carrier lifetime before a carrier gets trapped and τ_{trap} lifetime of a carrier while it is remaining in a trap.

2.2.6 Glass Transition Temperature

An important material property of glasses and polymers is the glass transition temperature, T_g. This is a unique property of the amorphous materials. The glass transition temperature of a material is the critical temperature below which the molecules have relatively less mobility. At a temperature below T_g, the material remains hard and brittle, usually called as "glassy" state. Once the amorphous selenium starts getting viscous with heating, the molecules start to wiggle around while staying intact in its chain-like structure. Further heating up makes the material liquid. Figure 2.6 illustrates the comparison between amorphous and crystalline materials [7].

For a crystalline substance there is an abrupt change in specific volume at tem-

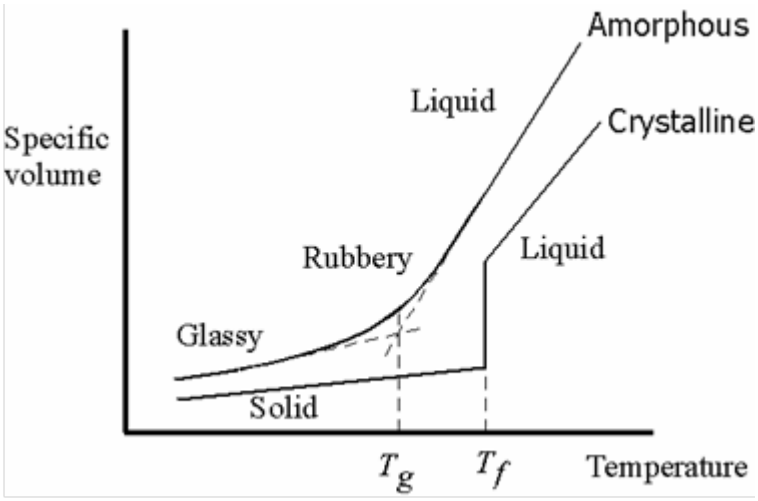

Figure 2.6: Graph showing different states of amorphous and crystalline material [7].

perature T_f when the material becomes a solid. In an amorphous material, between the glassy and liquid states there exists the semi-viscous state which happens around the glass transition temperature.

A crystalline solid is formed by a discontinuous solidification in which a solid appears and grows in the liquid. Hence, the bonds have time to align themselves into proper orientation that provides a long range atomic order. To obtain an amorphous material the liquid must be quickly cooled or quenched at a typical rate less than 1^oC/min. At the glass transition temperature, the atomic motions become too sluggish and the atoms do not have enough time to align and form a regular array. The result is a frozen liquid, and the bonding geometry resembles that of a liquid in solid form without any long range order.

For practical quench rates ($< 1°C$/min) pure selenium forms a glassy solid. However, even at room temperature selenium will crystallize over time, typically

months. The crystallization process of a-Se is accelerated by surface junk and high temperature.

2.3 Stabilized Amorphous Selenium as a Glass

As mentioned in Chapter 1, stabilized a-Se is currently the preferred photoconductor for clinical X-ray image sensors starting from mammography (where low dose of X-ray is required) to chest X-ray (where high dose of X-ray is required) because it can be quickly and easily deposited as a uniform film over large areas (e.g., 35 cm $\times$ 35 cm or larger). Amorphous selenium can be easily coated as thick films (e.g., 100–1000 μm) onto suitable substrates by conventional vacuum deposition techniques and without the need to raise the substrate temperature beyond 60–70°C. Stabilized a-Se is used in the X-ray sensors, because pure a-Se is unstable and crystallizes over time. The crystallization process gets quicker with some other environmental parameters such as exposure to light, ambient temperature, oil from the fingertips etc. Alloying pure a-Se with As (0.2–0.5% As by wt.) greatly improves the stability of the composite film and helps to prevent crystallization. However, it is found that arsenic addition has adverse effect on the hole lifetime because the arsenic introduces hole traps. With the additional 10–40 parts per million (ppm) of chlorine the hole lifetime is restored to its initial value. Thus, a-Se film that has been alloyed with 0.2–0.5% As and 10–40 ppm Cl is called stabilized a-Se. Another property that is improved with this stabilization method is the glass transition temperature. The glass transition temperature of amorphous selenium is less than 40°C, whereas that

of stabilized amorphous selenium is around 60°C.

2.4 Summary

A brief overview of the amorphous structure has been presented in this chapter. The difference between amorphous and crystalline semiconductors has been discussed. Stabilization technique of amorphous selenium is illustrated as it is the material of interest of this work. Atomic structures of amorphous material and the corresponding band theory is discussed in this chapter so that it becomes easier to understand the behavior of the material in the following chapters.

Chapter 3
Electrical Noise

This chapter describes the physics of electronic fluctuations in solids, which is known as electrical noise. Emphasis is given to the main concepts of noise and noise sources, physical mechanisms of different types of noise and, in the conclusion, the details of $1/f$ noise.

Electrical noise is spontaneous random (stochastic) variation of the current through a device or the voltage across a device. These random fluctuations can arise from several sources such as thermal energy or simple statistical variations. The ultimate accuracy of the measurement of any physical quantity is limited by the fluctuations and the ultimate sensitivity of many devices, including the a-Se FPDs that is the main interest of this research work, are limited by fluctuations. Therefore, the physics of fluctuations is especially important for the development of highly sensitive devices [8].

Noise is not always detrimental. A possible role of stochastic resonance in obtaining the weak signals in neuroscience is an excellent example of noise being an important tool where the weak signals are enhanced with an optimized level of noise [32]. Conductivity of any highly resistive material can be measured with the John-

son noise [8]. Also excess noise for a device can indicate a possible weakness of the device that can lead to failure [33, 34, 35]. This chapter reviews $1/f$ noise after a brief overview of thermal or Johnson noise, shot noise and random telegraphic type of noise.

3.1 Sources of Electrical Noise

Noise sources can be divided into two groups: intrinsic noise sources and extrinsic noise sources. The intrinsic noise is produced from the fundamental physical nature of the device material while the extrinsic noise is generated from interactions between circuit and the surrounding environment [36]. The intrinsic noise can be reduced by changing the material properties, but what can be done is often limited. The effect of the extrinsic noise can be minimized with the use of proper mechanical and electrical shielding.

3.2 Mathematics of Noise Spectra

To understand noise measurement requires understanding the mathematics describing a noise signal. Signals are usually described by their behavior in either time or frequency domain. To measure the noise in the frequency domain we have to use Fourier analysis which provides the frequency spectrum of the noise signal. The mathematical analysis of stochastic processes is based on the idea of an ensemble of statistically similar processes observed simultaneously in a given period of time. Quantities are determined by statistical averaging over the ensemble. The

statistical property most commonly discussed in relation to noise measurement is the power. Power is the second-order measure of a process. It is derived by starting with Parseval's theorem,

$$\int_{-\infty}^{\infty} x_1(t)x_2^*(t)dt = \left(\frac{1}{2\pi}\right)\int_{-\infty}^{\infty} X_1(j\omega)X_2^*(j\omega)d\omega \tag{3.1}$$

where $x_1(t)$ and $x_2(t)$ are signals whose Fourier transforms are $X_1(j\omega)$ and $X_2(j\omega)$ respectively. The theorem is quite general and requires only that the time functions be integrable.

Let us assume that a noise signal is observed from $-T/2$ to $T/2$, outside of this window of time the signal has a value of zero. This gated noise signal is called $x_T(t)$. $x_1(t)$ and $x_2(t)$ in Equation 3.1 are now related to the gated noise signal by,

$$\begin{gathered} x_1(t) = x_T(t+\tau) \\ \text{and} \\ x_2(t) = x_T(t) \end{gathered} \tag{3.2}$$

where τ is a delay time. Since $x_T(t)$ is a gated process which is zero outside of its time window, its Fourier transform exists and Parseval's theorem gives

$$\int_{-\infty}^{\infty} x_T(t+\tau)x_T^*(t)dt = \left(\frac{1}{2\pi}\right)\int_{-\infty}^{\infty} |X_1(j\omega)|^2 exp(j\omega\tau)d\omega \tag{3.3}$$

When $\tau = 0$, equation 3.3 reduces to,

$$\int_{-\infty}^{\infty} x_T(t)^2 dt = \left(\frac{1}{2\pi}\right) \int_{-\infty}^{\infty} |X_T(j\omega)|^2 d\omega \tag{3.4}$$

This is known as Plancheral's theorem or energy theorem. Both sides of equation 3.4 represent the total energy in $x_T(t)$. Therefore, $|X_T(j\omega)|^2$ can be interpreted as the energy density of the noise signal $x_T(t)$ with units of energy joule per Hertz, and it will be finite provided $T < \infty$. The average power is just the total energy divided by T. When $x_T(t)$ is real, as $T \to \infty$ the total power can be given by,

$$\lim_{T\to\infty} \frac{1}{T} \int_{-\infty}^{\infty} x_T(t)^2 dt = \lim_{T\to\infty} \left(\frac{1}{2\pi}\right) \int_{0}^{\infty} \frac{2|X_T(j\omega)|^2}{T} d\omega \tag{3.5}$$

where the limits are assumed to exist. The integral on the right can be given in a one-sided form because $x_T(t)$ is a real process and an even function of frequency. The power spectral density of the stationary signal $x_T(t)$ can be written as,

$$\overline{S_x(\omega)} = \lim_{T\to\infty} \frac{2\overline{X_T(j\omega)}^2}{T} \tag{3.6}$$

which converges to a specific value. Thus the power spectral density of a stationary process is expressed as a property of the ensemble as a whole, not as a property of an individual member function of the ensemble [8].

The expression for the power spectral density allows the techniques of digital sampling to be applied to noise measurements. Equation 3.6 shows that there is a relationship between the power spectral density and the Fourier transform of the gated noise signal. This equation is based on averaging of the signal.

3.3 Types of Electrical Noise

Johnson or thermal noise, shot noise, random telegraphic noise and $1/f$ noise have been named according to their nature. The origins of Johnson noise and shot noise are known. However, in spite of being an important topic in noise research for past several decades, the exact mechanism for $1/f$ noise is still unknown in most cases. Among the different types of noise, thermal noise is present in every resistive material.

3.3.1 Thermal Noise

Thermal noise is produced by the thermally driven random motion of free charge carriers in a conductor. The mechanism is similar to that of Brownian motion where a macroscopic particle jiggles back and forth due to collisions with moving atoms. The motion is limited to the thermal energy of the atoms. The statistical properties of Brownian motion was first described by Einstein in 1906 [37]. In a conductor, the situation is somewhat different because the charge carriers are microscopic but their random motion is still due to interactions with thermal vibrations. For an open-circuit conductor, the average current is zero, but the fluctuations produce a noise voltage across the conductor. For a shorted conductor, the fluctuations induce a noise current that flows through the short. Thermal noise is always present when any resistive element is in thermal equilibrium with its surroundings and is often referred to as Johnson noise, as this phenomenon was first observed by Johnson in 1928 [38]. The experimental results of Johnson showed that the open circuit mean-

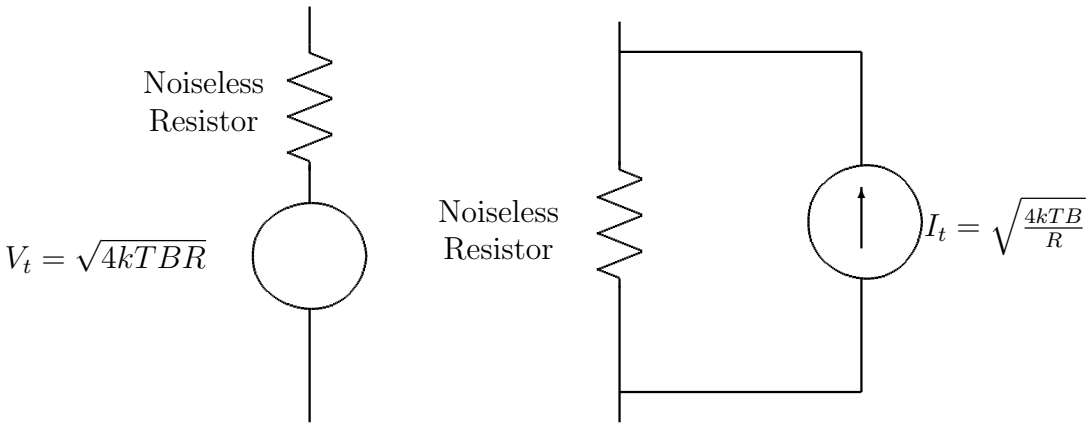

Figure 3.1: Johnson noise models for a physical resistor.

square noise voltage depends upon the temperature and can be expressed as Eq. 3.7,

$$\overline{V_t^2} = 4kTBR \tag{3.7}$$

where k is Boltzmann's constant in JK^{-1}, T is the temperature in Kelvin, B is the bandwidth in Hz of the measurement, and R is the resistance of the conductor [39].

The Johnson noise of a device is usually modeled as a noiseless resistor in series with a voltage-noise generator or a noiseless resistor in parallel with an ideal fluctuating current source and is shown in Figure 3.1 [40].

The mean square of Johnson current noise is

$$\overline{I_t^2} = \frac{4kTB}{R} \tag{3.8}$$

The noise sources in both the voltage-noise and current-noise models are zero

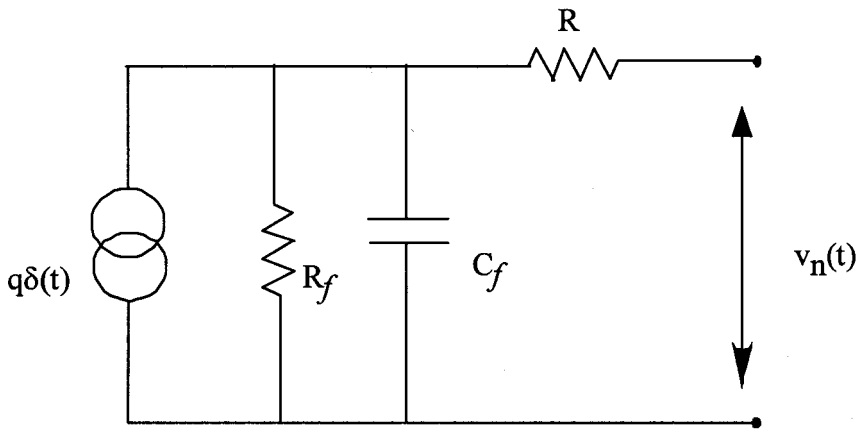

Figure 3.2: Equivalent noise circuit of a single resistor.

mean Gaussian noise generators with a white power spectral density, which means that the noise power density is the same over the frequency. In the voltage-noise model an increase in the voltage noise spectral density results from increasing resistance, and in the current-noise model, the current noise spectral density decreases with increasing resistance. Other passive elements, such as inductors and capacitors, do not create thermal noise if they do not have a resistive component meaning that an ideal inductor or an ideal capacitor does not produce any thermal noise.

Mathematical analysis of thermal noise: The mathematical model of Johnson noise can be derived from a one dimensional model of a resistor with cross-sectional area A and length L. Let us consider the transit of an electron between collisions with mean-free-path l_f. This can be modeled by a parallel plate capacitor with plate separation l_f and charge density $\pm\frac{q}{A}$, where q is the charge accumulated in the capacitor. The equivalent circuit for this configuration is shown in Figure 3.2, where R_f and C_f are the resistance and the capacitance of the region between the

charge sheets, bulk resistance $R = (R_f \times L)/l_f$ and $q\delta(t)$ is the current generator producing a pulse shape at the terminals and a subsequent charge relaxation.

The following equation can be written if a voltage pulse $v_n(t)$ appears at the terminal due to the single square wave pulse, which is a delta function, and can be expressed by the following equation:

$$C\frac{dv_n(t)}{dt} = \frac{v_n(t)}{R} + q\delta(t) \tag{3.9}$$

where, $C = C_f l_f/L$. Fourier transforming both sides of Equation 3.9 provides the transform of the voltage pulse

$$V_n(j\omega) = \frac{ql_f(R/L)}{(1 + j\omega\tau_1)} \tag{3.10}$$

where, $\tau_1 = RC = \rho\varepsilon$ is the dielectric relaxation time, ρ is the resistivity and ε is the permittivity of the material. The magnitude of τ_1 is extremely short, in the range of 10^{-12} seconds.

Equation 3.10 is the transform of a voltage pulse at the terminals of the resistor due to the single event within the resistor that produces the pulse. The inverse transform of the pulse shape function is a decaying exponential with a decay time equal to τ_1. Assuming that there is an equal probability of positive and negative l_f, the mean value of voltage fluctuations at the terminal is zero. With the Fourier transform of the terminal voltage from Eq. 3.10 and from Carson's theorem [Equation 2.41; [8]] we get the PSD of the terminal voltage fluctuation at the terminals of the resistor as,

$$S_{v_n}(\omega) = \frac{2\nu q^2 (R/L)^2 \overline{l_f^2}}{(1+\omega^2\tau_1^2)} \tag{3.11}$$

where ν is the mean number of events per second within the volume of the resistor. Taking n as the density of electrons in the material and τ_f is the mean free time between the collisions, then

$$\nu = nAL/\overline{\tau_f} \tag{3.12}$$

Resistance can be related to the electron mobility using the following expression:

$$R = \frac{L}{nq\mu A} \tag{3.13}$$

A statistical mechanical argument [8] shows that

$$\mu = \frac{q\overline{l_f^2}}{2\overline{\tau_f}kT} \tag{3.14}$$

where k is Boltzmann's constant and T is the absolute temperature. Combining Eqs. 3.11 to 3.14 leads to the expression for the PSD for open-circuit voltage fluctuations,

$$S_{v_n}(\omega) = \frac{4kTR}{(1+\omega^2\tau_1^2)} \tag{3.15}$$

and the short-circuit current fluctuations,

$$S_{i_n}(\omega) = \frac{4kT/R}{(1+\omega^2\tau_1^2)} \tag{3.16}$$

For all practical frequencies $\omega^2\tau_1^2$ is negligible, which reduces Eqs. 3.15 and 3.16 to Eqs. 3.7 and 3.8 respectively.

The thermal noise power spectral density is uniform and independent of frequency. It has a constant magnitude for a given bandwidth anywhere in the spectrum. For example, the Johnson noise power in a 1 kHz band between 1 Hz to 1.001 kHz is equal to the Johnson noise power in a 1 kHz band between 1 MHz to 1.001 MHz. Johnson noise is also referred as "White Noise"meaning that it is made up of all frequency components with the same strength [41].

3.3.2 Shot Noise

Shot noise occurs when a flow is composed of discrete elements, such as a current which is a flow of charge carriers, either electrons or holes, and the charge carriers are statistically independent of each other. Fluctuations in the average current arise from the random bunching of these discrete charge carriers. An example of shot noise is the popping of corn kernels hitting the walls of the pot. Current shot noise is often suppressed in the conductors because the coulomb repulsion of charge carriers introduces correlations between them. However, if the current is controlled by the charge carriers either overcoming or tunneling through an energy barrier then the probability of any electron crossing the barrier becomes independent of any other electron, hence shot noise results.

Shot noise is a Poisson process and the charge carriers that move past on a given time follow a Poisson distribution. The current fluctuations show a standard deviation of

$$\sigma_i = \sqrt{2qIB} \tag{3.17}$$

where, q is the amount of electric charge carried by a single electron (1.6×10^{-19} C), I is the average current through the device and B is the bandwidth in hertz over which the noise is measured [42, 43].

Mathematical analysis of shot noise: The shot noise current can be assumed as a random train of pulses. Each electron that overcomes or tunnels through a potential barrier carries a discrete electronic charge equal to q. If the transit time τ is such that $\tau \ll T$, where T is the observation time over which time-average is chosen, then each pulse can be represented by a delta function $\delta(t)$ which can in turn be approximated by a short rectangular pulse as shown in Figure 3.3(b). The equivalent electronic charge,

$$\int_{-\infty}^{\infty} q\delta(t)dt = q \tag{3.18}$$

If $F(\omega)$ is the Fourier transform of $\delta(t)$ then,

$$F(\omega) = \int_{-\infty}^{\infty} q\delta(t)e^{(-j\omega t)}dt = q\frac{\sin(\omega\tau/2)}{\omega\tau/2} \tag{3.19}$$

Hence,

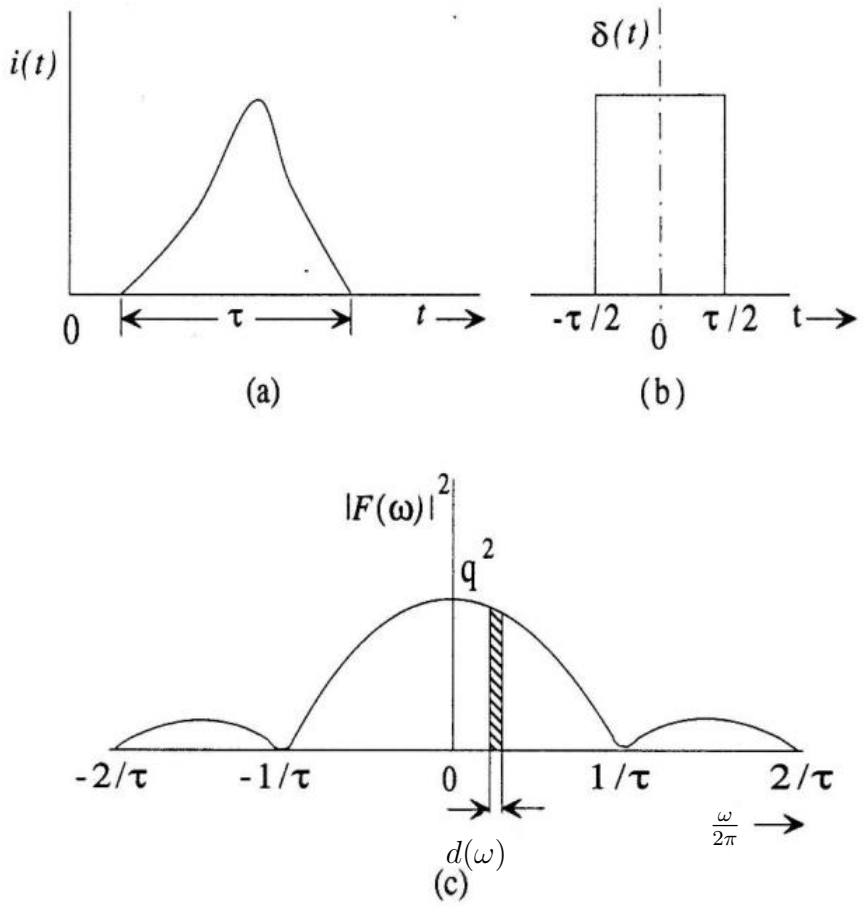

Figure 3.3: Steps in the development of the equation for shot noise. (a) Each electron gives rise to a current pulse, (b) An ideal pulse associated with each charge carrier and (c) The energy spectral density function.

$$|F(\omega)|^2 = q^2 \left[\frac{\sin(\omega\tau/2)}{\omega\tau/2}\right]^2 \tag{3.20}$$

where $|F(\omega)|^2$ is the energy spectral density and is shown in Figure 3.3(c) [43]. Therefore, given the shape of the energy spectral density, it can be assumed that at sufficiently low frequencies, the spectral density over a given $df = B$ is constant. This constant value of energy spectral density q^2 is assumed to be the actual value at zero frequency.

The total energy W in the bandwidth B is,

$$W = \frac{1}{2\pi}\int_{-\infty}^{\infty} |F(\omega)|^2 d\omega = \frac{1}{\pi}\int_{0}^{\infty} |F(\omega)|^2 d\omega \tag{3.21}$$

or given the assumptions mentioned, the total energy may be expressed as,

$$W = 2q^2 B \tag{3.22}$$

If n electrons are counted at the anode over a sufficiently long time T the average shot noise power in a 1 Ω resistor becomes

$$i_s^2 = nW/T = n(2q^2B)/T \tag{3.23}$$

now substituting $I = nq/T$ for the average dc current, one can get the formula for the rms value of shot noise current,

$$i_s = \sqrt{2qIB} \tag{3.24}$$

In the noise studies of the selenium samples in many cases the current is so low that the expected shot noise is less than other noise sources such as $1/f$ noise or Johnson noise. However, in those instances where a larger current was used so that a shot noise signal would be large enough to measure, still the shot noise was not present due likely to the suppression mentioned above. The only case where shot noise was seen was for multilayered samples where there is injection which may have restored the shot noise although the magnitude was still less than that predicted by Eq. 3.24.

3.3.3 Random Telegraphic Noise

For many materials, the observed noise is greater than the Johnson and shot noises; this noise is defined as the excess noise of the device. The excess noise has many forms and Random Telegraphic Noise (RTN) is one of them. RTN, also called switching noise, is the random transition between two or more discrete levels. A typical waveform of RTN is shown in Figure 3.4(a) [8]. The switching events are superimposed on other sources of noise. Filtering out the other noise leaves a signal which is similar to a telegraphic code. RTN is not universally present but is usually detectable in devices of very small volume or at junctions. The spectral density of an RTN signal has Lorentzian spectrum and can be expressed as,

$$S(\omega) = \frac{A}{(\omega - \omega_o)^2} \tag{3.25}$$

where, ω is the frequency and ω_0 and A are the constants determined by the switching

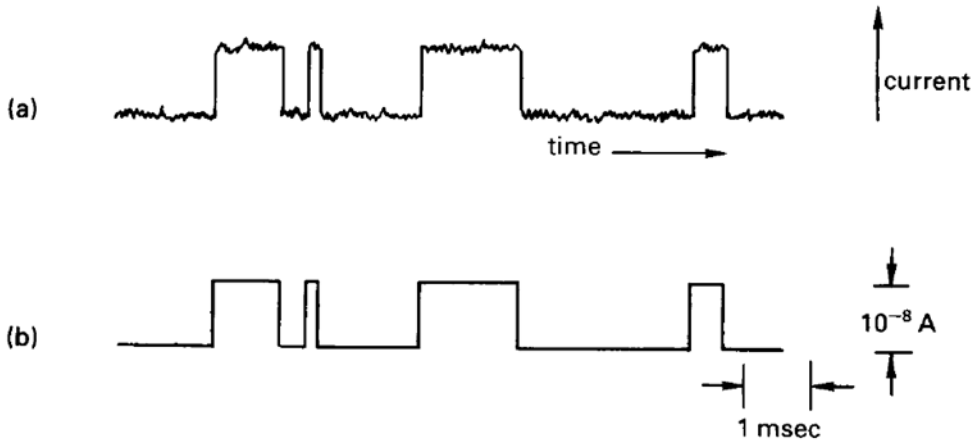

Figure 3.4: Typical RTN noise current waveform a) as observed with white noise superimposed and b) after low-pass filtering

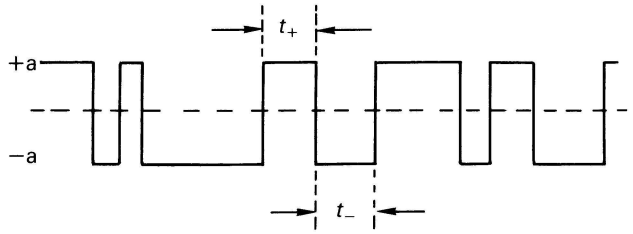

Figure 3.5: Sketch of an RTN signal [8]

rates, ω_o is often referred as the "knee frequency".

Mathematical analysis of RTN: Let us assume a pulse-shape function where τ_+ and τ_- are the average time spent in the upper and lower levels. If we assume that the probability of a transition from one level to the other in the time interval $(t, t+dt)$ is νdt, and that this probability is independent of events occurring outside the interval, then the probability of m transitions in the interval $(0, T)$ is given by the Poisson distribution,

$$p(m,T) = \frac{(\nu T)^m}{m!} e^{-\nu T} \tag{3.26}$$

The probability density of the times t_+ and t_- spent in the two levels is

$$p(t_\pm) = \tau_\pm^{-1} e^{-(t_\pm/\tau_\pm)} \tag{3.27}$$

Equation 3.27 states that the times in the two levels are exponentially distributed in agreement with the statistical measurements of burst noise depicted in Figure 3.5. The autocorrelation function of the burst noise is $\overline{x(t)x(t+\tau)}$, which in turn gives the power spectrum through the Weiner-Khintchine theorem. The product $x(t)x(t+\tau)$ is equal to $+a^2$ if an even number of transitions occur in the interval $(t, t+\tau)$ or $-a^2$ if an odd number of transitions occur at the same interval. Therefore the average value is,

$$\begin{aligned} \overline{x(t)x(t+\tau)} &= a^2 \times \text{ probability of an even number of transitions in } (t, t+\tau) \\ &- a^2 \times \text{ probability of an odd number of transitions in } (t, t+\tau) \\ &..... \end{aligned} \tag{3.28}$$

The two probabilities depend only on the length of the interval $|\tau|$ and not on the starting time of the interval. Hence by setting $T = |\tau|$ in Eq. 3.26, we have from Eq. 3.28

$$\overline{x(t).x(t+\tau)} = a^2 e^{-2\nu|\tau|} \tag{3.29}$$

But the average on the left of Eq. 3.29 is equal to the autocorrelation function $\overline{\phi_x(\tau)}$, of the waveform. Therefore,

$$\overline{\phi_x(\tau)} = a^2 e^{-2\nu|\tau|} \tag{3.30}$$

and the corresponding power spectrum is

$$S_x(\omega) = 4\int_0^\infty \overline{\phi_x(\tau)} cos(\omega\tau) d\tau = \frac{2a^2/\nu}{(1+\omega^2/4\nu^2)} \tag{3.31}$$

The power spectrum of Eq. 3.31 has the shape of a Lorentzian distribution. It is essentially flat at low frequencies below the frequency ν/π, and decays as ω^{-2} at higher frequencies.

3.3.4 $1/f$ Noise

The most ubiquitous excess noise is $1/f$ conductance noise. $1/f$ noise was first observed by J. B. Johnson in 1925 [44]. While observing the current fluctuations of electronic emission in a thermionic tube he found this $1/f$ noise whose spectral density decreases with increasing frequency, apart from the frequency independent shot noise. Schottky proposed its name 'flicker noise' in 1926. Till now measurements of the current noise have been performed in various types of materials, and the $1/f$ noise has been found in many of them.

When a constant voltage is applied across a resistor, a fluctuating component of the current is observed on top of the Johnson noise. The conductance of the material fluctuates whenever a current flows through the material causes the fluctuating current. Essentially all conductive materials exhibit $1/f$ noise including the semiconductors that make up solid state devices. This excess noise has become an important topic for research as the noise affects the performance of these devices. The main object of the research work proposed here is to determine the $1/f$ noise in amorphous Selenium.

$1/f$ noise gets its name from the shape of its power spectral density, which varies with frequency as $|f|^{-\alpha}$, where α usually falls between 0.7 and 1.45. This dependence has been observed down to frequencies as low as 10^{-6} Hz. There are nearly as many theories of the origin of this fluctuation phenomenon as there are instances of its occurrence. Many aspects of $1/f$ noise are still debated such as the effects of contacts, carrier number versus mobility fluctuations, and bulk versus surface effects. Many researchers have been compelled to search for a universal mechanism because of the wide range of systems in which $1/f$ noise is observed. These include not just electrical materials but also other physical and biological systems such as brain waves, thunderstorms, and earthquakes [8]. However, to date no universal theory has gained widespread acceptance.

Chapter 4
Experimental Procedure and Measurements

4.1 Introduction

This chapter describes the preparation of a-Se samples and the techniques followed to measure noise in the deposited samples.

Selenium alloys are obtained in pellet form from the refinery and then evaporated using a vacuum coater. Different methods such as cathode sputtering, glow discharge, chemical vapor deposition (CVD) are used to deposit other types of amorphous and microcrystalline materials but are not of interest for this research.

This chapter will start with the preparation of substrates and adding metal electrodes by sputtering a thin layer of the metal, typically a few tens of nm, on the surface of the glass substrate. The thin layer of metal will be used as the bottom electrode of the sample. The evaporation technique will then be described that produces a thick layer of a-Se, varying from 20 μm to 200 μm according to the need of the noise experiment.

The following part of the chapter will discuss the experimental setup and will

describe the noise measurement technique for a low magnitude of noise signal, typically in the range from 10^{-22} A^2/ Hz to 10^{-26} A^2/ Hz, produced from a low dark current, typically in the range between 10^{-6} A to 10^{-10} A. Noise measurements of this low a magnitude are quite challenging. I had to choose a low-noise current preamplifier to extract and amplify the noise signal to a higher magnitude so that it can be measured by the subsequent equipment. Brief descriptions of the apparatus used in this project are given in the following sections. The concluding part of this chapter will describe the calibration process and the response curves of the system.

4.2 Sample Preparation

The samples used in the noise studies have a transverse geometry—that is the current flows through the layer, not along the layer. Thus electrodes need to be deposited both before and after the selenium deposition. The sample preparation in this work is a four step process that starts with the cleaning of the glass substrate to make sure that no external substances remain on the surface of the substrate followed by the deposition of a few tens of nm of metal on the substrate to be used as the bottom electrode. Once the metal is deposited the substrate becomes ready for a-Se deposition. A number of factors were varied while depositing a-Se layer according to the needs of the experiments. The final part of sample preparation is to deposit the metal electrodes on top of the a-Se layer.

4.2.1 Substrate Cleaning

It is necessary for the glass substrate to be cleaned so that the a-Se layer is not contaminated by external substances, i.e. the oily substance from the fingerprints on the glass slide. Amorphous selenium is unstable and tends to crystallize quickly in the presence of contaminants. The first step is to get rid of the oily substances and the polymers from the glass surface. The cleaning process starts with the glass slides submersed in trichloroethylene. One has to be careful when handling trichloroethylene as it is hazardous to the human health. After the glass substrate is left fully submersed for a period of 5 minutes it is then cleaned with methanol several times, typically 5 to 7 times followed by cleaning with de-ionized water for at least for 5 times.

Concentrated detergents are also used to clean the glass substrates if the substrates are not too oily. Glass slides are submersed in the diluted detergents for 5 minutes using an ultrasonic cleaner. These glass slides are then cleaned with the flow of warm water for 7 to 10 minutes followed by rinsing 5 times with the de-ionized water.

Once the glass substrate is clean, the remaining water on the surface of the substrate is removed with high-pressure filtered air. The substrates are then kept in a dryer for about 4 to 5 hours at 40°C.

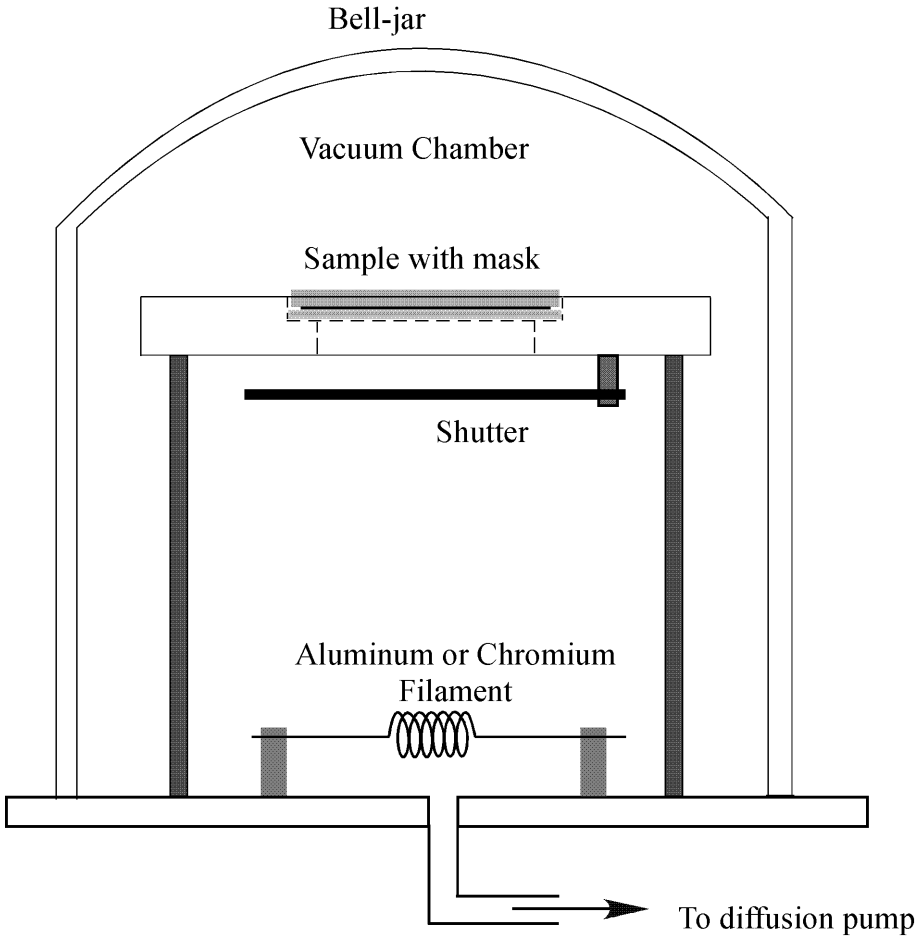

Figure 4.1: Schematic diagram of the evaporator unit used for metal evaporation.

4.2.2 Metal Deposition for Both the Electrodes

Two different methods are used to deposit a thin layer of metal on the glass substrates for the bottom electrodes or on the selenium layers for the top electrodes. Aluminum and chromium are deposited by evaporation while gold and platinum are sputtered.

The schematic diagram of the metal evaporator is shown in Figure 4.1. Evaporating aluminum and chromium on the surface of the glass substrate or amorphous

selenium is done in the following way. Firstly, a filament of pure aluminum or pure chromium (Kurt J. Lesker: Part No. EVSCRW2) is installed inside the chamber. To deposit the bottom electrode a pre-cleaned glass substrate is placed on the holder. The shutter is tested to be working properly and remain at the closed position. A glass bell-jar, especially built to sustain at the low pressure is positioned properly to cover the whole assembly. At first the air inside the chamber is pumped down to the vacuum level of 60 milli-Torr. Pressure inside the chamber is brought further down to a vacuum level of 10^{-5} Torr with the help of a diffusion pump backed by the mechanical pump. Once the desired vacuum level is achieved, the necessary amount of current is allowed to flow through the filament to heat the metal. Once the metal starts evaporating, the shutter is opened for a required period of time, usually a minute to allow the metal to deposit. The shutter is closed once enough metal has accumulated. The a-Se layer can be affected by heat if the shutter is kept open for as little as two minutes, but seems to survive for lesser times.

Sputtering uses a plasma of a non-reactive gas, typically argon, to knock atoms off a target; the atoms then diffuse to the sample forming a thin film. To proceed with the sputtering at first it is necessary to make sure of the following steps:

1. A target of the metal of our interest is placed as the cathode in the system
2. The cathode magnet and its surroundings are free from other metals from the previous depositions to prevent contamination
3. The distance from the target to the sample is adjusted so that the bombarded metal ions don't settle as grain of metals on the surface of the sample

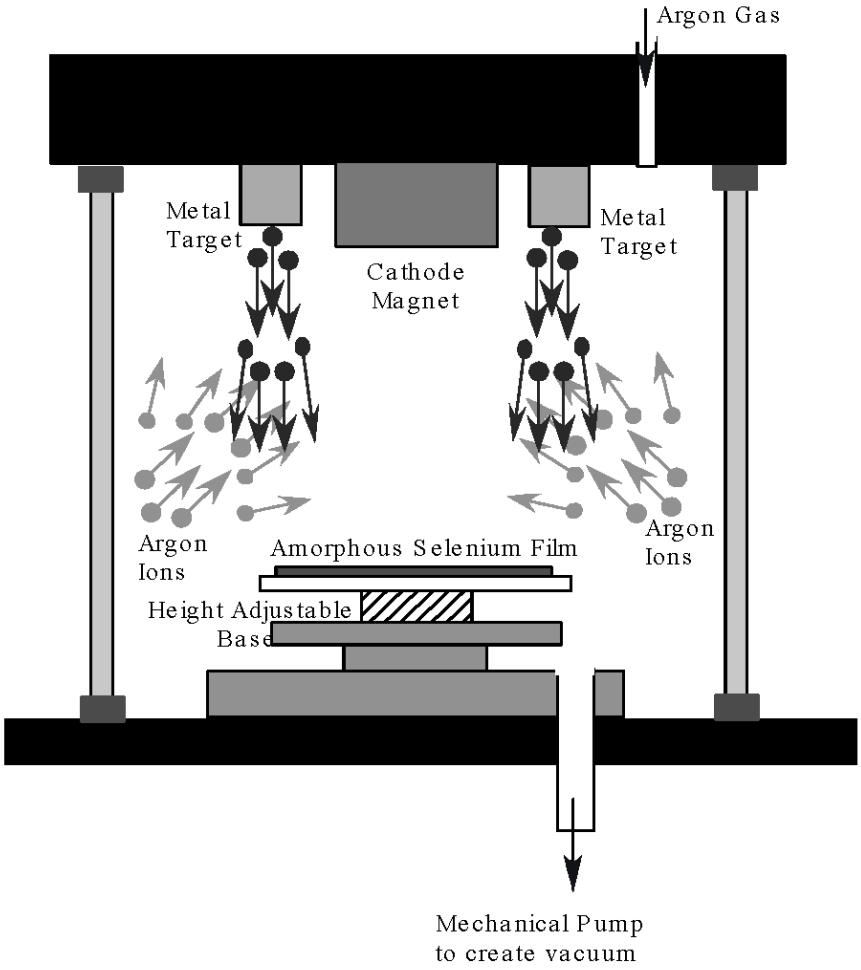

Figure 4.2: Schematic diagram of the sputterer used for depositing gold and platinum to prepare top and bottom electrodes.

4. The outside ring of the base is not fully covered by the sample and the mask, which can result in a poor conduction through the argon plasma

Once the above conditions are met then the pressure inside the vacuum chamber is brought down to 80 milli-Torr. A constant flow of argon is maintained during the process. Once a constant vacuum is obtained, a high d.c. voltage is applied across the base and the cathode. The high voltage is maintained in such a way that it ensures a flow of 14 mA of current through the plasma for gold and 18 mA for platinum deposition. Depending on the desired thickness, sputtering continues for 7 to 10 minutes until a desired resistance of the electrode is achieved. Typically for the platinum electrodes the acceptable range of the resistance across 1 cm length is between 0.5KΩ to 5KΩ.

4.2.3 Deposition of Amorphous Selenium Layer

The deposition of a thick layer of amorphous selenium is done by thermal evaporation using a conventional stainless steel vacuum coater. Pure selenium pellets are used as the source. The purity of the a-Se pellets is measured by the supplier to be 99.9999%.

First, a typical load of 50 gm to 60 gm of selenium pellets made with desired amount of arsenic and chlorine is placed in the molybdenum boat of the vacuum coater as shown in Figure 4.3. A glass substrate with a bottom electrode is placed in the substrate holder and the substrate heater is placed on top of the holder. A thermocouple to measure the temperature of the substrate is attached near to the substrate holder. The growth is measured using a quartz crystal monitor. The bell-

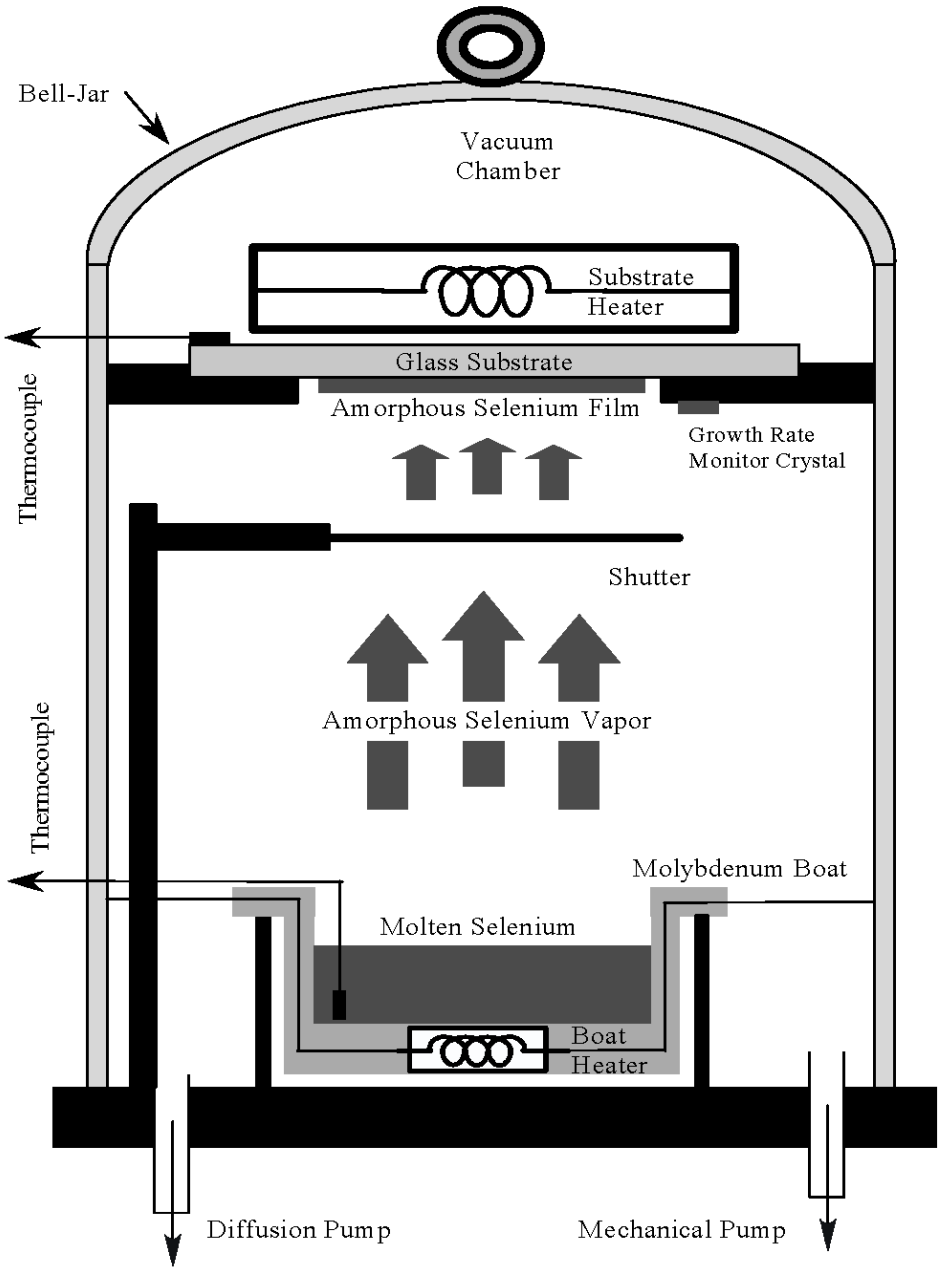

Figure 4.3: Schematic diagram of the amorphous selenium coater.

jar is closed and the system is pumped down to around 50 milli-torr with the help of the mechanical pump. The system is then pumped down to $P \approx 5 \times 10^{-7}$ torr using the diffusion pump. During evaporation the pressure increases to about 5×10^{-6} torr because of volatiles released from the pellets.

The shutter is kept at the closed position at the beginning of the evaporation process. The substrate temperature is maintained between 50°C to 70°C. The boat heater temperature control is set to between 240°C to 265°C depending on the desired evaporation rate, and the current through the heater filament is set to 120 A; once the evaporation rate is stabilized at typically 10 Å/sec and the substrate temperature reaches its desired level, the shutter is opened allowing the a-Se vapor to reach the substrate. A layer of amorphous selenium is then formed on the substrate. The thickness of the layer is constantly monitored, once the desired thickness is reached the shutter is closed to prevent further deposition. The boat heater is turned off, but the diffusion pump continues pumping until the boat temperature cools down to below 45°C—the glass transition temperature of stabilized amorphous selenium—before the bell-jar is opened. The amorphous selenium film is maintained at the stated substrate temperature until the boat and the chamber have cooled down. The substrate heater is then turned off and the sample is ready to remove from the coater once the substrate temperature reaches 30°C.

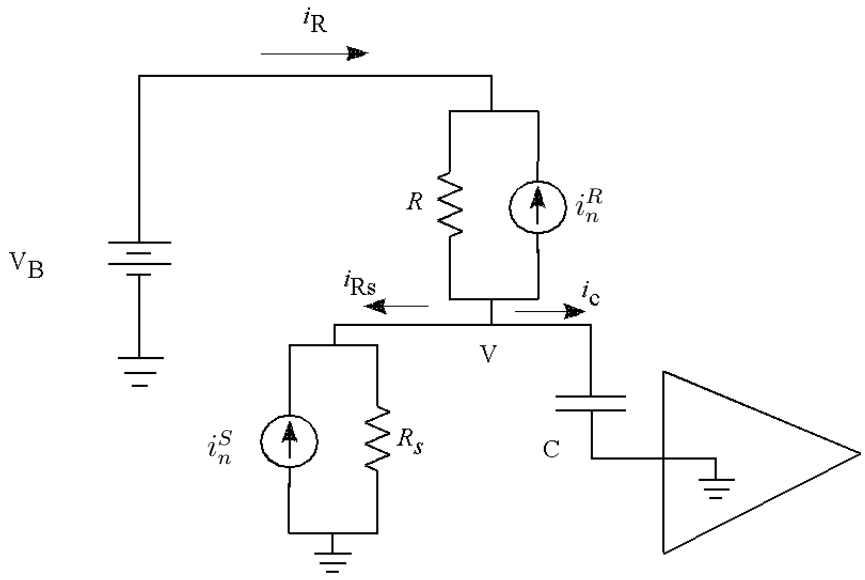

Figure 4.4: Noise equivalent circuit model of the experimental setup.

4.3 Circuit Analysis of the Experimental Setup

The Equivalent circuit of the experimental apparatus used to measure the noise is depicted in the Figure 4.4. In the circuit, V_B is the biasing voltage, R_s is the sample resistance which fluctuates, i_n^s is the thermal noise of R_s, which is always present under any biasing conditions. R is a series resistance and its thermal noise is i_n^R. C is a coupling capacitor, used to block DC from the low noise pre-amplifier. The fluctuating current i_c is the current that we need to measure for noise. R_s can be expressed as follows:

$$R_s = R_{so}(1 + \delta_{Rs} e^{j\omega t}) \tag{4.1}$$

where we are considering only a specific frequency. Since only linear terms will be

retained in the analysis, we can dispense with the Fourier integral over frequency normally required for the randomly varying resistance. Here

$$V = V_o(1 - \delta_v e^{j\omega t}) \tag{4.2}$$

Now, applying the current law at node V we get,

$$i_{Rs} = i_R + i_c \tag{4.3}$$

Hence,

$$\frac{dv}{dt} = \frac{V_B}{R_S C} - \frac{V}{R_S C} - \frac{V}{RC} \tag{4.4}$$

Solving equation 4.4 and neglecting the non-linear terms the following expression for δ_v is obtained:

$$\delta_v = \frac{Z_c}{V_o R_{so}} \frac{\delta R_s (V_B - V_o)}{1 + \frac{Z_c}{R_{So}} + \frac{Z_c}{R}} \tag{4.5}$$

Now, $i_c = Cdv/dt = -j\omega C V_o \delta_v e^{j\omega t}$, and taking the RMS value gives, $i_c = -j\omega C V_o \delta_v$

Therefore, applying the value of δ_v from equation 4.5 we get,

$$i_c = -\frac{\delta R_s}{R_{so}} \frac{(V_B - V_o)}{1 + \frac{Z_c}{R_{So}} + \frac{Z_c}{R}} \tag{4.6}$$

$$\therefore i_c = -\frac{\delta R_s V_B}{R_{so} + R} \frac{1}{1 + \frac{Z_c}{R_{So}} + \frac{Z_c}{R}} \tag{4.7}$$

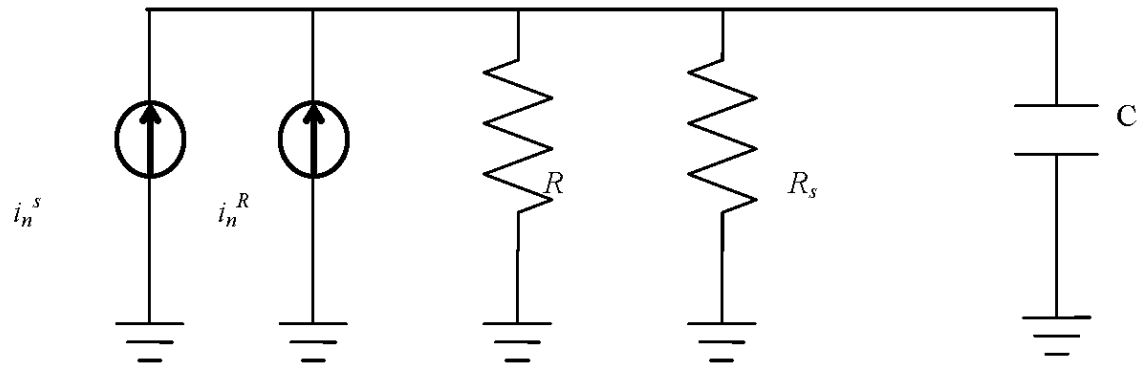

Figure 4.5: Simplified noise equivalent circuit model of the experimental setup.

Including the thermal noise currents, the total noise current is $i_n = i_n^S + i_n^R$, and solving the circuit we get, $i_n = i_R + i_{R_S} + i_c$, where i_c is the current through the capacitor.

$$i_n = \frac{V}{R} + \frac{V}{R_S} + \frac{V}{Z_c} \tag{4.8}$$

$$\therefore i_n = \frac{V}{Z_c}\left(1 + \frac{Z_c}{R_S} + \frac{Z_c}{R}\right) \tag{4.9}$$

Therefore, total current through the capacitor is,

$$i_C = \left(i_n - \frac{\delta R_s V_B}{R_{so} + R}\right)\left(\frac{1}{1 + \frac{Z_c}{R_{So}} + \frac{Z_c}{R}}\right) \tag{4.10}$$

This i_c is the total current that is fed to the pre-amplifier and then amplified and analyzed for our noise measurement.

4.4 Noise Measurement Apparatus

The apparatus used to measure noise is depicted schematically in Figure 4.6. A constant voltage (biasing) is applied to the sample through a voltage divider consisting of a low-noise resistor R and the sample R_S. The fluctuations of R_S induce corresponding changes in the current that are coupled through the capacitor C to the low-noise current pre-amplifier (ITACHO 564 or EG&G Signal Recovery 5182 pre-amp). The pre-amplifier has a very low level of noise current for the amplification range of 10^8 V/A, which is 45 fA/$\sqrt{\text{Hz}}$ referenced to the input. The capacitor acts as a DC blocking capacitor which blocks the biasing DC current from the amplifier's input which is a virtual ground. The capacitor along with the resistors of the voltage divider creates a high-pass filter that limits the ability to measure low-frequencies. The lower cut-off frequency is $(1/R_s+1/R)/2\pi C$. Since generally $R \ll R_s$ the cut-off frequency is just $\frac{1}{2\pi RC}$, which is 16 mHz for the values of R and C used in this project. A low noise voltage amplifier (EG&G 5113) further amplifies the noise signal. This signal is then fed to the spectrum analyzer (Stanford Research Systems SRS785). The spectrum analyzer calculates the Fourier Transform of the noise signal, does averaging and displays the power spectrum. Data is then transferred to a computer through the GPIB (IEEE 488) port using Labview software. A four-pole Butterworth filter is connected just after the voltage source. It has a cut-off frequency of 0.16 Hz,

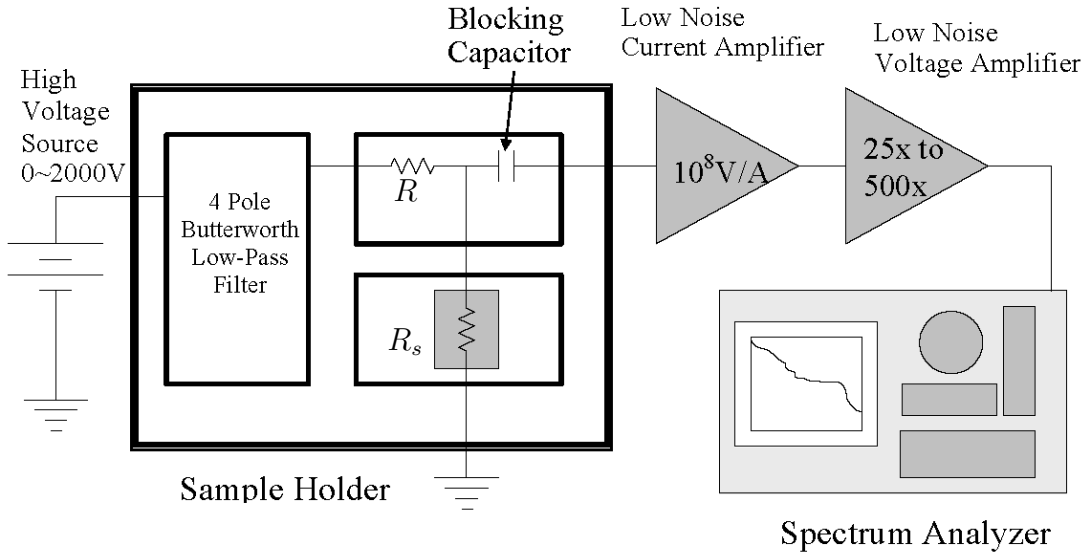

Figure 4.6: Schematic diagram of the experimental setup for noise measurement.

which suppresses any residual fluctuations from the high-voltage power supply. The sample holder along with the low-pass and the high-pass filters are enclosed in a shielded box to protect the experiments from outside noise sources.

A pictorial view of the experimental setup is shown in the Figure 4.7. where the black box in the left bottom corner is the sample holder, specially designed for noise experiments. The equipment sitting on top of the sample holder is the low-noise voltage amplifier and the unit sitting on top of the voltage amplifier is the low-noise current preamplifier. The bulky unit on the right hand side is the spectrum analyzer with built-in anti-aliasing filter that produces the noise spectra using the Fast Fourier

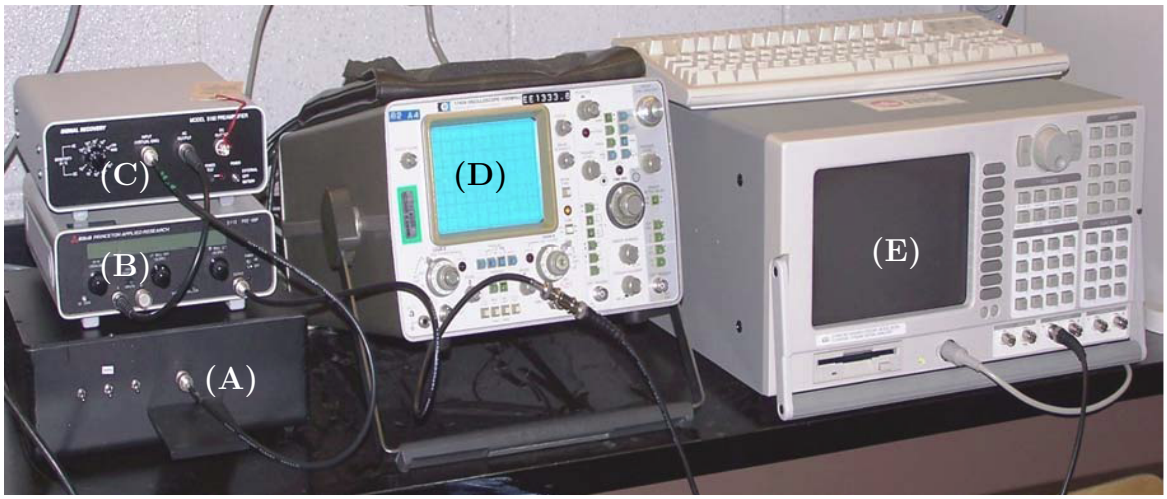

Figure 4.7: Pictorial illustration of the bench-top experimental setup. (A) The sample holder, (B) Low noise voltage amplifier, (C) Low noise current amplifier, (D) Analog oscilloscope and (E) Spectrum Analyzer.

Transform technique.

4.4.1 High Voltage DC Source

Amorphous selenium is a highly resistive material and needs to be biased with a high electric field to get sufficient d.c. current for noise measurements. To provide with a large electric field a high voltage dc source (EG&G Ortec model 556H) is used in this project.

The Ortec 556 is a reliable high voltage dc source that can produce up to 3000 V with a current ranging from 0 to 10 mA and a maximum overload current of 20 mA. The most attractive feature of this model is that it can be used in low-noise applications. The switching power supply of this particular model makes it different than the other high voltage d.c. power supplies as it produces less noise.

A pictorial illustration of the high voltage dc source is given in Figure 4.8. The

Figure 4.8: The high voltage dc source.

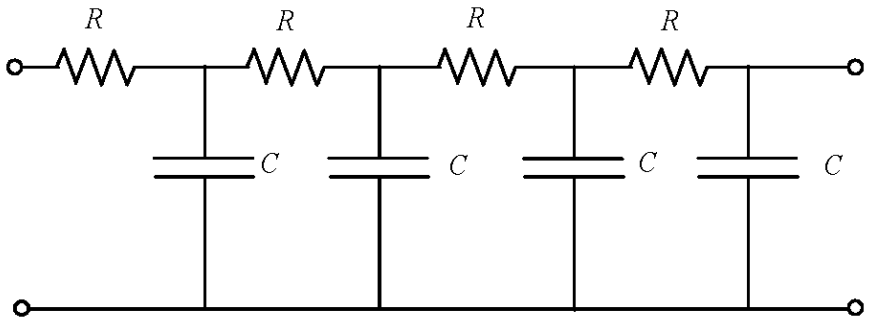

Figure 4.9: 4-pole low pass Butterworth filter attenuating noise over 145 mHz.

top most knob is for setting up coarse voltage with steps of 500 V. The middle knob is for setting up coarse voltage with steps of 100 V and the bottom one is for setting up fine voltage ranging from 0 to 100 V. Any level of desired voltage can be achieved with the help of these three voltage selectors.

4.4.2 Low-pass Butterworth Filter

One of the most effective ways to prevent electrical noise entering into the measurement is to use a low pass filter after the dc voltage source. Although the specifications of Ortec 556 dc voltage sources suggest that it can be connected to a low-noise system; an additional low-pass 4-pole Butterworth filtering unit is used at the output of the dc source unit to reduce the interference from the power supply.

Each section of the *RC* filter is constructed with six metal film resistors of 200KΩ each connected in a series providing a total of 1.2MΩ resistance in parallel with a 1μF non-polarized capacitor that can withstand 2000 V across it. Early research

shows that metal film resistors less than 1MΩ produces low $1/f$ noise. A series of resistors reduces the probability of a large voltage drop across each resistor. The time constant from this RC combination is 133 mHz. As a consequence noise spectra of samples were not measured below 0.5 Hz.

4.4.3 High Pass Filter

The coupling capacitor before the current pre-amplifier forms a high pass filter with the resistors of the voltage divider including the sample. In Figure 4.6, the high pass filter section is shown in a box before the current pre-amplifier section. The current pre-amplifier, Ithaco 564 is designed in a way that the voltage at the output should not exceed 5 V. With the gain set at 10^7 V/A, the input current is limited to 0.5 μA. The noise current, along with the biasing dc current, fed from the voltage divider without any filtering can easily overload the current amplifier. The capacitor of this filter blocks the dc current and allows only the noise current to flow to the following stage and hence prevents overloading. The measurements are limited to only the higher gain setting of the amplifier as the higher gain settings produces lower internal noise.

To build the high pass filter, a series of ten 1MΩ metal film resistors is connected with a 1μF, 2000 V non polarized capacitor. A single 10MΩ resistor produces more $1/f$ noise. The reason for using a high resistance is to reduce the Johnson noise. A higher resistance would increase the RC time constant, hence requiring a longer waiting time. The combination of this RC has a cutoff frequency of 40 mHz.

4.4.4 Circuit elements of the filters and the sample enclosure

Both the low pass and the high pass filters are made of passive elements, resistors and capacitors, which may seem somewhat trivial. But these components must be carefully chosen so that they don't adversely affect the noise measurement of a very low level signal. Metal film resistors were chosen to minimize $1/f$ noise from the resistor itself. Though the metal film resistors exhibit a slightly higher level of $1/f$ noise compared to the wire-wound types, the large resistance values needed preclude using wire-wound resistors. Other types such as carbon composition and glazed metal were tested and found to have excessive amount of $1/f$ noise.

Non-polarized capacitors were used to avoid the intrinsic fluctuations found in any capacitor that uses an electrolyte and to allow both positive and negative dc voltages to be applied. It was very difficult to get non-polarized capacitors of 1 μF capacitance or more that are rated to 2000 V dc, fortunately, one vendor had just 10 in stock.

Instead of the regular BNC (Bayonet Neill-Concelman) connectors, a semi high voltage connector (SHVC) was used to feed the input dc voltage to the low pass filter at the input stage. The SHVC connectors are designed to use up to 5000 V. All other low voltage connections were provided with regular BNC connectors. Solder flux between the center pins and the grounds of the BNC connectors provides current paths and hence produces leakage current. In the case when the noise signal level is quite low, the leakage current can affect the noise measurement. To prevent the solder flux getting into the insulator area of the BNC a special care is taken while

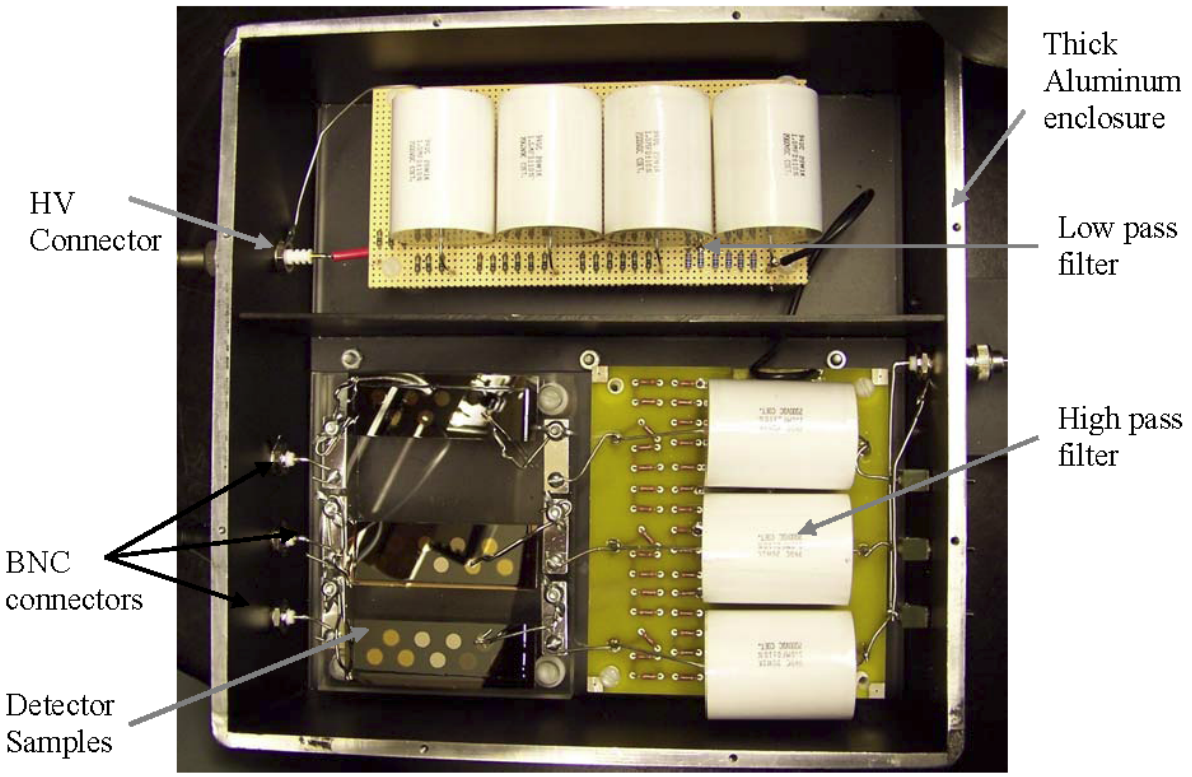

Figure 4.10: Sample enclosure (Uncovered).

soldering the wires. All flux was cleaned from the BNC insulators. After each connections the BNCs were tested for leakage current with the electrometer.

Another potential problem is the vibrations in the wiring. There is always a capacitance, say to the nearest ground point or to the walls of the box, that will depend on the distance. As the wires vibrate the capacitance changes and currents are induced in the measurement circuit. In other applications such currents are small and can be ignored but the sensitivity required for noise measurement makes these induced currents significant. Because of this sensitivity all wiring is either tied down or made with very stiff heavy gauge wire. In spite of those precautions, there is still some sensitivity to vibrations and so I took care to isolate the measurement apparatus from vibration sources.

Pressure contacts made with nickel-chromium wires were used to get the noise signal from the top electrodes of the samples. NiCr wires are stiff and relatively immune to vibration. Stiff wires produce significant force on the top contact and sometimes scratches the metal. Moreover, the edges of contact-wires have many microscopic point which results in poor contact to the electrode. To eliminate both the scratching and poor contact, a piece of soft metal such as indium or gold was placed between the contact and the top electrode.

A picture of the sample enclosure is shown in the Figure 4.10. The low-pass filter, the sample holder and the high-pass filter are enclosed in a metal box made of thick aluminum so that no external electrical noise can affect the noise measurements. Signal with the lid off show a great amount of signal pickup from other equipment mostly the 60 Hz mains and its harmonics. All the output connections from the

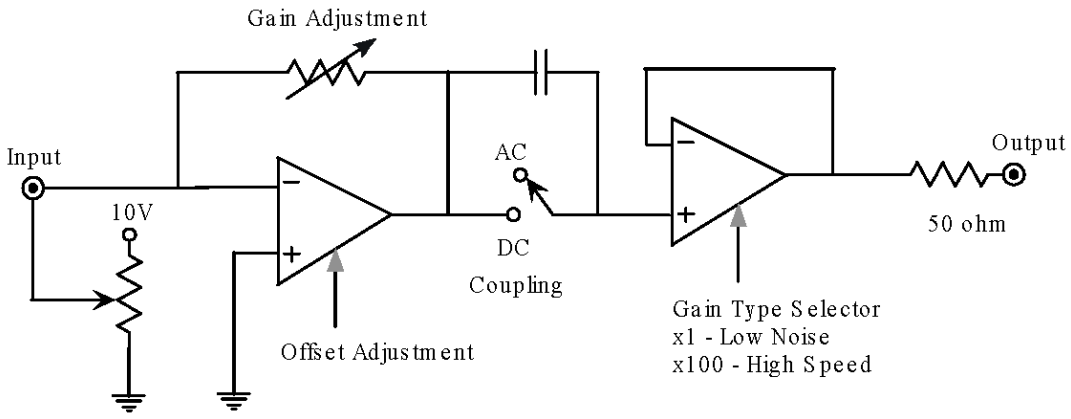

Figure 4.11: Schematic diagram of the Ithaco 564.

sample holder enclosure were made through the BNC connectors. All other interconnections between the sample holder enclosure and the other measurement units were made with standard RG-58 coaxial cable of 50Ω impedance.

4.4.5 Current Pre-Amplifier

Two current amplifiers with different trans-impedance settings were used for the noise measurements. The Ithaco 564 current preamplifier was used for gains from 10^4 V/A to 10^7 V/A while the EG&G *Signal Recovery* 5182 was used for the gain of 10^8 V/A. The later has a better bandwidth for the 10^8 V/A range. A simplified diagram of the Ithaco 564 amplifier is shown in Figure 4.11. A selectable voltage buffer is attached to the output of the current to voltage amplifier section to provide either low-noise or high-speed operation. The low-noise option has less background noise but about $10\times$ less bandwidth. Since for $1/f$ noise the lower frequencies are

more important, all the noise measurements used the low-noise setting at 10^7 V/A amplification. The 10^8 V/A setting of the Ithaco 564 amplifier was unsuitable because the bandwidth is less than 1 kHz, which does limit the $1/f$ noise measurement. Both sections of this unit were ac coupled for all the measurements. The bias and offset adjustments were set to zero. The input of the Ithaco 564 is a virtual ground that prevents loading of the circuit and also reduces the effects of source and cable shunt capacitance.

The EG&G *Signal Recovery* 5182 is a similar type of current pre-amplifier with a better noise figure and bandwidth than the Ithaco 564. With the setting of 10^8 V/A low-noise, this unit starts showing a high-frequency roll off around 10 kHz and has a noise level of 15×10^{-15} A/$\sqrt{\text{Hz}}$ referenced to the input. The noise level of the Ithaco 564 is 41×10^{-15} A/$\sqrt{\text{Hz}}$ for the 10^7 V/A range.

Both the *EG&G Signal Recovery* 5182 and the Ithaco 564 are powered by a set of four external rechargeable sealed lead-acid type batteries. One 12 V battery is connected in series with a 6 V battery to produce the required 18 V. The other pair of batteries provides -18 V. The reason for not using an ac power supply unit was to eliminate the 60 Hz signal and its harmonics from the mains. The batteries are enclosed in an aluminum box to isolate them from the ambient noise signals and the connections to the amplifiers are made through a shielded cable.

4.4.6 Voltage Pre-Amplifier

In order to match the signal level to the input range of the spectrum analyzer the output voltage of the current pre-amplifier is further amplified using a voltage

pre-amplifier EG&G model 5113. It amplifies the input voltage from 1× to 50,000× with an accuracy of ±2%. The referred-to-input noise specification for the amplifier is 4 nV/$\sqrt{\text{Hz}}$. The EG&G model 5113 has a built in filter stage with three different types of response, i.e. low-pass, band-pass and high-pass. For the measurements of this project, the internal filter was set to a high pass filter with a 300 kHz cut-off frequency and a 12 dB/decade roll-off. The input of the amplifier was always set to the ac coupling.

The voltage pre-amplifier unit is battery operated with internal rechargeable lead-acid batteries. The amplifier is microprocessor controlled, however, the processor is put to sleep during measurements to avoid high frequency signals from the clock being injected into the amplified signal.

4.4.7 Spectrum Analyzer with Built in Anti-Aliasing Filter

In general, the spectrum of the noise signal is of primary importance. A Stanford Research Systems SR785 spectrum analyzer is used to calculate an averaged noise spectrum from the amplified signal.

The analyzer first digitizes the input signal at 262 kHz; all further analysis uses digital signal processing. In order to maintain the integrity of the information contained in the input noise signal, this signal must be band limited to less than half of the sampling frequency. This frequency is known as the Nyquist frequency. To make sure that Nyquist's theorem is satisfied, the input signal is passed through an analog anti-aliasing filter before digitization that removes all the frequency components above the Nyquist frequency.

The noise power spectral density is calculated using

$$S(f_i) = \frac{2|X(f_i)|^2}{N\tau} \tag{4.11}$$

where data in the frequency domain $X(f_i)$ is the discrete fourier transform of the digitized signal, τ is the period between data points, N is the total number of points and f_i are the frequency points spaced equally by $1/(N\tau)$ from 0 to $1/(2\tau)$ [8]. However, noise spectra are usually graphed on a log-log plot, so equally-spaced points in frequency are crowded at the high frequency region on the log scale and quite sparse in the low frequency region. In order to obtain a more uniform distribution of points data were taken in three different frequency windows with three different τs. A larger τ for the low frequency window and then a smaller τ for the mid-frequency window and the smallest τ for the high frequency window. For this project the frequency span for the lower frequencies is 0.5 Hz to 13 Hz with spacing 62.5 mHz. The mid-frequency window starts at 13 Hz and ends at 813 Hz with a spacing of 1 Hz. The high frequency window spans 813 Hz to 52 kHz with a spacing of 64 Hz. The combined spectra starts at 0.5 Hz and goes to 52 kHz and has a reasonable density of points at all frequencies.

Each spectra is obtained from Eq. 4.11 by calculating the Fourier transform using a FFT algorithm. A spectrum produced by a single transform is not useful because the "noise" in the spectrum is quite large. An average over many transforms must be performed in order to obtain a smooth spectrum. Typically 3000 transforms are averaged together for the lower frequency window, 5000 for the mid-frequency and

10000 for the high-frequency window. Acquiring the spectrum for the low-frequency window takes the longest time—about 2 sec. per transform. The choice of 3000 averaged transforms is a compromise between the total time of measurement and the desired smoothness of the resulting spectrum. The upper two frequency windows are acquired much more rapidly and the number of transforms averaged simply produces a smooth-looking curve.

Interference from the 60 Hz mains and its harmonics is inevitable in noise measurements. However, this interference produced a set of sharp features, spikes, superimposed on the noise spectrum, and the spikes can be either ignored or manually removed before further analysis. The percentage of data points affected by the spikes always remains less than or around 1% of the total number of data points.

Besides the interference from 60 Hz and its harmonics, the only other significant background noise sources are the Johnson noise from the resistances R and R_s and the noise of the current amplifier. In order to remove the background noise, a noise spectrum was obtained without applying a bias voltage, hence without any bias current flowing through the sample. This spectrum should not contain any $1/f$ noise, just the background noise. Spectra are then measured with different bias currents. The background noise spectrum is subtracted from these leaving just the $1/f$ noise spectra.

This procedure is able to give reliable $1/f$ noise data even when the $1/f$ noise is less than the background noise. However, once the $1/f$ noise becomes about $10\times$ less than the background, there is too much residual fluctuations in the background data and the $1/f$ noise data can not be seen.

One background noise source that can not be removed by this procedure is shot noise, since the shot noise is only present with a bias current. Fortunately, for reasons mentioned previously, shot noise is rarely seen in these experiments.

4.4.8 Software to Collect Data and Measure Noise Spectra

In order to collect data from the spectrum analyzer, two different methods were used in this project. First, the data were collected with the help of the built-in floppy drive of the analyzer and then recorded in double-sided High Density (HD) magnetic floppy disks. The recorded data were then transferred to the computer and converted to the ASCII format with the help of converter software srt785.exe. The ASCII file was then converted to the Excel format for further analysis. The other method of collecting data was by using the Labview 7.1 software in conjugation with a General Purpose Interface Bus (GPIB) card through a GPIB cable; the collected data from the Spectrum Analyzer were transferred directly to the personal computer system. In the latter method, data were saved in the Microsoft Excel format and with the help of the appropriate formulas the noise power spectral density was produced. A labview program was written to transfer data from the spectrum analyzer to the computer.

4.5 X-ray Apparatus

The effect of X-rays on $1/f$ noise was measured in the later part of the project. Several doses of X-ray were shone on the multilayer p-i-n and n-i-p structured sam-

ples. The X-ray source used to shine X-ray on the a-Se photoconductor layers is a Gendex GX-1000 dental X-ray system placed inside a lead X-ray isolation chamber. This unit is made of a relatively small X-ray tube and a separate control unit. The tube head contains a tungsten anode with 2.5 mm internal Al filtration along with a hot filament cathode to release electrons. The electrons are accelerated by a large electric field. These high energy electrons hit the anode at a high velocity to produce a wide spectrum of X-ray radiation and heat. The X-ray head was positioned at $4 \sim 5$ cm directly above the sample. The tube head is surrounded by an oil-filled lead enclosure in order to dissipate the heat generated by the accelerated electrons. The total system was enclosed inside in the isolation chamber.

The tube current of the Gendex system can be set to 10 mA or 15 mA and the tube voltage can be varied in the range from 50–100 kVp. The exposure duration can be set to different values in the range 3/60 sec to 5 sec. The X-ray beam consists of a series of 1/60 second impulses due to the self rectifying nature of the tube and the 60 Hz power supply. Hence the number of pulses can be set from 3 impulses to a train of 300 impulses for each exposure. The temperature of the anode increases while the beam is on which limits the duration of the X-ray output so as not to damage the tube. However, for larger currents, the total time is further restricted so that the number of "heat-units"is less than 4000 where a heat-unit is defined as

$$\text{Heat unit} = \text{Current(mA)} \times \text{kV}_p \times \text{Exposure time(in seconds)} \tag{4.12}$$

Table 4.1: Maximum allowable number of exposure seconds in a 5 minute period.

kV_p	No of exposures in a 5 minute time span at the setting of a 5 second train of exposures	
	10mA Setting	15mA Setting
50 - 70	30	20
80	26	17.5
90	23	15.5
100	21	N/A

The following equation is applied to get the amount of radiation emitted by the anode. The X-ray output of the tube, Q, is defined by,

$$Q = k \times I \times t \times V^2 \tag{4.13}$$

where k is a constant that depends on the tube characteristics, I is the anode current, t is the exposure time and V is the tube voltage [45]. The anode current can be controlled by adjusting the filament current.

The magnitude of the X-ray exposure was measured using a Keithley 96035 ionization chamber connected to a keithley 35050 dosimeter. The dosimeter produces a voltage reading that is proportional to the X-ray exposure. The proportionality factor was calibrated at the Cancer Center at the Royal University Hospital, University of Saskatchewan using a standard calibration procedure. To measure the exposure, the ion chamber was placed between the X-ray tube and the sample. The output of the dosimeter was connected to a Fluke 8000A digital multi-meter to measure the corresponding voltage from the X-ray exposure.

The most common method of measuring X-ray exposure is to determine the

amount of ionization that the beam produces in air. The degree of ionization is nearly proportional to the radiation exposure under certain controllable conditions [46]. One roentgen is the amount of radiation exposure which when passed through 0.001293 g of air at the Standard Temperature and Pressure (temperature of 0^oC at 760 mm Hg pressure) produces ionization in this 1 cm^3 of air with the appearance of a defined number of ions and electrons. This is called corpuscular emission [47]. This results in a charge of 0.000258 C/kg in air under standard conditions. The rate of exposure of an X-ray beam can be controlled by the four factors,

1. current in the tube,

2. accelerating voltage,

3. filtration of the beam and

4. distance between the sample and the X-ray head.

The penetration depth of an X-ray beam can be increased by increasing the acceleration voltage which is not a linear function. The penetration of a particular beam is determined primarily by its photon energy spectrum. A higher voltage on the X-ray generator results in the electrons hitting the target material with a greater kinetic energy and results in a more higher energy photons and a greater penetrating X-ray beam.

In order to ensure a proper safety guideline when operating the X-ray equipment the unit along with the sample and the dosimeter is installed in a lead lined cabinet manufactured by X-ray Products Corporation of Pico Rivera, California. A photo-

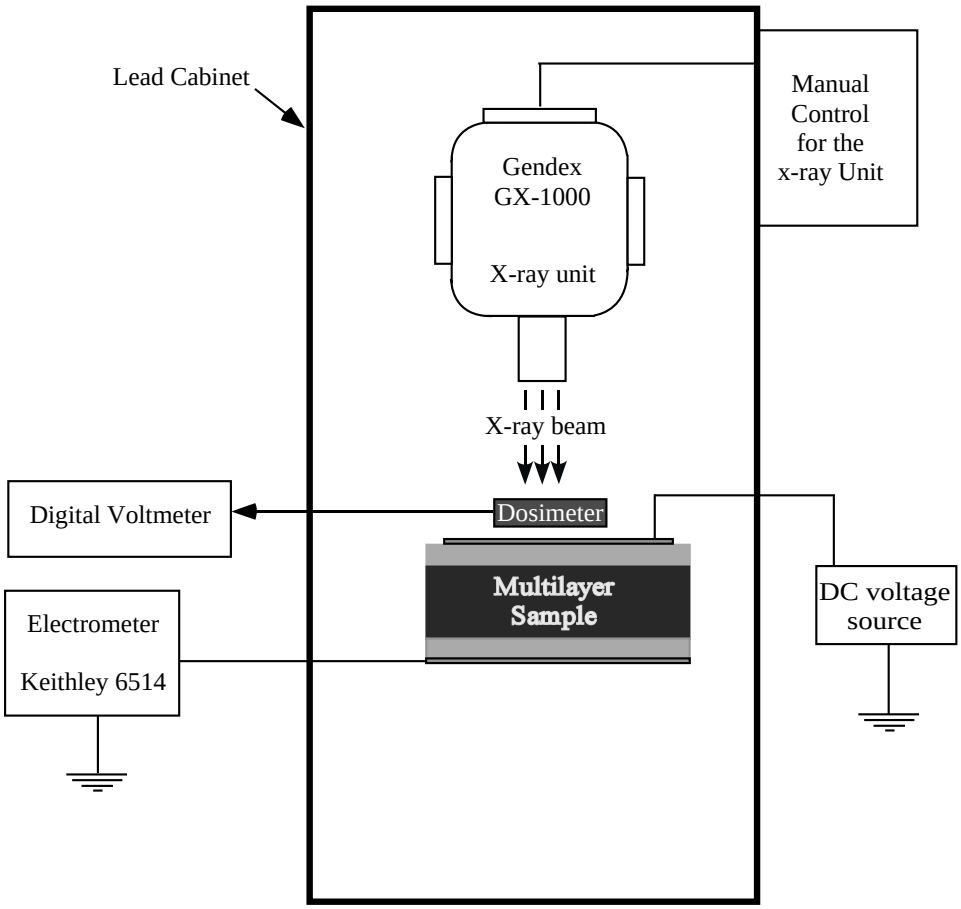

Figure 4.12: Schematic diagram of the experimental setup for X-ray measurements on multilayer samples.

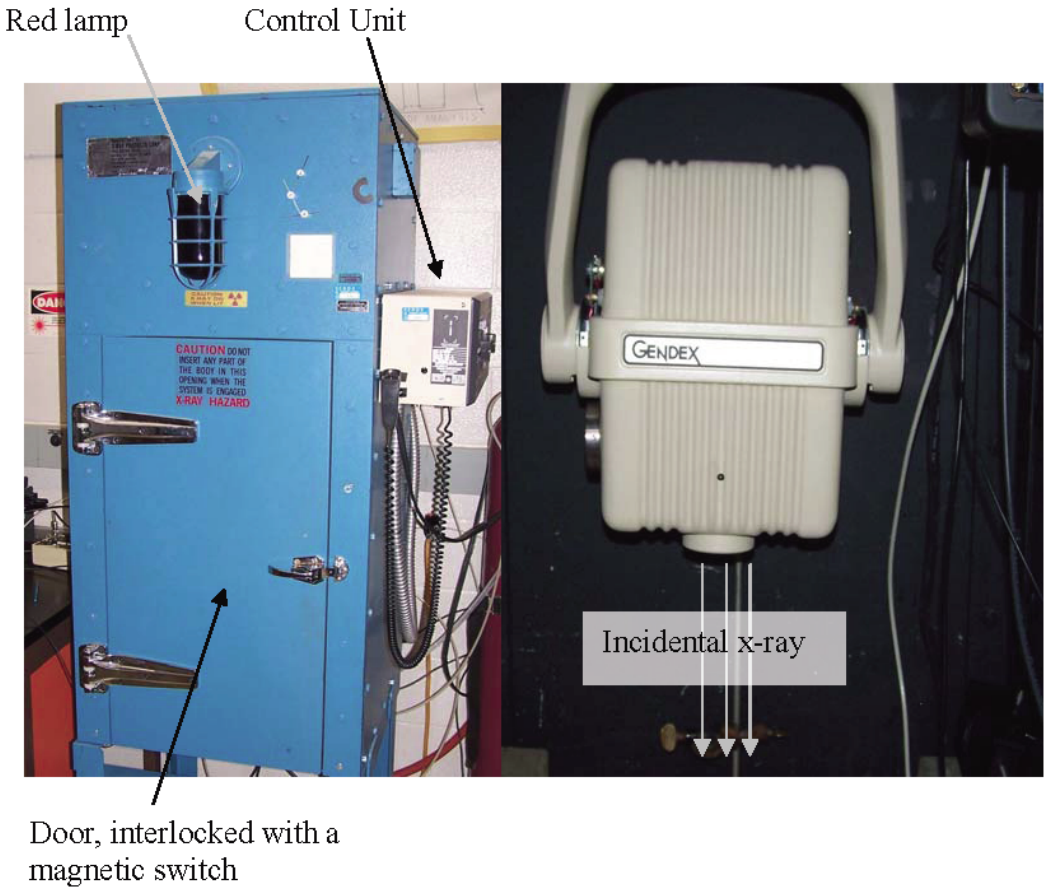

Figure 4.13: Pictorial illustration of the X-ray chamber. i) The lead cabinet with the external control and the safety features, ii) The X-ray head inside the lead enclosure.

graph of the external shielding and the Gendex GX-1000 dental X-ray head is shown in Figure 4.13, where an emergency light is seen at the front of the lead chamber, which is turned on when the X-ray system is in use. The control unit is seen in the right hand side of the chamber. A door is mounted at the front of the enclosure to facilitate access to the inside of the cabinet. A magnetic interlocked switch is fixed to the door to shut off the X-ray tube when the door is opened. There is a serpentine maze for cables near the top back of the cabinet.

A schematic diagram of the manually controlled experimental setup is shown in Figure 4.12, which was used to expose a multilayer sample to X-rays while a dc bias of 10 V/μm was applied to the sample. A Keithley 6514 digital electrometer is connected to the sample to measure the X-ray photo-current during the exposure. The manual control unit is attached outside the lead cabinet. A multilayer sample is placed underneath the X-ray head of the Gendex GX-1000 unit. A dosimeter is placed between the X-ray head and the sample to measure the dose of the incidental X-ray beam. A high voltage is applied to the sample via a SHV cable pulled through the top of the lead cabinet. The a-Se photoconductor layers were exposed to 14 Roentgen (R) of X-rays for 5 minutes.

4.6 Noise System Calibration

Section 4.4 outlined the procedure to calculate the noise power spectral density using Equation 4.11. It is necessary to collect data with an accuracy that will produce the best noise spectra possible. In order to do so, the various components of

the system were calibrated several times during the project. The calibrations were then incorporated in the final analysis. Response curves of the following equipment were measured from time to time:

1. Current to voltage amplifier

2. RC high pass filter

3. Voltage amplifier

The response of the RC low pass filter was not corrected for because it was tested with the system when the system was calibrated with a known resistance and found to be working properly. Some additional noise signal would show up in the noise spectra of the known resistors, if an additional amount of noise would have passed through the low pass filter. Control experiments used to verify the accuracy of data collection will be discussed in this section.

4.6.1 Response Curves

The response curves of both the current and the voltage pre-amplifiers are not flat. In particular, the response curves fall off above a certain frequency depending on the gain setting. In this project only one gain setting was used for each current amplifier, so, only one response curve is needed for each unit. There are several correction factors that needed to be determined having to do with the response of the amplifiers. Noise data are divided by the square of the response to correct for the non-linearity of the amplifiers.

Frequency response of the current amplifier

The manufacturer supplies a generic response curve for their amplifier, but for this project the response curve was measured typically once a year. The measurement consisted of applying a known ac voltage to a large resistor (10MΩ) to generate an ac current which is then input to the amplifier, and the output is measured. The frequency is varied across the range of interest and the response curve is built up. Figure 4.14 shows the response of the EG&G model 5182 pre-amplifier and Figure 4.15 shows the response of the Ithaco 564 amplifier.

An Agilent 33120A signal generator was used in order to determine the response curve of the current amplifiers for both the Ithaco 564 and the EG&G model 5182. Both the input and the output were measured by an Agilent MSO6014A mixed signal oscilloscope. The output was also verified with the spectrum analyzer. The gain of the amplifier was determined with the output/input ratio and was normalized with the average of the magnitude at the flat region of the response curve. Capacitances of the samples vary with the different sizes of contacts, which produces frequency response of different shapes, especially at the higher frequency ranges. Most samples typically fell in the range from 10pF to 100pF, but the samples with the largest top electrodes (21 cm^2) were close to 1nF. A difficulty is that the response at high frequency depends on the input capacitance. Curves were measured for minimal input capacitance and 1 nF. Two different response curves were used for calibration to get rid of the capacitance effect in the measured spectra.

The response curve of the current pre-amplifier is shown in Figure 4.14. To

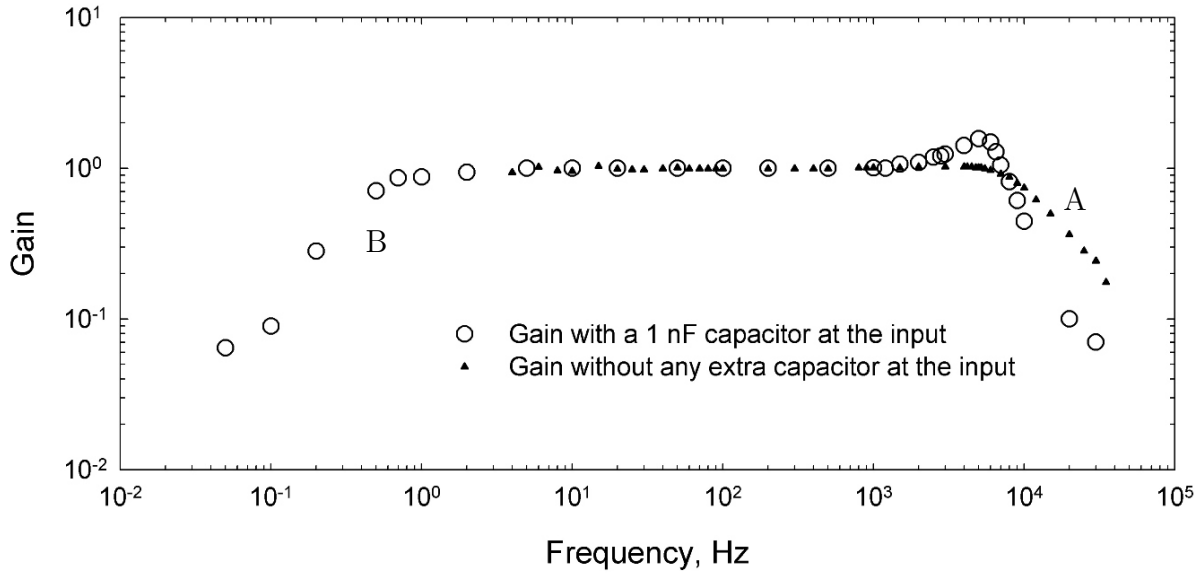

Figure 4.14: Response curve of the EG&G 5182 amplifier at 10^8 V/A low noise setting, curve (A) no extra input capacitance, and curve (B) with 1nF input capacitance.

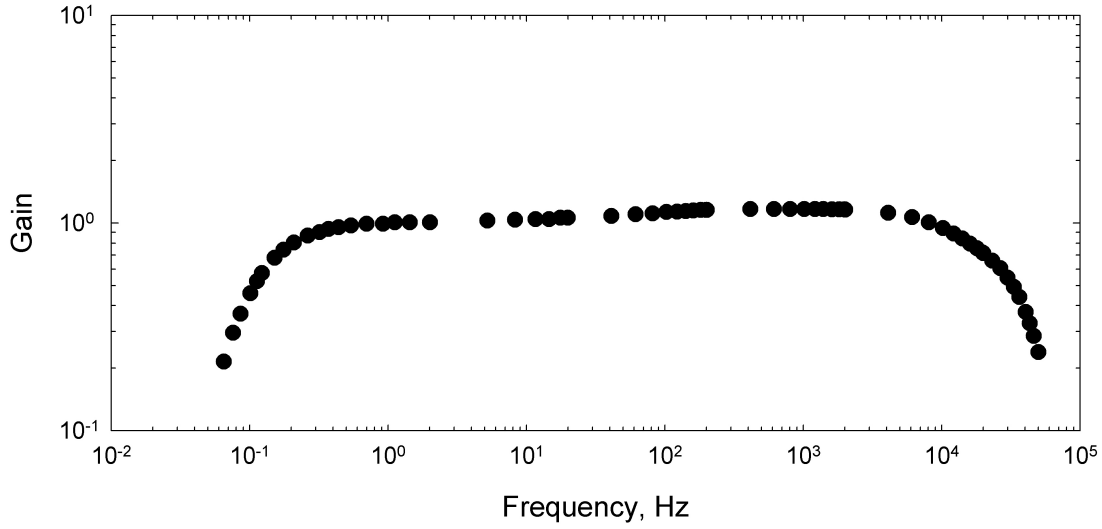

Figure 4.15: Response curve of the Ithaco 564 current amplifier with 10^7 V/A gain setting.

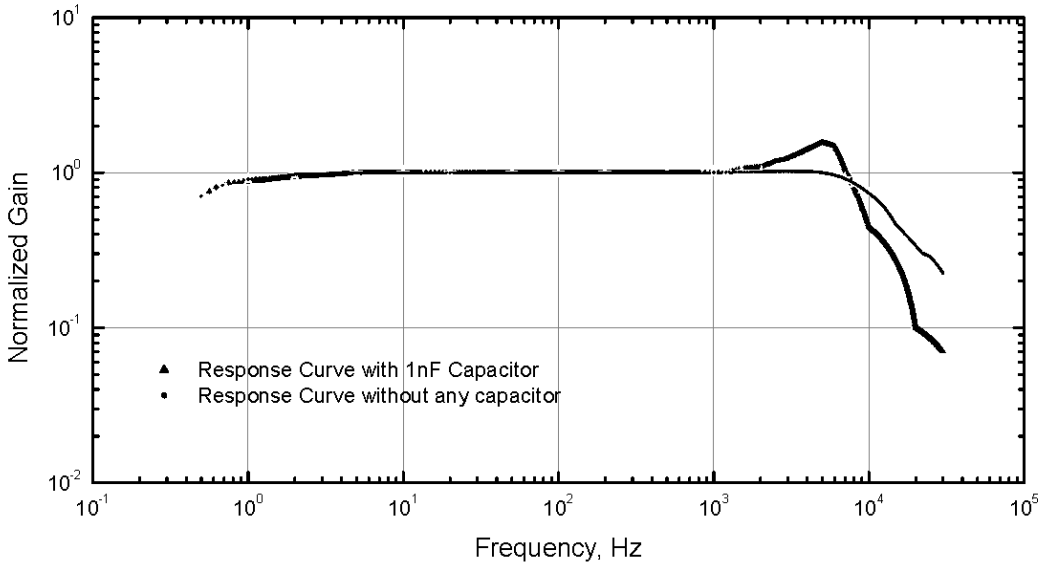

Figure 4.16: Response curve of the current amplifier set to the gain of 10^8 V/A.

obtain the linearly extrapolated response curve, a set of gain data has been recorded at different frequencies. With the help of this set of data the curve has been generated with linear equation and is shown in Figure 4.16.

The response data is then used in the noise analysis to correct all noise spectra. To test the frequency response correction, the white Johnson noise from a 90KΩ wire-wound resistor was measured and after applying the correction the spectrum is almost a perfectly flat (see next section).

Noise floor level of the current amplifier

Another important factor is the noise floor of the low-noise current pre-amplifier. This quantity establishes a lower limit on the noise magnitude that can be measured with this device. The noise floor of the amplifier was measured with the input open and capped using the spectrum analyzer SRS 785.

The measured noise floor level is shown in the Figure 4.17. $1/f$ noise is visible at the lower frequencies below 0.5 Hz. The noise measurements were not affected by the $1/f$ noise as the measurements started after 0.5 Hz. The noise floor in the frequency range of our interest is small compared to measured sample noise. An increase in the noise power is found at the higher frequencies due to the input capacitance of the amplifier.

4.6.2 System testing with the Johnson noise of a known resistance

The system was tested using the known Johnson noise of a 90KΩ wire-wound resistor. Using Eq. 3.8 from chapter 3, the expected Johnson current noise amplitude

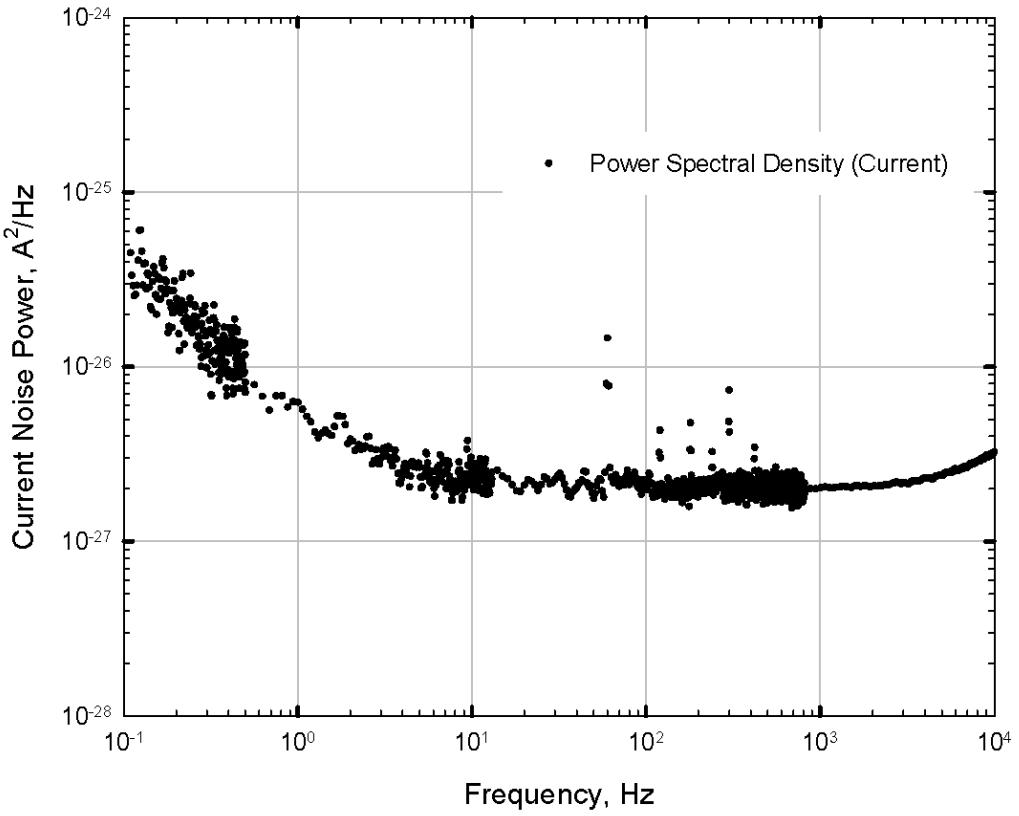

Figure 4.17: Noise floor of the *EG&G* 5182 at 10^8 V/A low noise setting.

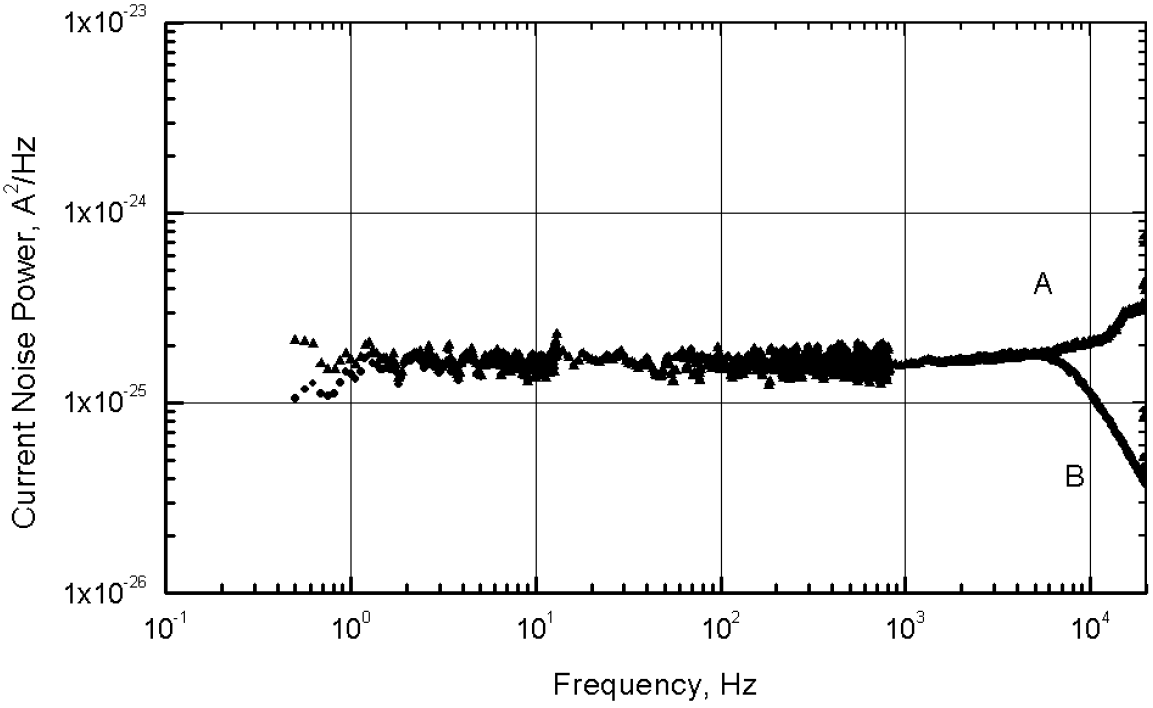

Figure 4.18: Measured Johnson noise power of a 90KΩ wire-wound resistor. (A) With amplifier response, and (B) without amplifier response.

is 4.25×10^{-13} A/$\sqrt{\text{Hz}}$ at room temperature 22 °C, which corresponds to the Johnson noise power 1.81×10^{-25} A^2/Hz . Figure 4.18 shows the measured spectrum for the 90KΩ wire-wound resistor before and after the corrections for the amplifier response.

A linear regression of the points after removing the points within 5 Hz of 60 Hz and 180 Hz as well as points above 1.5 kHz is shown in Figure 4.19. The linear fit of the shown data gives a slope of 0.006 and an average current noise power of 1.7×10^{-25} A^2/Hz. The zero slope is as expected for white noise and the magnitude is very close to the theoretical value. The rise at the highest frequencies in the response

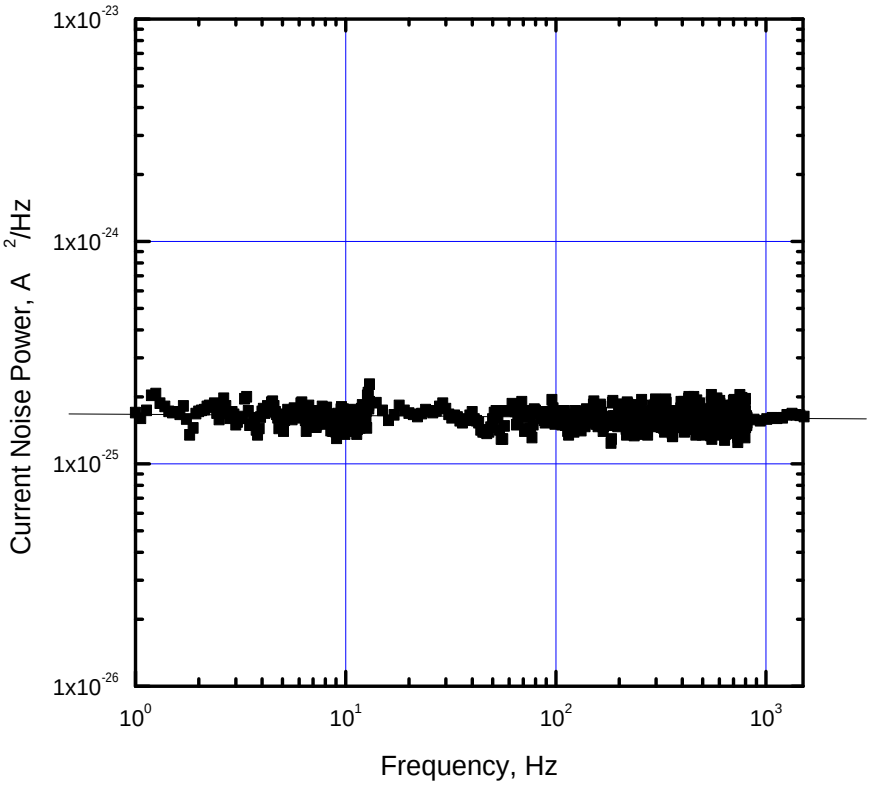

Figure 4.19: Measured Johnson noise power of a 90KΩ wire-wound resistor with the linear fit showing a straight line of 0.006 slope at 1.7×10^{-25} A^2/Hz.

curve is likely due to an impression of the input capacitance.

4.6.3 Testing the system for $1/f$ noise with pure resistive load

In this section the $1/f$ noise of a series of ten 1.2MΩ metal film resistors is presented. Metal film resistors are used in the filters as well as the biasing resistors in the resistor divider (R in Figure 4.6). It is important that the $1/f$ noise from these resistors is small compared to the sample's $1/f$ noise. The sample holder was

tested with a series of 1.2MΩ metal film resistors creating a resistive load of 12MΩ. The metal film resistors were chosen because the metal film resistors produce very low $1/f$. A series of 1.2MΩ resistors were chosen instead of a single 12MΩ because our measurement showed that metal film resistors with less than 10MΩ resistance value produces less $1/f$ noise. This test also establishes that the present system is capable of measuring low levels of $1/f$ noise. The 12MΩ test resistor was chosen to be similar to the voltage divider resistor. Any noise provided will come about equally from each resistor. Note that for the a-Se samples, the resistance is typically 1000 times larger than R. Hence a smaller bias current flows compared to this test and the $1/f$ noise from R is reduced accordingly.

Figure 4.20 shows the current noise spectra for the Johnson noise and $1/f$ noise of the 12MΩ test resistor and the 10MΩ resistor R for applied voltages of 500 V and 2000 V. Measured bias currents for 500 V and 2000 V were 18.7 μA and 74.8 μA respectively. Figure 4.21 shows how the $1/f$ noise scales when both spectra are normalized with the square of their respective currents after the Johnson noise is subtracted. This shows that the $1/f$ noise scales with bias current as expected for conductance noise. The noise power spectra fits a $1/f^{\alpha}$ power law with α equal to 1.2 after removing the points below 1 Hz and above 1 kHz.

4.6.4 Data Analysis

The method of data analysis and the processing steps to correct the data so that it can be referred to the input is described in this section. Description of the software and the programs have been discussed in section 4.4.8 under the heading Software

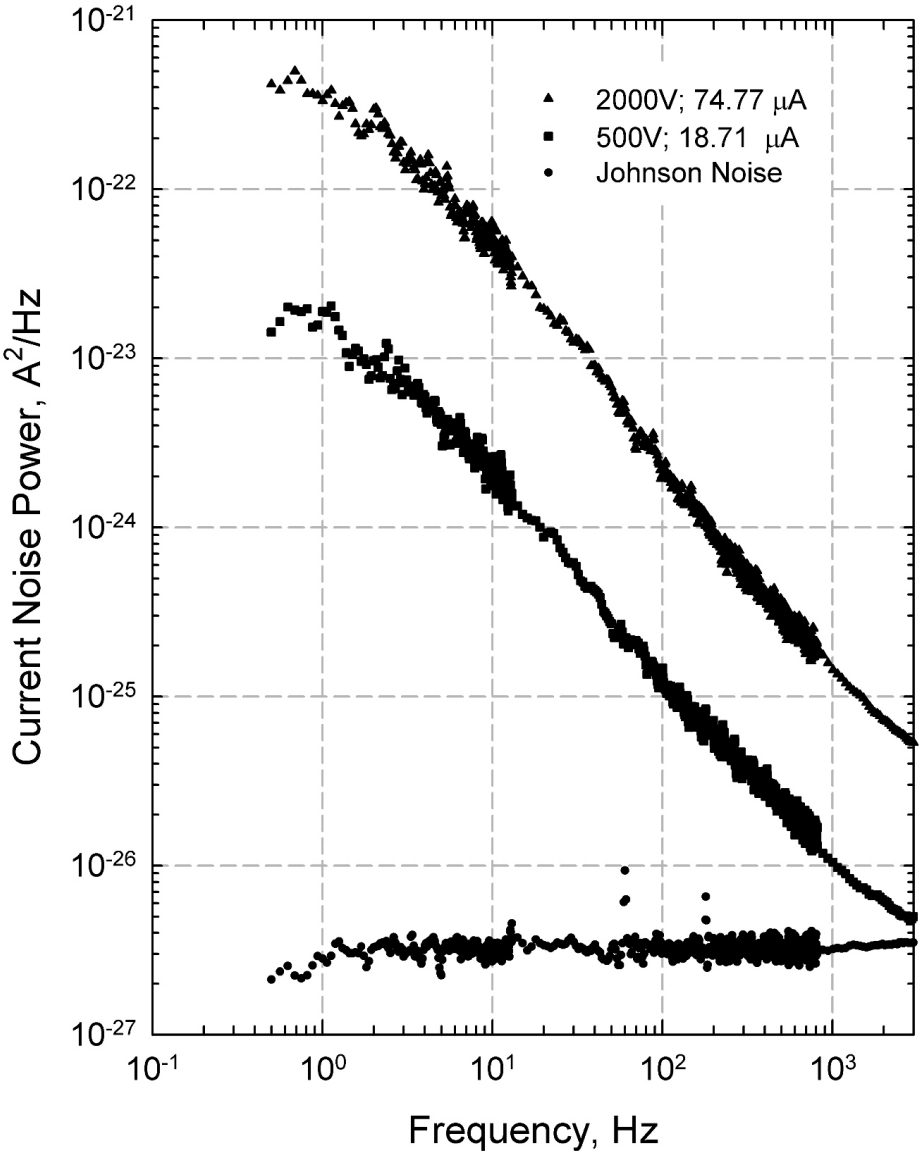

Figure 4.20: Current noise spectra showing the Johnson noise along with $1/f$ noise from 500 V and 2000 V biasing.

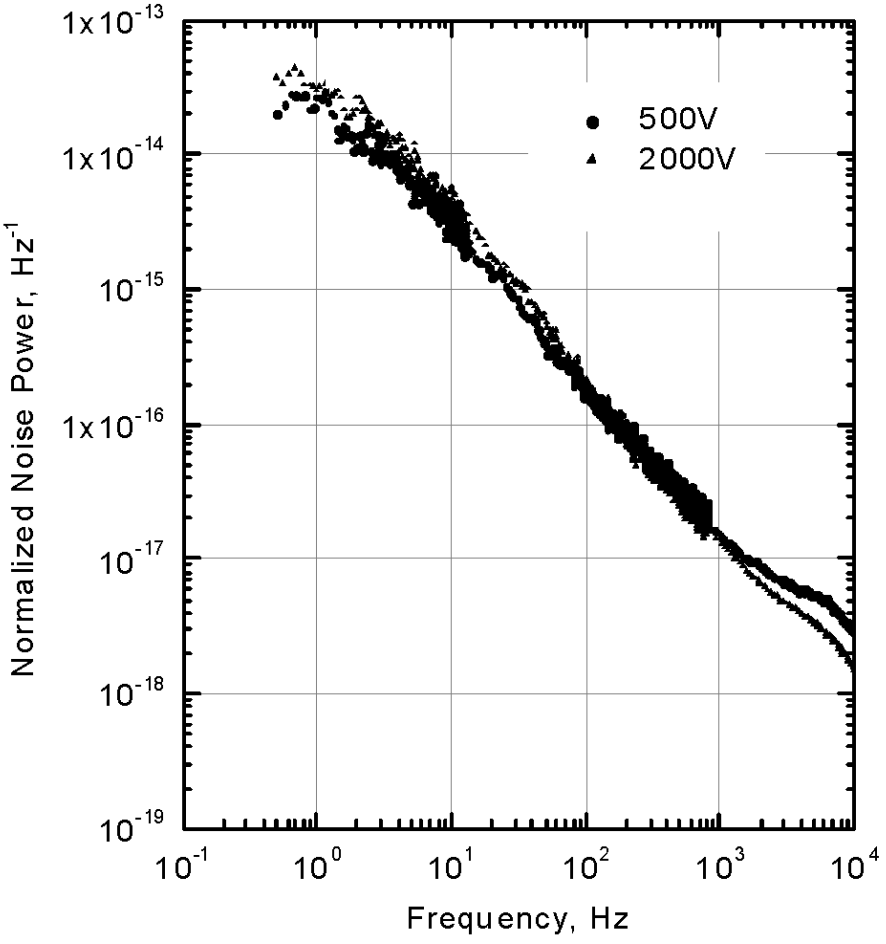

Figure 4.21: Normalized noise spectra showing the linearity of $1/f$ noise after normalization at 500 V and 200 V biasing.

to collect data and measure noise spectra.

Normalized noise spectra are the final output of the software that analyzes the data from the spectrum analyzer. The spectrum analyzer produces a single-sided spectrum of the fluctuating voltage at its input. The values produced are such that a sine wave input of a certain rms amplitude produces a peak in the spectrum of that amplitude. This value is not the power density but the power density can be obtained by dividing by the line width. Further to obtain the spectrum referenced to the sample, the gains of the pre-amplifiers must be taken into account as well as the response curves of the pre-amplifiers. Finally we generally want a two-sided spectrum so that data is divided by 2. The following equation is used to account for all these factors.

$$PSD(f) = \left(\frac{\frac{V(f)}{2}}{G_{IV} \times G_V \times H(f)} \right)^2 \times \frac{1}{\mathrm{LW}} \tag{4.14}$$

where, $PSD(f)$ and the $V(f)$ is the power spectral density and the voltage respectively at frequency f, G_{IV} and G_V are the gains of the current pre-amplifier and the voltage amplifier respectively. $H(f)$ is the frequency response correction and LW is the line width for that frequency span. After doing the necessary calculations the obtained data represents the noise spectrum produced by the sample.

4.6.5 Normalization

$1/f$ noise is generated when current flows through any resistive material. Figure 4.20 shows the generation of $1/f$ noise with the flow of current through the

resistor and how it scales with current. In order to understand the noise properly, it is necessary to present $1/f$ noise without the effect of bias current by dividing by the square of the bias, also known as dark current in a-Se samples [48]. The result is called the normalized spectrum. Figure 4.21 shows the results of the normalization on the spectrum of the test resistor. Notice that the two curves for different bias currents now fall mostly on top of one another.

4.7 Summary

This chapter started with a description of the metal evaporator, sputterer and the vacuum coater used for sample preparation and characterization. The technique of evaporation of metal and a-Se was described thoroughly. The experimental techniques for the fabrication included only the preparation of different metal/a-Se/metal samples. The methodology for measuring noise on metal/a-Se/metal samples was described in the following sections. A brief description of the X-ray unit was given, which was used to observe the change in noise behavior after X-ray exposures. The later part of this chapter described how the system was calibrated and tested with some known parameters. In order to put the upcoming data in the next chapter into perspective, the outcomes of the noise measurement system as well as the analysis of the data have been discussed in this chapter.

Chapter 5

Results and Discussion

This chapter is primarily divided into two sections. The first section deals with the noise properties of single-layer amorphous selenium films and shows how the noise behaves with different metal electrodes, alloying, and different surface conditions. The second section reports on the noise properties of multi-layer amorphous selenium films that are used in practical X-ray detectors and also reports on the presence of shot noise in these devices.

All the samples in this project were prepared by vacuum evaporation techniques as described in Section 4.2 and were relaxed for 72 hours in complete darkness at the room temperature of 22°C before they were electroded with different metals. All the samples were kept in complete darkness between the measurements to avoid a permanent change in their atomic structures from the influence of light. In terms of biasing, positive or negative has been defined in the way the voltage is applied to the top electrodes, i.e. if the top electrode is connected to the positive terminal of the supply then is referred as positive biasing.

5.1 Introduction

The measurement and analysis of noise in various amorphous semiconductors, in particular amorphous silicon has received attention from researchers [49, 50, 51, 52]. However noise measurements of amorphous selenium have not been investigated and reported to date. The main reason behind this lack of data might be because amorphous selenium is a highly resistive material and needs highly precise instruments to measure the noise. Because the dark current in the samples ranges mostly in nA, typically between 1 nA to 100 nA, the resulting noise current, which is typically around 1% of the dark current, ranges mostly in the pA range. To measure such a low-level signal the sample needs to be isolated properly from the ambient noise occurring from both the mechanical and the electrical systems around the area of measurement. As an example, mechanical vibration from the electrical motors in the surrounding areas (such as, the motors used for the ventilation system of the building) affect the noise measurements if not the experimental setup is mechanically isolated. Noise coming from the current pre-amplifier adds up another level of challenge in the noise measurement. The only way to eliminate this problem is to choose an appropriate type of amplifier that has a reasonably less noise than that is produced from the samples.

Another difficulty with selenium is the low glass-transition temperature. Due to this material property, the experimentally accessible temperature range is quite restricted. Most of the previous research shows that temperature is a critical parameter to vary when studying noise in a material [53]. It is almost impossible to

do experiments by changing the operating temperature of amorphous selenium devices. At a higher temperature, typically greater than 40°C, one cannot produce any useful noise data as the electronic structure of the a-Se layer gets affected by the glass transition temperature, while at the lower temperatures the conductivity of the a-Se layer becomes too low to produce an acceptable level of dark current to measure the noise. Typically the acceptable level of the dark current starts from the nano-amperes to above.

This research has resulted in the first reports of $1/f$ noise in amorphous selenium. The results of the present work primarily focus on the excess noise in the a-Se used in the Flat Panel Detectors.

Many researchers have published their results on the noise measurement in other types of materials used in the large area devices but no such research was done for amorphous selenium. Though the other areas of amorphous selenium such as charge transport, dark current etc. have been studied [54, 55, 56].

The previous chapter detailed the level of care taken to obtain sets of high quality data. Data from these noise measurements will be presented in this chapter. Many possible origins of $1/f$ fluctuations have been proposed by other researchers [57]. The applicability of some of them to a-Se will be discussed in the later part of this chapter in the light of the present research. Although, the physical mechanism responsible for the fluctuations in a-Se remains unknown.

5.2 DC Measurements

In order to understand the noise mechanism of the material used in a device it is necessary to measure some device characteristics. The most common device characteristics are the current-voltage (I-V) characteristics, current-time (I-t) characteristics and the conductivity activation energy of the material. Due to the nature of a-Se only the first two quantities were measured. Again because of the restricted temperature range, measurement of the activation energy was not attempted.

5.2.1 Current-time (I-t) Curve

The current-time relation is a complicated one for amorphous selenium devices (unlike other materials used for large area devices such as amorphous silicon). Figure 5.1 shows the current drift with time for various applied voltages in a log-log plot. Both the top and the bottom electrodes are gold and the device is made with a transverse type structure. Each voltage was applied for 3 hours with 6 hours of waiting time with no voltage in between the two consecutive applied biases. This plot shows that the dark current decayed by almost a decade after applying a constant voltage over an hour and had not reached a steady value. Typically most of the decay occurs over the first 1000 sec. After 5 hours (not shown in the graph) the rate of decay becomes much smaller. Noise measurements are problematic while the current is changing, so typically the sample is under bias for 5 hours before the noise measurements are attempted. For some samples, the current initially increases for a few minutes before the decay begins. The ratio of initial to final current depends on

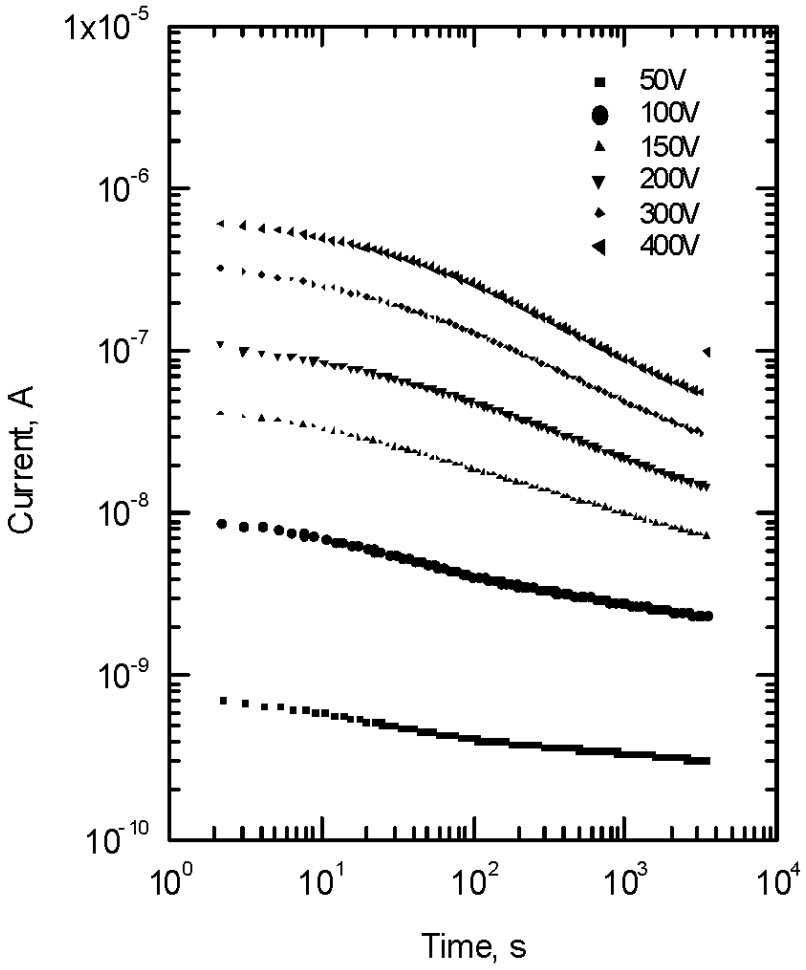

Figure 5.1: Current drift after applying various bias voltages to a-Se photodetector sample with Au top and bottom electrodes. Material composition of this sample is a-Se with 0.5% As and 10ppm Cl and the sample thickness is 30 μm. Top electrode is biased with positive voltages. At a low applied electric field the decay of current is much lower than that of at high applied electric field.

the applied electric field. The ratio is lower for a comparatively low electric fields. Typically if the electric field is less than 3 V/μm then it is assumed to be low electric field, whereas if the applied electric field is equal to 7 V/μm or over then it is taken as a high electric filed. Applied electric field in the range between 3 to 7 V/μm is expressed as moderate level of electric field. The curves vary depending on the metal used as electrodes and on sample preparation conditions but are reproducible for a given sample [3].

The magnitude of the measured noise signal varies with the bias current [58], therefore, ideally the bias current should be held constant during time required to acquire an averaged noise spectrum. In order to satisfy this condition of acquisition several hours of delay was provided so that the current stabilizes sufficiently and the difference in magnitude between the starting and the ending times remains less than 5% of the total dark current.

It should be mentioned at this point that the high voltages involved in these and the noise measurements sometimes resulted in damage to the sample. The top electrode was particularly vulnerable especially if the electrode was gold. Either due to a corona type discharge or some other effect the electrode could violently and suddenly vaporize damaging the selenium at the same time. Naturally such an event terminated any measurement and destroyed the sample.

5.2.2 Current-voltage (I-V) Curve

Figure 5.2 shows the current-voltage (I-V) characteristic curves obtained from the data of Figure 5.1. These curves are generated by cutting the time curves of

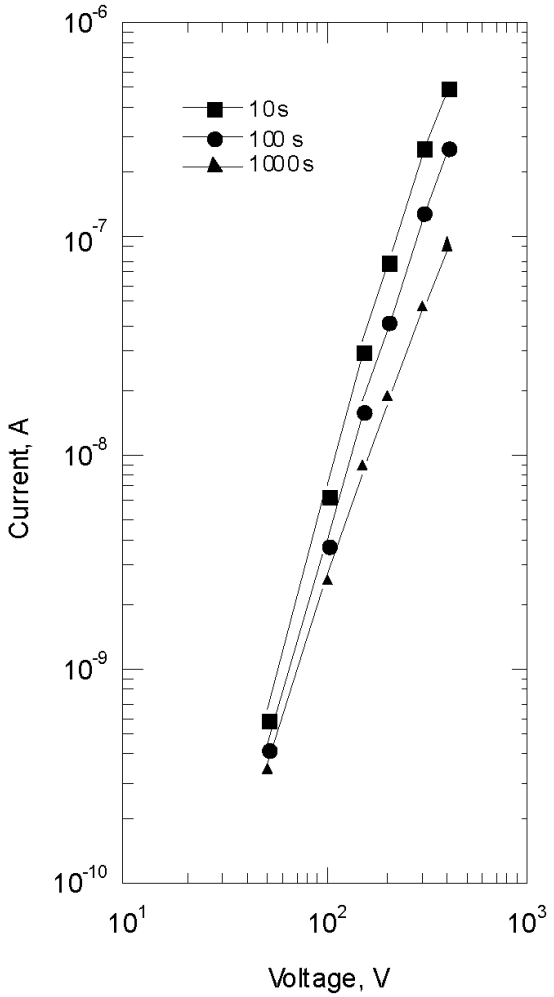

Figure 5.2: I-V relation for a-Se. Data was obtained by taking the time slice from Figure 5.1, at 10 s, 100 s and 1000 s.

Figure 5.1 at specific times. All three curves show that the I-V relation is highly non-ohmic. In the Figure 5.2 current is plotted as a function of voltage in a log-log plot. In a log-log plot ohmic behavior would be a line of slope 1; the I-V relation for a-Se has a slope close to 2.8, so $I \propto V^{2.8}$. This non-ohmicity makes the a-Se devices different than other amorphous materials, such as amorphous silicon. The non-linearity behavior most likely originates at the metal-semiconductor interface due to the high level of injection at higher applied voltages and the trap centers reduce the carriers drift at the lower voltages. The non-ohmicity creates difficulties for the noise measurements.

There is a strong possibility that the metal-semiconductor interface effects are the dominant sources of the fluctuations. Non-ohmicity hints that the metal-semiconductor interface "controls" the device current. This also indicates that the overall conductance fluctuations of the device are related to the applied voltage, hence depend on the applied electric field. Because of the high injection of carriers at a larger applied voltage it can be assumed that the noise from the interface at high voltages would then dominate. It could be that the measured noise at a higher field is not that of originated from the bulk of the a-Se. Since we are mainly interested in characterizing the noise for use in X-ray detector modeling, the origin of the noise is of secondary importance.

5.2.3 Basic Characteristics of the $1/f$ Noise Spectra of a-Se

The fundamental measurements performed in the present work are the frequency dependence of the noise power density. Most of the presented graphs have been

normalized by the square of the respective dark currents to eliminate the effect of dark current. The detailed method of acquiring such spectra has been described in the previous chapter. Although the present work emphasizes the normalized noise spectra, for some analysis the un-normalized noise spectra are more appropriate and these will be shown when required. Of course, the normalization does not affect the slope or shape of the noise curves.

We have reported [59, 60, 61] that the low frequency conductance noise produced in the layers of amorphous selenium under conditions similar to those found in the detectors follows a $1/f^{\alpha}$ power law with the value of α ranging in between 0.77 and 1.5. This range of values is comparable to those reported in previous studies in a wide range of materials and devices in which $1/f$ fluctuations have been observed, the slope ranged from 0.7 to 1.5. A study by Malik, Ray and Bruce on Langmuir-Blodgett films on silicon reported finding $\alpha = 1.18$ [62]. Research by Johanson and Kasap reports on $1/f$ noise of amorphous indium oxide showing the slope ranging between 1.0 and 1.12 [63]. In recent years, a number of researchers have reported the presence of $1/f$ noise in hydrogenated amorphous, micro and nano-crystalline silicon devices. In the year 1987, Bathei and Anderson reported the slope of $1/f$ noise ranging in between 0.7 to 1.3 [64, 65] for hydrogenated amorphous silicon devices. Later Kasap *et al.* reported that hydrogenated amorphous silicon germanium (a-SiGe:H) films exhibit $1/f$ noise with a slope α ranging from 1.2 to 1.5 [66].

Figure 5.3 shows a single noise power spectral density (PSD) curve of a stabilized amorphous selenium sample of 60 μm thick. Both electrodes are made with sputtered gold. The spectra fits with a $1/f^{\alpha}$ power law; 2000 individual spectra

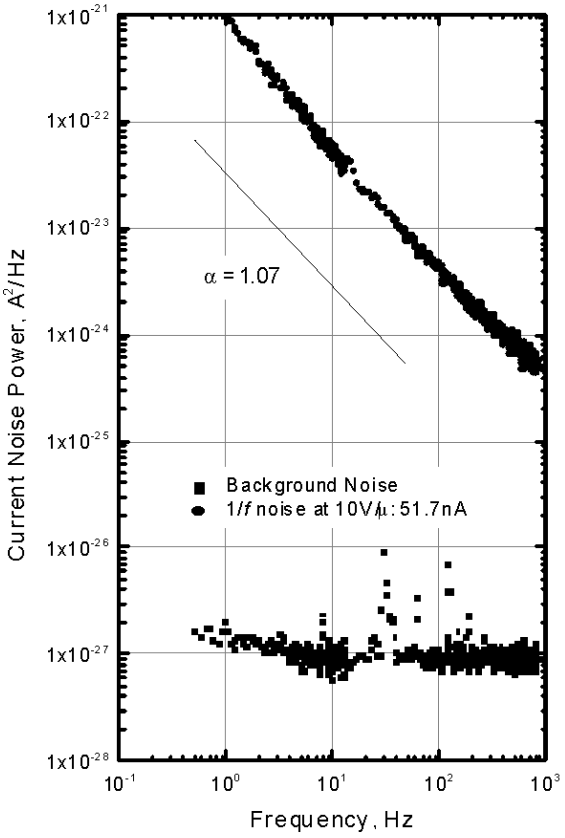

Figure 5.3: Current noise power spectra at room temperature showing $1/f$ noise of a measured slope $\alpha = 1.07$ with 10 V/μm electric field. Measured dark current is 51.7 nA. Both the top and bottom electrodes are sputtered gold. A positive dc voltage was applied at the top electrode.

were averaged to obtain the 1 Hz to 13 Hz part of the spectra while 5000 individual spectra were averaged to acquire the rest of the curve. The slope α was measured with a least-squares linear regression method and is 1.07 at an applied electric field of 10 V/μm that produced a bias current of 51.7 nA. All the data are measured at room temperature (22°C). The background noise shows some signs of unwanted signals from the 60 Hz power frequency and its harmonics. This background noise was subtracted to obtain the $1/f$ noise spectra, although the background noise in this case is well below the $1/f$ noise. However, for other samples and conditions, the background noise becomes comparable in magnitude to the $1/f$ noise The technique for acquiring the background noise has been described in section 4.6.1.2.

In order to show the background noise power level with respect to the noise power level of $1/f$ noise, the graph in Figure 5.3 is plotted without any normalization. The background noise power can be presented in a normalized noise power spectra by drawing a straight line at the appropriate level, but representing with the actual data provides a better illustration. To normalize the spectra in Figure 5.3 a normalization factor 3.7×10^{14} can be used, and after normalization the normalized noise at 1 Hz would be 3.7×10^{-7} /Hz. The rms amplitude of the conductance fluctuation was measured over the 1 Hz to 1000 Hz frequency range, which is approximately equivalent to one part in 1000 of the bias current, that is approximately 50 pA.

5.3 Non-Linearity of Noise Spectra in a-Se samples

Ideally, materials with simple conductance noise exhibit a linear relationship between the bias current and the current noise amplitude [67]. The basic model that relates the noise power spectral density with dark current is expressed by the following equation [68],

$$S_n(f) = K\frac{I^b}{f^\alpha} \tag{5.1}$$

where, $S_n(f)$ is the noise power spectral density, I is the bias current, K is a constant that determines the magnitude, b is the slope of the (log) noise power with respect to the (log) bias current and α gives the slope of the $1/f$ noise. Since the equation is given in terms of noise power, a "linear" relationship with current results in $b = 2$.

Figure 5.4 shows the noise power as a function of dark current for four different frequencies 10 Hz, 100 Hz, 1 kHz and 10 kHz for the sample where a 20μm thick a-Se layer was electroded with two different metals. Top electrode was fabricated with gold and the bottom electrode was made with aluminum. The slope of each curve, ranging from 1.56 to 1.79 indicates that the noise is showing sub-linear behavior with dark current. A similar study on hydrogenated amorphous silicon was reported by Parman and Kakalios [69] in 1991 showing that amorphous silicon shows a sub-linear behavior with $b = 1$ at 370K increasing to a maximum of $b = 1.9$ at 420K [70].

Due to the non-linear behavior, it is obvious that normalization with respect to the bias current will not scale the spectra for different bias currents onto a common

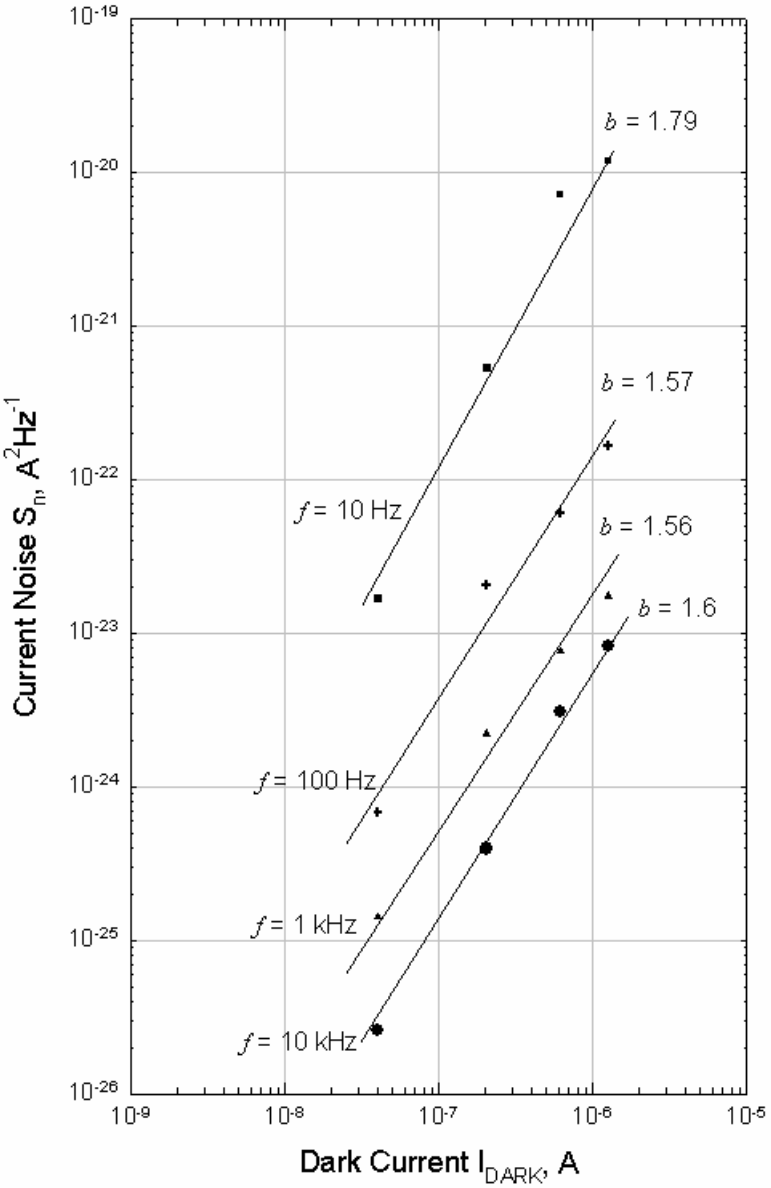

Figure 5.4: Noise power as a function of dark current. The sample is 20 μm thick with gold top electrode and aluminum bottom electrode. Slope of each set has been indicated as b.

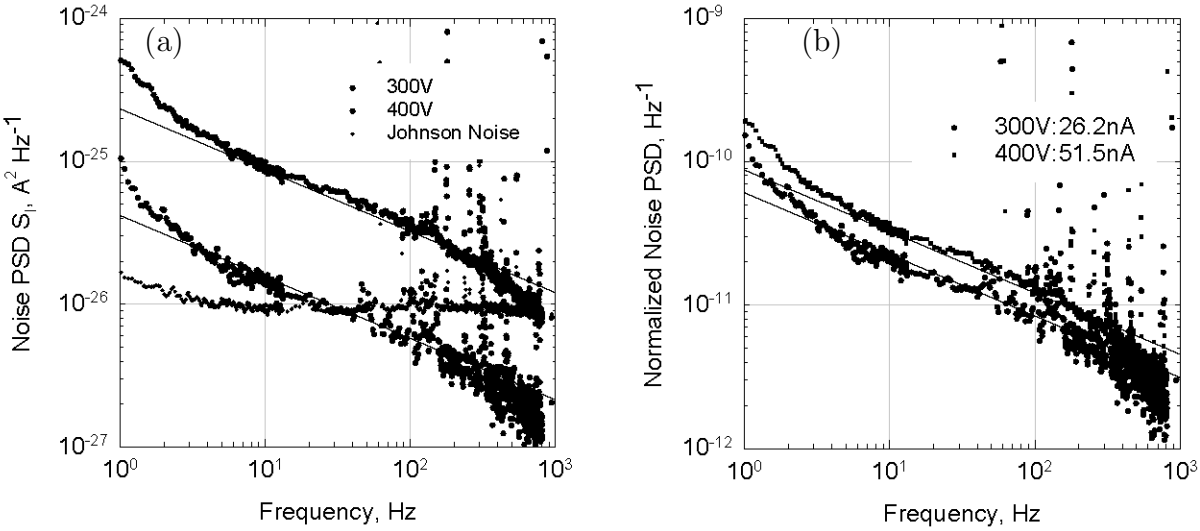

Figure 5.5: Noise power density spectra for a-Se sample with two different bias voltage. (a) Un normalized spectra showing Johnson noise, and (b) Normalized spectra. The sample is 60 μm thick with platinum top and bottom electrode.

curve. Further, the non-linearity causes some difficulty in explaining the observed current fluctuations in terms of fluctuations originating in the sample. There are two ways in which non-linearity might arise. The first is that the bias current is directly affecting the noise generating mechanism in the material. In this case, since $b < 2$ the higher currents act to suppress the noise. Alternatively, given that the sample is highly non-ohmic, it is possible that as the current varies different parts of the circuit that represents the sample, i.e. the metal-semiconductor interface or the bulk selenium, might contribute to the noise differently at different applied voltages. Unfortunately, it is very difficult to investigate the mechanism for non-linearity through noise measurements.

Figure 5.5 shows the non-linearity of the noise spectra for a different a-Se sample.

The sample is a 60 μm thick a-Se layer with platinum top and bottom electrodes. The un-normalized noise spectra shown in Figure 5.5(a) are separated by almost an order of magnitude, but it is not obvious from the Figure that the noise is non-linear. After being normalized, the spectra are still separated by a factor of two, depicted in Figure 5.5(b); by graphing the normalized spectra the non-linearity is immediately apparent.

5.4 Various Factors Affecting Excess Noise

In order to thoroughly investigate the $1/f$ noise of amorphous selenium, various material parameter have been systematically altered. These parameters include the type of metal used for the electrodes, the thickness of the selenium layer, area of the electrodes, the substrate temperature during evaporation, the composition of the amorphous selenium alloy and the condition of the surface. Because of the absence of any theoretical model of noise in amorphous selenium, it is important to investigate the effect of as many material parameters as possible. Each parameter will be discussed in a section of this chapter.

5.4.1 Effect of Metal Contacts

Noise spectra were obtained for a-Se with different types of metal contacts, particularly platinum, gold, chromium and aluminum. All these metals are used in actual devices. Especially, platinum is used for its low "dark" current and gold is used because it is inert to the environmental parameters, such as water vapor and

air. Metals that electro-migrate into selenium [71] are obviously unsuitable to use as electrodes on the selenium layers. These include silver and copper. Johanson *et al.* has studied the dark current of a variety of metal electrodes on amorphous selenium and came to the conclusion that there is no simple correlation of the current level with the work function, the injection of holes at the metal/selenium interface or the transport through the bulk material [72].

An example of the dependence of the dark current with the applied electric field for various metal electrodes is shown in Figure 5.6, where dark current is plotted as a function of applied electric field. The samples are 35 μm thick stabilized a-Se and the area of the top electrode is 0.25 cm^2. All the samples were prepared in the same deposition environment in order to keep the atomic structure of the material as constant as possible. The solid dots are for symmetric samples that is the same metal for both top and bottom electrodes while the hollow dots are for asymmetric samples. The magnitude of dark current depends not just on the bottom or on the top electrode but on both of them. Changing the metal of either electrode affects the magnitude of the dark current and the slope of the I-E relation.

The noise spectrum also depends on the metal of the electrode as shown in Figure 5.7 where normalized noise spectrum have been plotted for a sample of 100 μm thick stabilized a-Se. The bottom electrode is aluminum and is kept grounded. Three separated top electrodes were formed using evaporated aluminum, and sputtered platinum and gold. An optimum deposition environment was maintained during the selenium evaporation, similar to that used to fabricate commercial devices. The measurements were taken for a moderate electric field (4 V/μm). It is quite evident

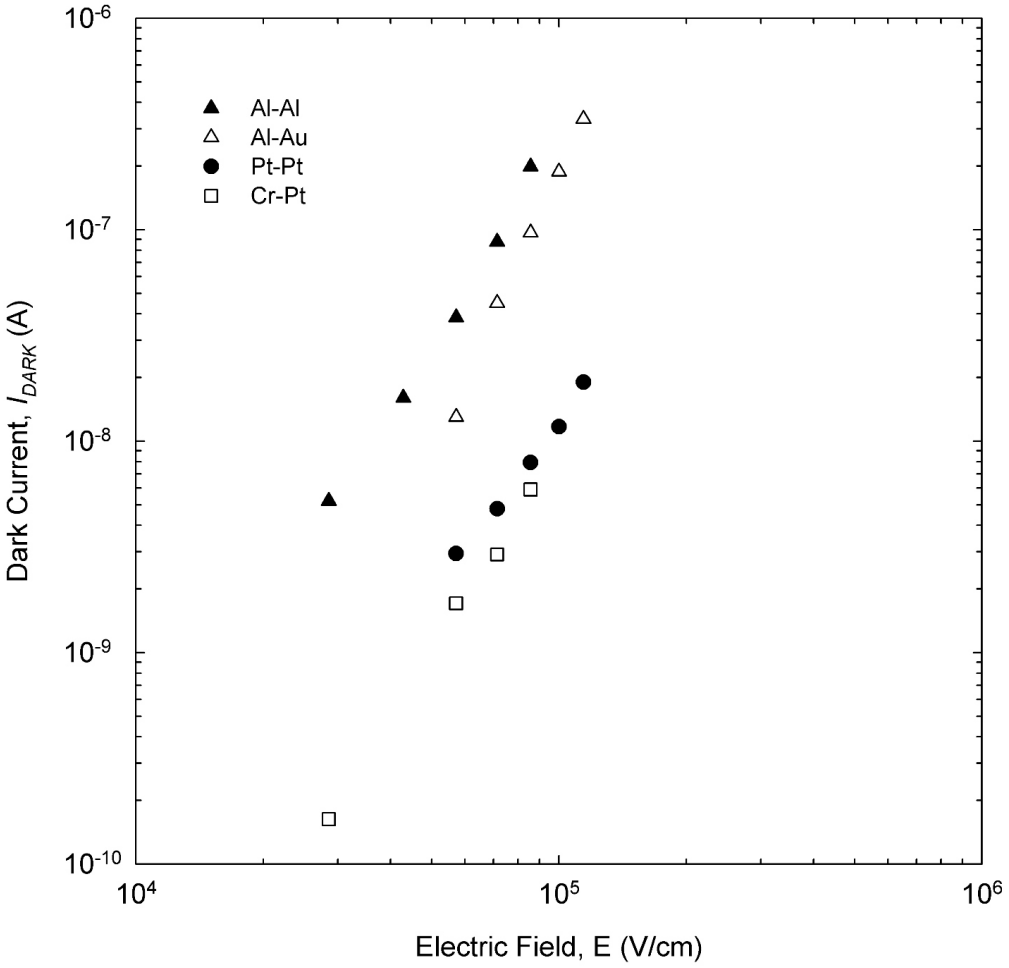

Figure 5.6: The dark current vs. electric field for four different types of metal combinations for top and bottom electrodes. Name of the metal stated in the left hand side is the top electrode. In all four cases a positive dc bias is applied at the top electrode.

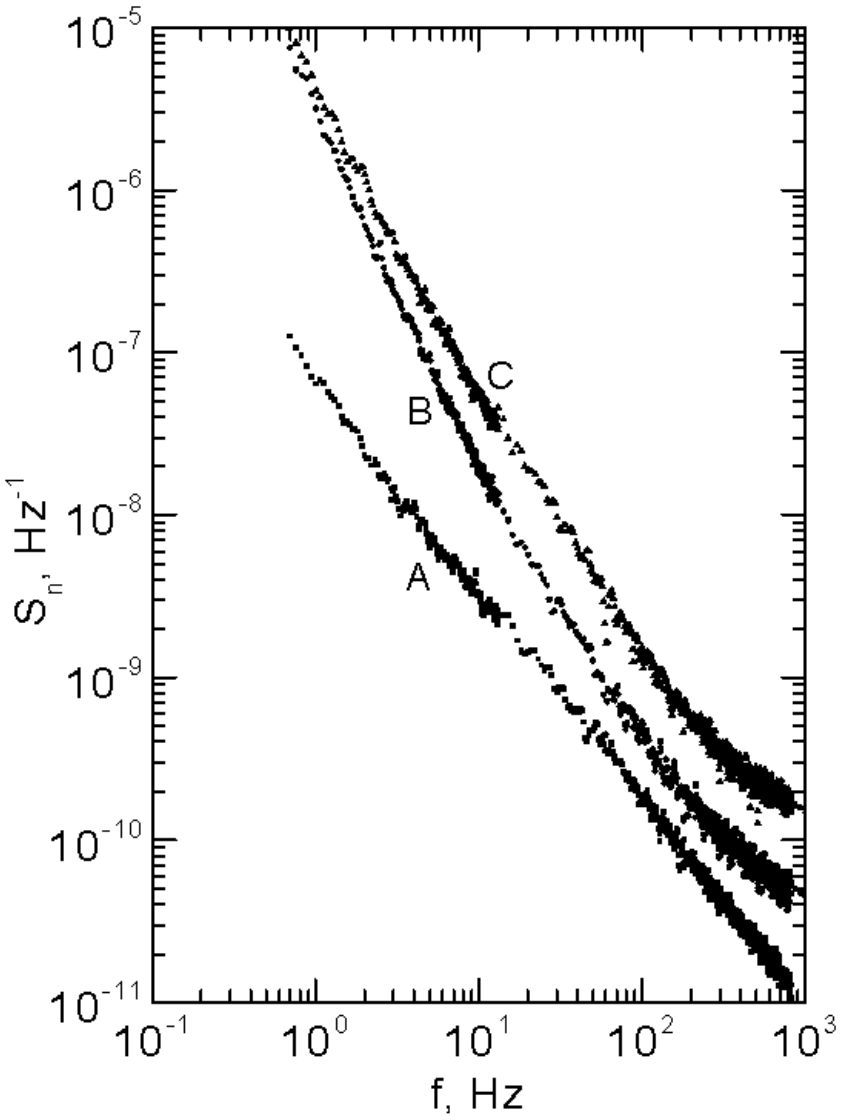

Figure 5.7: Normalized noise power spectrum with different metal contacts. (A) Top electrode is Al, (B) Top electrode is Au and (C) Top electrode is Pt. All three bottom electrodes are Al. The samples are 100 μm thick. A constant applied field of 4 V/μm was applied for all the measurements. Changes in noise magnitude and the slope are observed with different metals.

Table 5.1: Dark current at different combinations of top and bottom electrodes showing the consistency of the change in dark current with the metal used for electrodes. In all the measurements, top electrodes of the samples were connected to the positive terminal of the dc supply.

Run	Top electrode	Bottom electrode	Dark current (nA)
146	Al	Al	199
146	Pt	Pt	7.9
268	Cr	Pt	2.88
268	Pt	Pt	10.65
268	Al	Al	812
268-2	Au		97
268	Pt		47
268	Al	Au	47.6
268-2	Au		45
268-2	Pt		40.5

from the figure that both the overall noise level and the slope of each noise spectra depends on the metal used as the top electrode. There is a trend of the noise magnitude and slope with the work function of the metal (Φ_m). Work functions of aluminum, gold and platinum are 4.28 eV, 5.1 eV and 5.65 eV respectively which is much lower than that of selenium, which is 5.9 [73]. Both the magnitude and the slope of the $1/f$ noise increase with the work function of the top electrode metal.

More combinations of metals for the top and bottom electrodes were investigated. Shown in Table 5.1 are the metals used and the dark current variations. Unlike in the previous figure, the samples were prepared in different deposition runs the deposition number is shown in the table. Since these samples were part of other studies, some deposition parameters were changed from run to run so there is possibility that the variations in noise are not solely due to the metal used. However, there is always a consistent decreasing trend going from platinum to gold to aluminum in the noise magnitude. Notice that both electrodes influence the dark current and the noise.

For example, the three samples with platinum top electrodes but different bottom electrodes do have different dark currents and noise.

The study by R. E. Johanson, *et al.* [72] shows that the current density from the metal-selenium junction does not directly depend on the work function of the metal. Although a Schottky barrier might form, the applied voltages greatly exceed the height of the barrier and thus should not influence the dark current. However, it is less clear that such a barrier would not affect the noise, but no model of noise at a Schottky barrier has been applied to a-Se. Various other factors might include the formation of metal-selenides at the metal-selenium junction since it has been an established fact that a few metals do diffuse into selenium at high electric fields [74, 75] and form such selenides. Research by Hoffman and F. Rose in 1953 showed that in crystalline selenium (c-Se) rectifiers instead of a Shottky barrier in the Cd-c-Se, interface the diode is formed at the junction of n-type cadmium selenide and the c-Se. A further thorough research on the dark current in the metal-selenium interface is required to have a clear picture of noise behavior at the metal interface.

5.4.2 Effect of the Bulk Material

In the previous section a clear trend of the dependence of $1/f$ noise on the metal electrodes was found. In order to establish a definite relationship of $1/f$ noise, a further examination of noise with the other parameters is needed. In this section the effect of $1/f$ noise is observed by changing the bulk parameters of the samples. To investigate the dependence of the noise on the bulk a-Se, various parameters are varied,

1. The thickness of the bulk and effective device volume

2. The substrate temperature

3. Arsenic content in the bulk material

4. Chlorine content in the bulk material

Among the quantities mentioned above, the thickness of the bulk material and the substrate temperature during amorphous selenium deposition was controlled in the present research facility. But the variation of arsenic and chlorine content was done by using different types of starting alloys supplied by "Noranda Advanced Materials" in the form of pellets, who checked the composition using mass spectrometry. Accuracy of the data falls within $\pm 0.05\%$ for the arsenic concentration and about a factor of 2 for chlorine. The material composition of the prepared sample used for this project was not measured after deposition, which leaves a possibility that some fractionation occurred during evaporation. However, a negligible a change from the starting alloys is observed with mass spectroscopy from the samples prepared elsewhere using a similar process.

5.4.3 Thickness of the a-Se layer and effective device volume

The dependence of $1/f$ noise on the volume of the device can be derived from the following empirical formula by Hooge (1969) that relates the normalized noise to the number of carriers in the device [17, 18]. In the case where the current power spectral density of $1/f$ noise follows a power law with a slope close to unity and is

proportional to the square of dark current one can represent the spectral density in the form,

$$\frac{S_I}{I^2} = \frac{C}{f} \tag{5.2}$$

where S_I is the spectral current noise density, I is the dark current flowing through a sample of volume V with n number of free carrier concentration in the dark. C is a dimensionless coefficient. In his derivation Hooge correlated a large number of experimental data obtained by different authors [76] with an approximation of $C = \alpha_H/nV$ where he assumed that $\alpha_H = 2 \times 10^{-3}$ is a universal coefficient. With this substitution the volume dependence of noise spectra can be derived as

$$\frac{S_I}{I^2} = \frac{\alpha_H}{nf} \times \frac{1}{V} \tag{5.3}$$

Equation 5.3 shows that the magnitude of noise power is inversely proportional to volume. The device volume can be altered in two ways. Either by increasing or decreasing the thickness or by increasing or decreasing the contact area. By depositing the contact area one is actually inserting a nominal change in the surface condition of the a-Se layer underneath the metal electrode. It is assumed that the change in the atomic structure in the bulk around the electrode area is negligible as the bulk thickness is quite large with respect to the "disturbed" thickness. The volume effect is examined using six samples in two sets. Each set consists of identical top and bottom electrodes but with three different thicknesses of the bulk material of the same alloy composition.

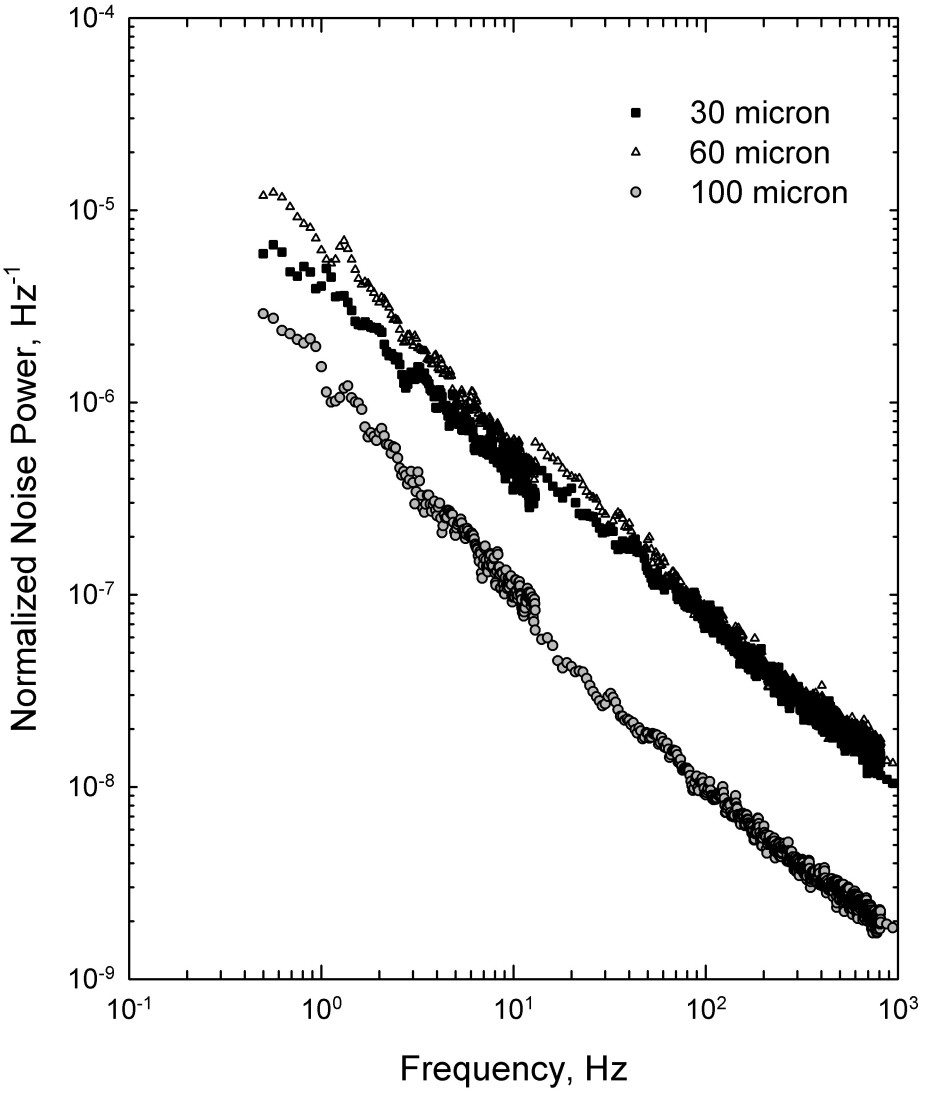

Figure 5.8: Normalized noise spectra showing dependence on thickness with platinum electrodes. Samples were deposited in three separate depositions. All other deposition parameters except the deposition thickness was kept constant. Both top and bottom electrodes of each sample are platinum. Top electrode was biased with a positive voltage.

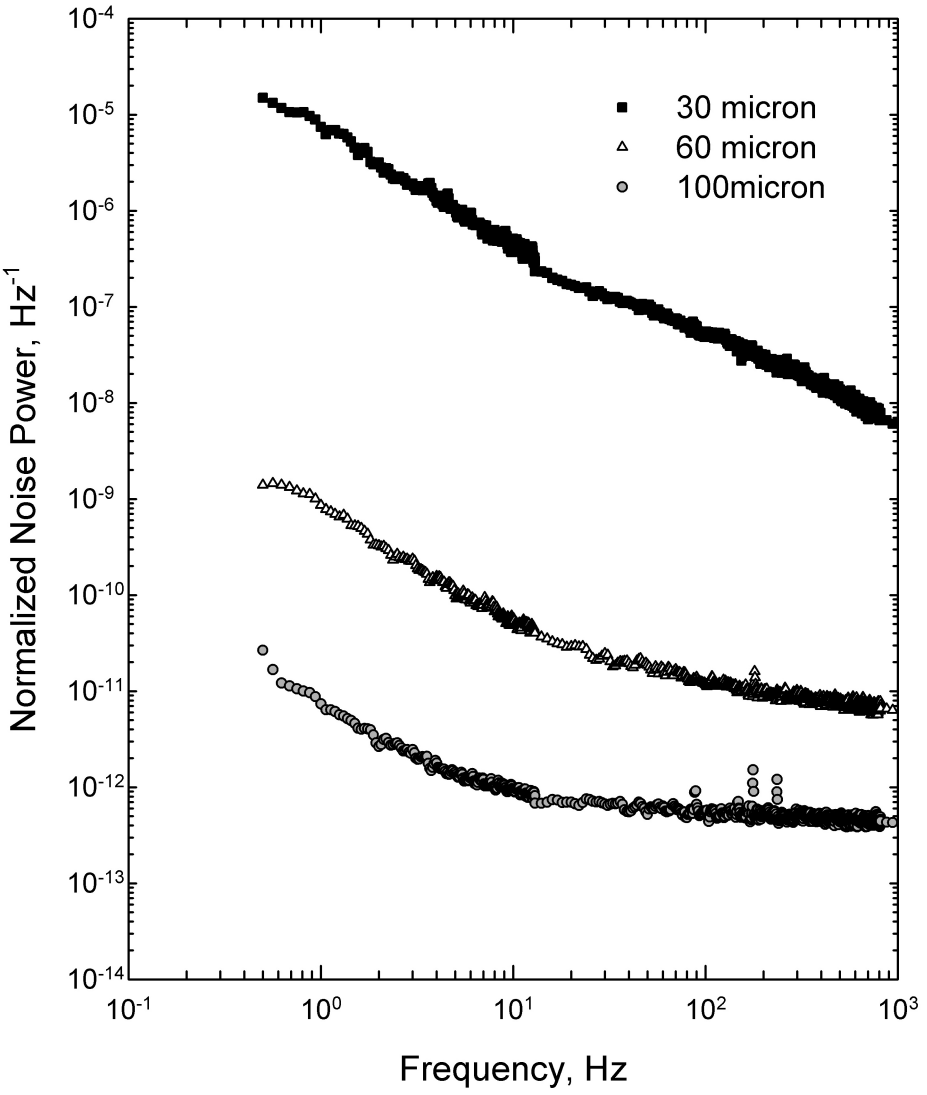

Figure 5.9: Normalized noise spectra showing dependence on thickness with gold electrodes. Samples were deposited in three separate depositions. All other deposition parameters except the deposition thickness was kept constant. Both top and bottom electrodes of each sample are gold. Top electrode was biased with a positive voltage.

Figure 5.8 and Figure 5.9 shows the dependence of $1/f$ noise on the thickness of the samples. Both the graphs have been plotted for three different thicknesses of a-Se layer, 30, 60 and 100 μm keeping the alloy composition of the bulk material constant with 0.3% As and 10 ppm chlorine. Samples for Figure 5.8 have platinum electrodes and those for Figure 5.9 have gold electrodes. All the samples have been prepared with the same substrate temperature of 50°C. All the samples have 25 mm^2 top electrodes; therefore the effective device volume of a 100 μm thick sample is 2.5 mm^3. The effective device volume of the 60 μm and the 30 μm thick samples are 1.5 mm^3 and 0.75 mm^3 respectively.

The measurements show a decrease in magnitude of normalized spectra with increase in the bulk volume, when the surface condition and the area of the metal contact remained the same. Both the figures show a dependence of $1/f$ noise on the thickness of the bulk material. In both cases, the magnitude of $1/f$ noise decreases with the volume of the device but in neither case was the proportionality factor 1/V. In Figure 5.8 there was a negligible change in the magnitude of $1/f$ noise when the thickness increased from 30 μm to 60 μm, despite the increase in device volume by a factor of two. A significant amount of change in the magnitude of $1/f$ noise is measured when the volume was increased almost 67% by changing the thickness from 60 μm to 100 μm. The measured change in magnitude is 6 times. This indicates that the level of fluctuations inside the material increased significantly with the increase of the bulk thickness.

In the second series where the same experiment was done on the samples with gold electrodes the results were even more surprising. Figure 5.9 shows the results

from the samples with gold electrodes. In this case, the magnitude of the $1/f$ noise varied by orders of magnitude. Moving from 30 μm to 60 μm thickness the magnitude of $1/f$ noise dropped almost 4 decades while for the change from 60 μm to 100 μm, the magnitude of $1/f$ noise dropped almost around 2 decades. As mentioned earlier in a previous section that electro-migration of gold in the selenium is observed by a few researchers. The electro-migration of gold might have affected the noise level, and as a result the drop in noise magnitude did not follow the non-linearity behavior found in the I-V characteristics.

None of the measurements showed the inverse-proportionality of $1/f$ noise with the change in volume. The main reason for this phenomenon is likely that the noise is controlled by the interface, rather than the bulk. As a result, Hooge's parameter $\alpha_H = 2 \times 10^{-3}$ is not applicable.

Device volume can also be varied with the size of the top electrode. To examine how the area of top electrode affects the $1/f$ noise, two platinum top electrodes of different sizes were deposited on top of the same sample. Due to electro-migration in selenium, gold electrodes were not used in this experiment. Figure 5.10 shows the normalized noise power spectral density of two different sized platinum top electrodes with areas of 10 mm^2 and 25 mm^2 producing device volumes of 0.6 mm^3 and 1.5 mm^3 respectively. The Alloy composition of the bulk material is amorphous selenium with 0.5% arsenic and 40 ppm chlorine. Substrate temperature was kept at 60°C during the deposition. Both the normalized curves show that the area of the top electrode does not effect on the slope and the magnitude of the normalized $1/f$ noise. This result is even more surprising than the previous case. Regardless of whether the

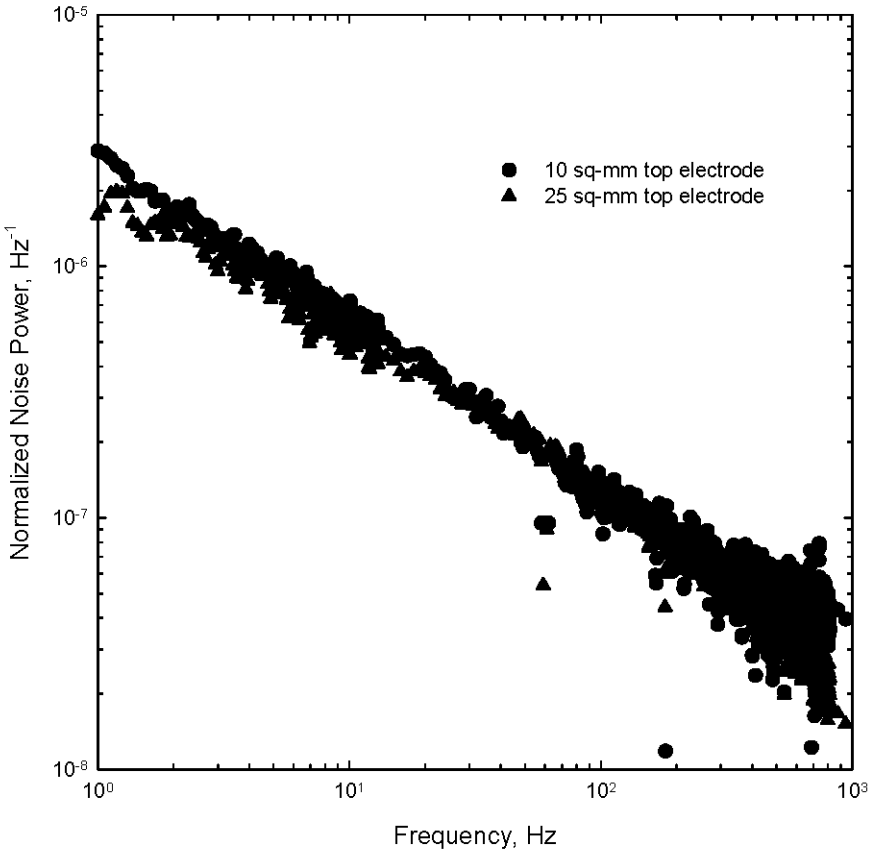

Figure 5.10: Normalized noise power spectral density with platinum electrodes of different size. The sample is 60 μm thick. Both top and bottom electrodes are platinum. Alloy composition of the bulk material is 0.5% As and 40 ppm Cl.

noise generation is in the bulk or at the interface, the expectation was that the noise power should scale with area since the noise sources should be uncorrelated across the surface of the electrodes. The bias current, however, should also scale with area, and the normalized noise should scale as $S_I/I^2 \propto \frac{1}{A}$. The normalized noise being independent of area could arise if the current is controlled by a hot-spot which is smaller than the area of the electrode.

5.4.4 Substrate temperature

Some research has shown that dielectric relaxation occurs in amorphous selenium films. Fiedler *et al.* has reported that the activation energy of the relaxation decreases with an increase of the substrate temperature. They have found that the activation energy reaches a minimum for substrate temperatures between 47°C to 52°C [77]. Depositing on a colder substrate produces a great number of dangling bonds due to the rapid quenching of the selenium, which creates trap centers at shallow and deep levels. Additional traps can increase the amount of conductance fluctuations.

Figure 5.11 shows the power spectra of two different samples deposited at two different substrate temperatures. Both the samples have a selenium layer stabilized with 0.5% arsenic and 40 ppm chlorine. The thickness of the a-Se layer is 60 μm. For both samples, the top and bottom electrodes are gold. The substrate temperature during deposition of sample A was 50°C and that of B was 70°C, and maintained constant during deposition. In order to keep the other parameters constant for both the depositions, a same set of evaporation procedure was maintained. The error in

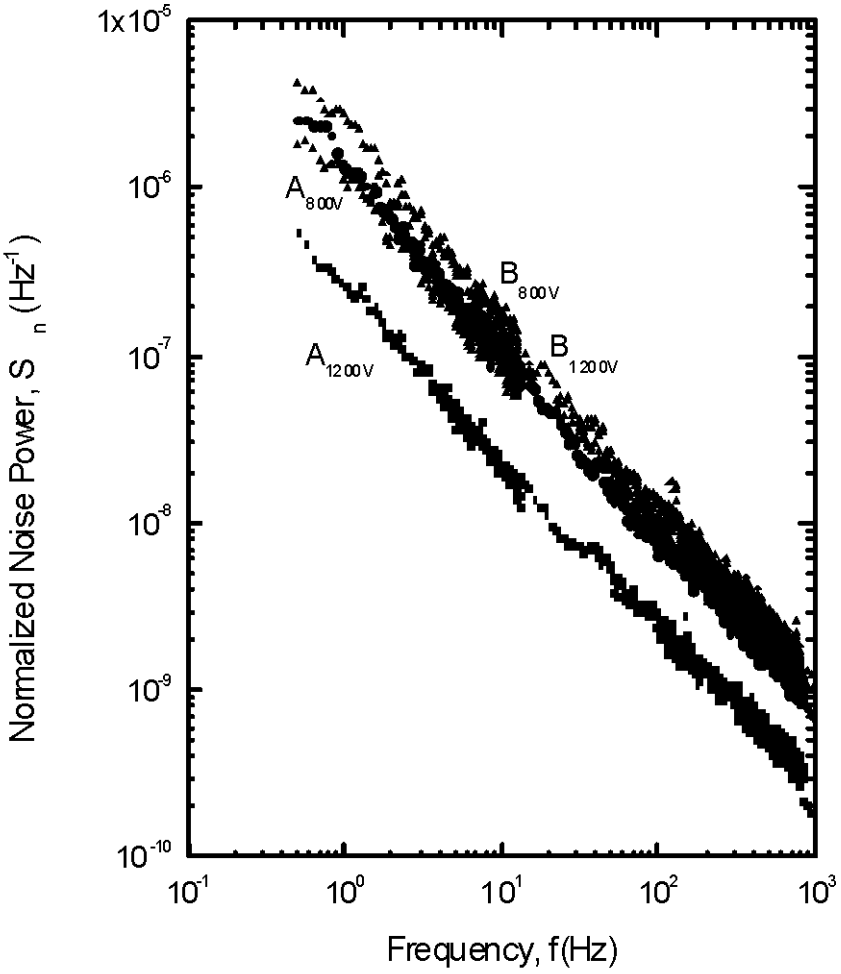

Figure 5.11: Normalized noise spectra at 800 V and 1200 V biasing on two different amorphous selenium samples deposited at 50°C (Sample A) and 70°C (Sample B). Both the samples are 60 μm thick with gold top and bottom electrodes.

the measurements depends on the amount of averaging and is self evident from the amount of scatter in the graph. All four power spectra exhibit $1/f^{\alpha}$ power law with a slope $\alpha = 1.19$.

The measurement shows that, for sample A, the normalized noise power magnitude became 5 times lower when the biasing voltage was increased from 800 V to 1200 V. The same measurement for sample B does not show any significant difference in the normalized noise power magnitude. Montrimas and Petretis have shown in their paper that the number of defects in the selenium at low substrate temperature is much larger than higher substrate temperatures [78]. We found that the sample with 70°C substrate temperature did not show a significant difference in the magnitude of $1/f$ noise at different dc biasing voltages, as the generation of trapping centers at this substrate temperature is less than that of the sample prepared at 50°C substrate temperature. Hence, the generation of trap centers during deposition might have an effect on the $1/f$ noise at a comparatively low applied electric field.

5.4.5 Material composition

Pure amorphous selenium is unstable and will crystallize over time at room temperature. Other environmental factors such as light, humidity and oil from human fingertips will accelerate the crystallization. To make the selenium more stable and to increase the glass transition temperature, a small amount of arsenic (typically 0.2% to 0.5% by wt.) is mixed with the amorphous selenium. But the addition of arsenic creates dangling bonds in the structure which produce carrier trap centers in the mobility gap region that reduce carrier mobility. To offset the effect of arsenic, a

Table 5.2: Relationship of arsenic and chlorine concentration with carrier mobility

As (% wt.)	Cl (ppm)	μ_h (cm^2/Vs)	τ_h (μs)	$\mu_h\tau_h$ (cm^2/V)
0.3	10	0.14	107	1.5×10^{-5}
0.5	10	0.12	85	1.0×10^{-5}
0.5	20	0.14	107	1.5×10^{-5}
0.5	40	0.11	78	8.6×10^{-6}

few ppm chlorine is added. The effect of adding arsenic and chlorine on the transport properties is shown in table 5.2. The effect on $1/f$ noise is described below.

Figure 5.12 shows normalized noise spectra of two different amorphous selenium samples with different arsenic concentrations. The concentration of the other stabilizing material chlorine was kept constant at 10 ppm for both the samples. All other deposition parameters such as the substrate temperature, deposition rate, vacuum level and deposition of the electrodes were kept constant to ensure, as well as possible, that other factors don't affect the conductance noise.

The result apparently show that arsenic concentration has an effect on $1/f$ noise. The additional 0.2% arsenic decreased the $1/f$ noise magnitude by more than a decade despite the assumption that adding arsenic increases the trap density. However, the sample with 0.3% arsenic produced 5.4 nA dark current while the one with 0.5% arsenic produced 63 nA with the same 400 V biasing.

Figure 5.13 shows the normalized noise power spectra of two different samples with different chlorine concentrations. For both samples, the concentration of arsenic was kept constant at 0.5%, so the number of dangling bonds produced by the arsenic should be similar. For the same applied electric field the sample with 5 ppm chlorine produced 40 nA dark current while the one with 20 ppm chlorine produced 2.33 nA.

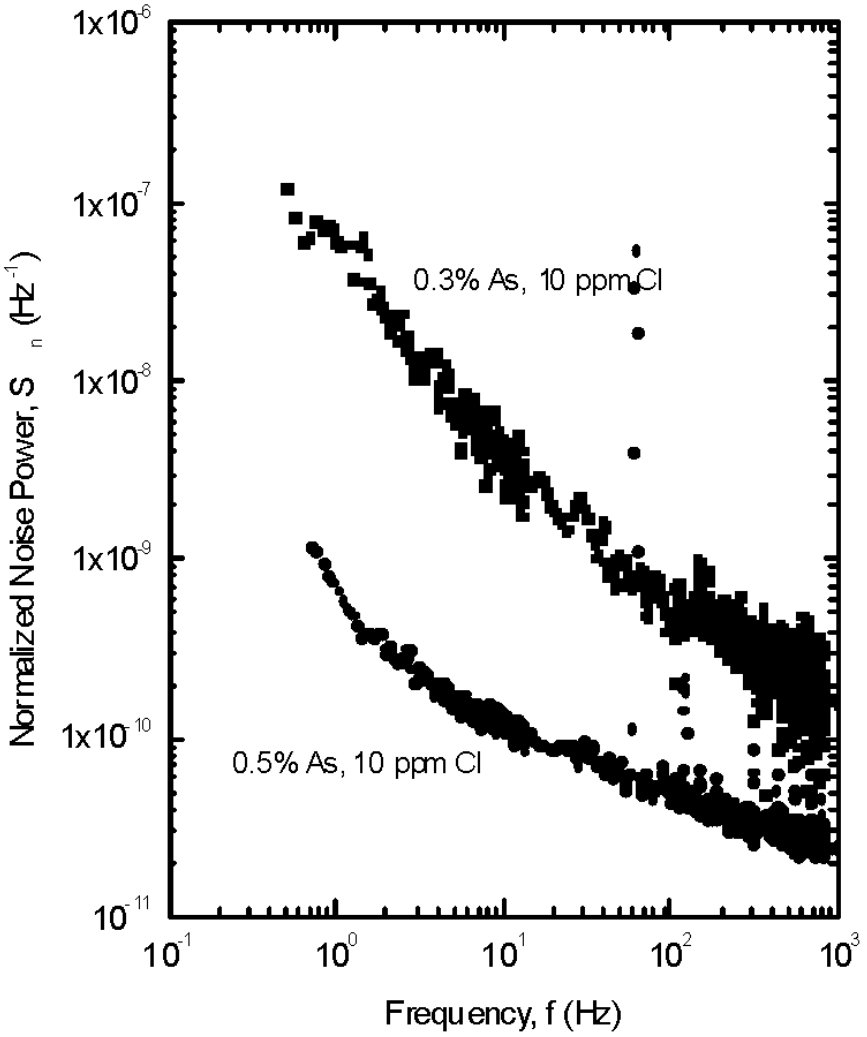

Figure 5.12: Normalized noise spectra of two different samples with variation in arsenic concentration keeping the chlorine concentration constant. Both the samples are 60 μm thick with gold top and bottom electrodes.

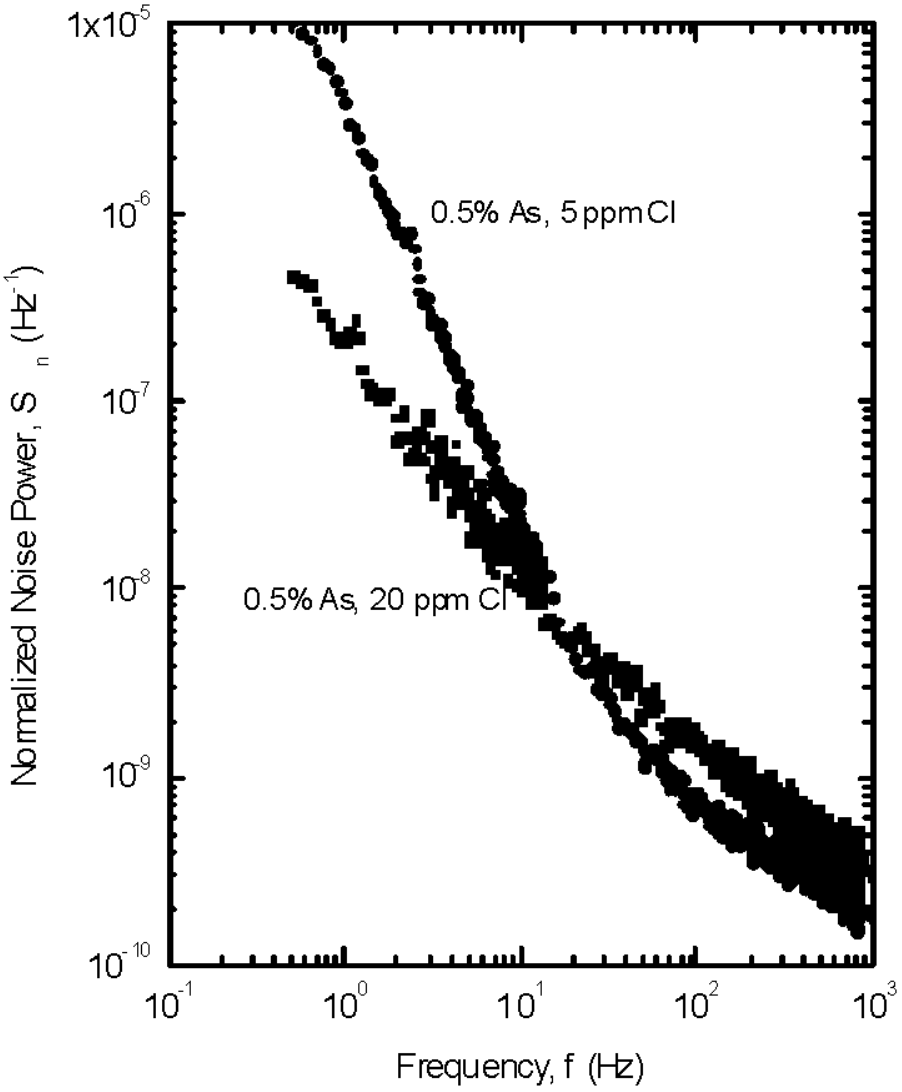

Figure 5.13: Normalized noise spectra of two different samples with the variations in chlorine concentration. Both the samples are 60 μm thick with gold top and bottom electrodes. Positive voltage were applied at the top electrodes.

The normalized noise spectra show that the change in chlorine concentration did not have much effect on noise power magnitude at higher frequencies but changed the slope of the spectra at lower frequencies. The excess noise for the 5 ppm Cl sample is due to random telegraphic type of noise that was produced by this sample which has a Lorentzian type of spectra.

The addition of arsenic and chlorine change the bulk electronic properties of amorphous selenium in known and consistent ways. The dark current and the $1/f$ noise do not seem to change in such a consistent manner. The conclusion is again that it is not the bulk transport that is controlling the current or noise but rather another factor most likely at the interface. The alloying might influence the noise by modifying the interface, but the effect would then be indirect and theoretically difficult to model or understand.

5.4.6 Surface Effect

The results presented above hint that the metal-semiconductor interface is important for the noise. One way to further test the importance of the interface is to modify the surface. However, amorphous selenium is quite vulnerable to stress and in particular external mechanical stress causes crystallization. Therefore, care is required when physically modifying the surface. In order to modify the surface I tried several techniques. A mechanical polisher was not successful because the sample tended to break into pieces. The pieces that were polished to an acceptable degree crystallized. Mullin in her PhD thesis described several procedures to prepare amorphous selenium samples for TEM observations including polishing [79].

These procedures, however surely introduce enough mechanical stress to convert the amorphous state to a crystallized one.

Surface of one part of the sample has been roughened using a very fine (800 grade silicon carbide) sand paper with the least possible applied pressure on the surface area to make sure that the amount of strain does not initiate crystallization throughout the sample. In order to gently alter the surface I manually abraded the surface of a sample by applying the least amount of stress possible to the selenium layer. The samples were then electroded with platinum and gold. Crystallization can be detected by a substantial increase in the conductivity. The dark conductivity was monitored for a long period of time, typically 5 to 6 weeks and no significant change was observed.

Figure 5.14 illustrates normalized noise spectra measured at two different types of surfaces. To ensure that all other parameters remain the same including the deposition factors, only a part of one physical sample was abraded - the rest was left as deposited. A relatively thicker sample was chosen to ensure that the roughening does not significantly change the thickness of the amorphous selenium layer; the sample is 60 μm thick. Both top electrodes are gold and were deposited at the same time, one on the roughened area and one on the pristine surface. The roughened surface produced $1/f$ noise power about two orders of magnitude less than the as deposited surface. This result serves to emphasize the importance of the metal-selenium interface for the noise.

In order to confirm and investigate further the effect of surface condition on $1/f$ noise two further samples were prepared. Although not deposited at the same

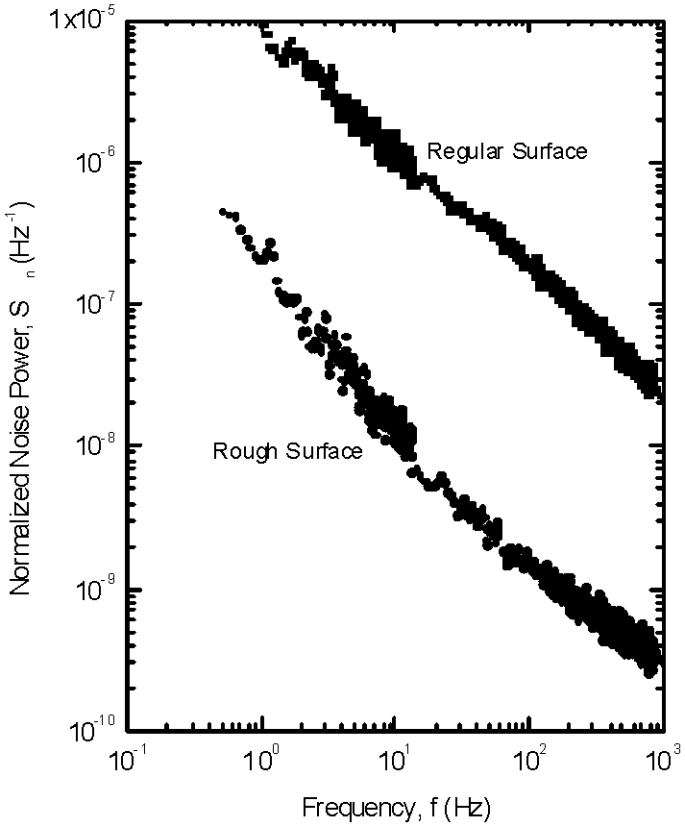

Figure 5.14: Normalized noise power spectra of a-Se sample with Rough surface and Regular as-deposited surface. One half of the top surface of the sample was roughened with 800 grade sand-paper and then both the top electrodes were deposited.

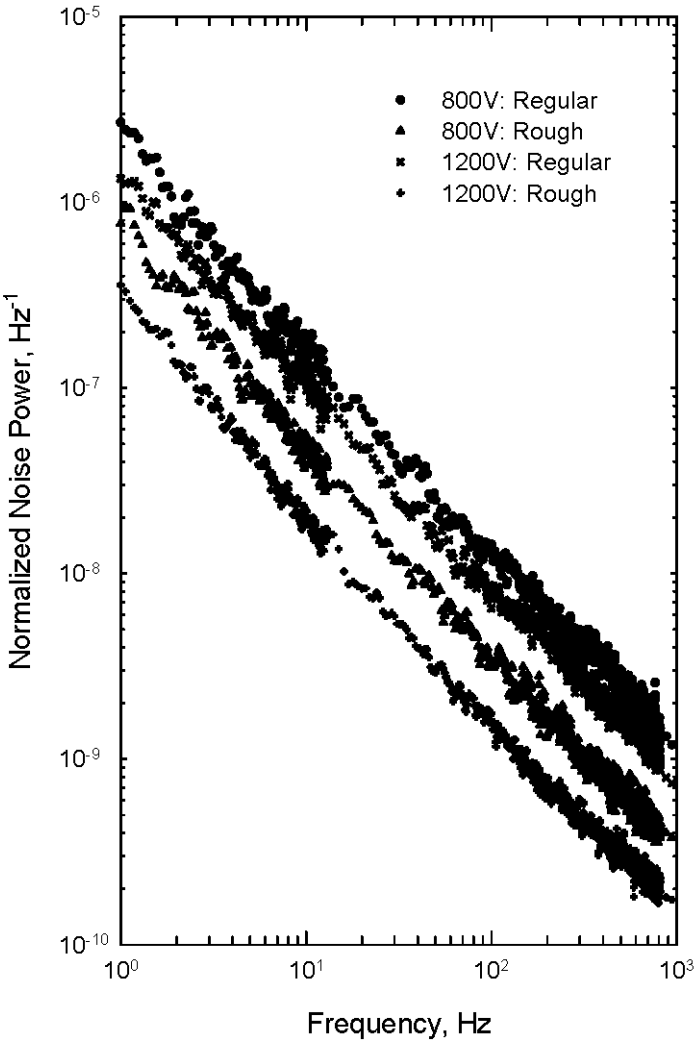

Figure 5.15: Normalized noise power with two different biasing voltages at two different surface conditions. In both the cases the surface conditions were altered with sand paper by applying the least possible stress on the surface to prevent further crystallization of the surface. Samples are 100 μm thick with both gold electrodes.

time, all deposition parameters were maintained the same for both samples. Again gold was used for the top electrodes. Part of the surface of both the samples were roughened in the same way as for the previous measurements. Unfortunately, one of the electrodes was damaged (which is what necessitated making two samples).

Noise spectra for the roughened and pristine surfaces at two bias voltages are shown in Figure 5.15. For both voltages, the rough surface produced less noise than that from the as deposited surface. However, the decrease was not as large as the previous sample. For the 1200 V biasing voltage, the magnitude of the noise spectra decreased by over a factor of four. Whereas at 800 V, the decrease was a factor of three. Notice that the shape of the spectra does not change with surface roughening, only the magnitude of the noise power.

5.5 Noise Behavior in Multilayer Structures

In order to reduce the flow of dark current through the device while under a biasing voltage, a multi-layered structure is used in the practical amorphous selenium based Flat Panel Detectors manufactured by ANRAD Corporation. Holes are the dominating carriers in a-Se devices. Blocking holes with the help of an extra n-like layer at the anode electrode helps to reduce the dark current while not affecting the device performance remaining almost unchanged. With this additional layer the device becomes an n-i layer device. A further reduction of dark current is achieved by adding a p-like layer deposited before the cathode electrode. With both the layers added to the intrinsic layer, the device structure becomes an n-i-p device. The n-i-p

device greatly reduces the dark current through the structure with a working applied voltage. The n- and p- layers are made by alloying the selenium with elements that create hole or electron traps respectively. Conventional doping like in silicon is not possible for selenium.

Multi-layered samples were provided by ANRAD, a company that produces the commercial FPD units used for X-ray imaging. The average dark current with these multilayered samples were in the range of pico-amperes (10^{-12} A). Noise measurement at this level of dark current is impossible with any current pre-amplifier presently available. To analyze the noise behavior, the devices were connected with a reverse dc voltage supply. Under such bias the multilayer devices produce a high level of dark current, in the range of micro-amperes (10^{-6} A).

Figure 5.16 shows the comparison between the magnitudes of normalized noise power in three different types of structures, a single i layer, i-n layer and p-i-n. In all three structures, the thickness of the intrinsic layer (i-layer) is 200 μm. The i-n layer contains a 6 μm thick n-like layer and the p-i-n device has and additional 2 μm thick p-like layer. The bottom electrodes are Indium-Tin-Oxide (ITO) and the top layers are Cr-Al. After deposition of the top electrodes a layer of parilene was deposited on the samples to increase their shelf-life.

As Figure 5.16 shows, the single intrinsic layer exhibits the largest magnitude of noise. Magnitude of the normalized noise power decreased almost four decades with the addition of the n-like layer and a further 1.8 decades for the p-i-n device. Both curves obtained from the multilayer structures change slope at around 50 Hz due to partial shot noise that occurs at the respective dark currents.

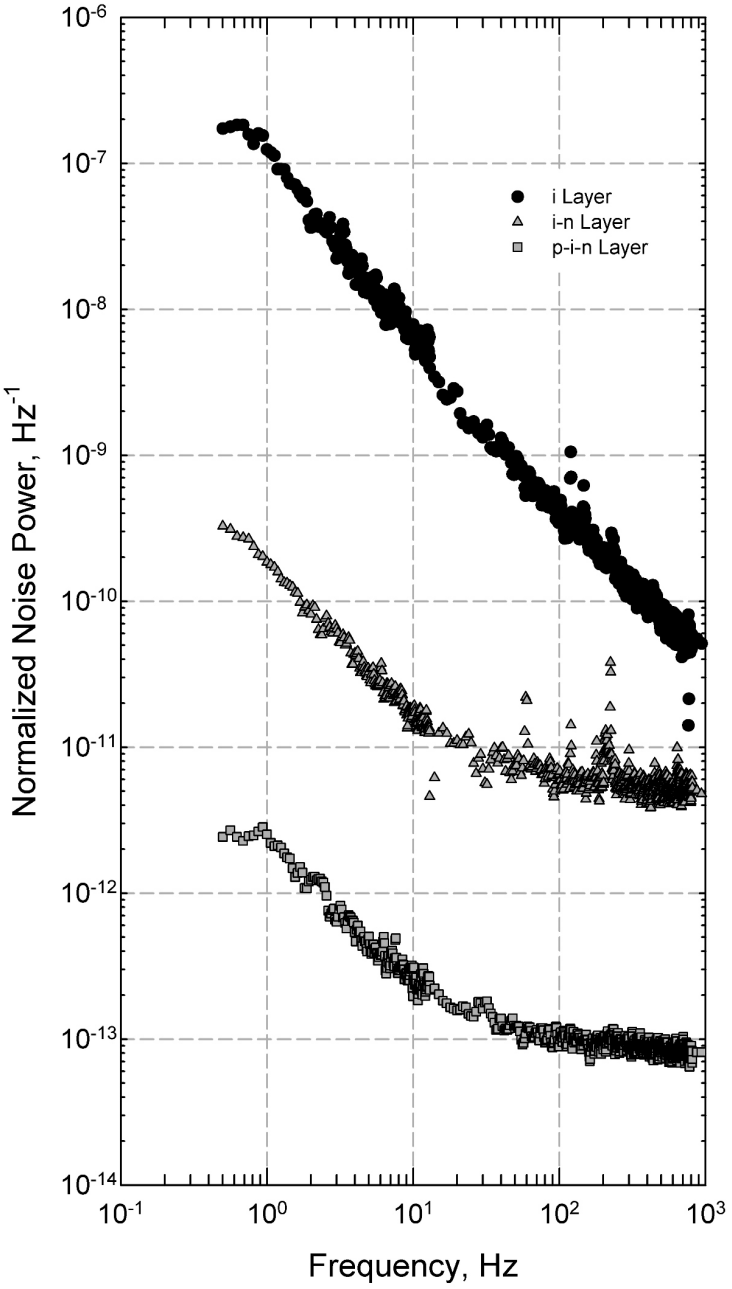

Figure 5.16: Normalized noise power spectral density showing the difference in magnitude at different types of multilayered structure. In all the samples the intrinsic a-Se layers are 100 μm thick. In the multilayered structures the top electrodes are made with aluminum and chromium, and the bottom electrodes are made with indium-tin-oxide (ITO). Positive voltages were applied at the top electrodes.

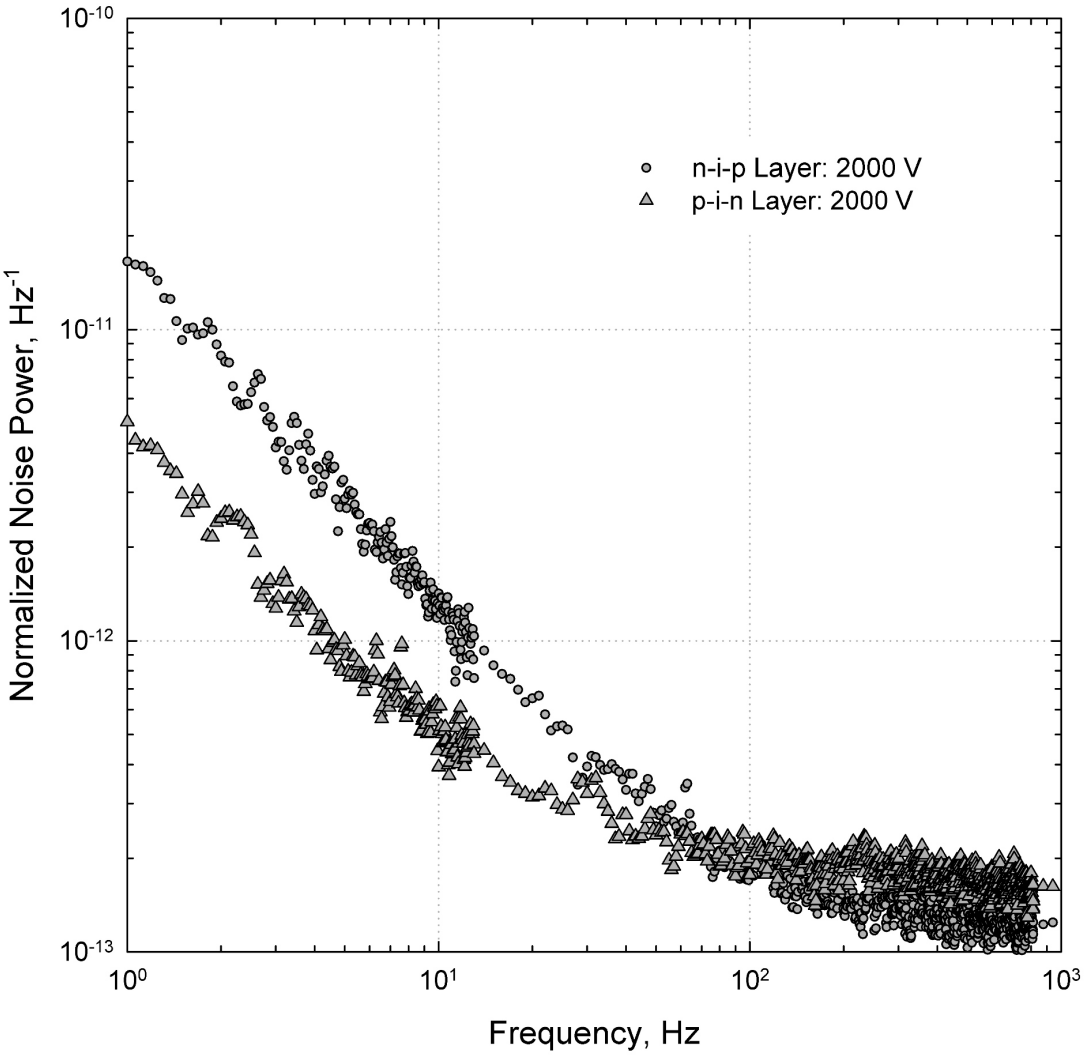

Figure 5.17: Normalized noise power spectral density plot of n-i-p and p-i-n structures. For the n-i-p structure, the top electrode is deposited on top of n-like a-Se layer and for the p-i-n structure, the top electrode is deposited on top of the p-like layer. Thickness of the intrinsic layer is approximately 200 μm, while the n- and p- like layers are less than 10 μm thick.

Figure 5.17 shows the normalized noise power spectral density plot of n-i-p and p-i-n structured devices. The difference between p-i-n and n-i-p is the order in which the layers are deposited; the first letter is the last deposited. Thickness of the intrinsic layers for both the structures is around 200 μm and the n-like layer is 6 μm, which is also the same for both the structures. p-like layer for n-i-p structure is 5 μm thick and that of p-i-n structure is 2 μm thick. Dark currents for n-i-p and p-i-n structures were 1.83×10^{-6} A and 1.7×10^{-6} A respectively. With 2000 V applied, the n-i-p device produced almost 4 times the noise power that the p-i-n device. A slight change in slope is also noticeable. The n-i-p layer produced $1/f$ noise with a slope of 1.11 while the slope of $1/f$ noise from p-i-n structure is 0.93. The curves are similar above 50 Hz due to the partial shot noise. Because the dark current is nearly the same, the shot noise level is also the same.

Figure 5.18 illustrates the levels of measured Johnson noise, measured excess noise and calculated shot noise. Excess noise data was obtained at 10 V/μm electric field while the shot noise was calculated for 1.83×10^{-6} A. In this figure it is quite evident that the bend in excess noise at 50 Hz cannot be due to the Johnson noise as its magnitude is far smaller, but the calculated shot noise is close to the measured noise in the flattish region above 200 Hz. Still the magnitude of this noise stays about three times below the calculated shot noise. This is the reason why instead of shot noise it is better to label it as a partial shot noise.

The dark current in the multilayer samples are much larger than in the single layer devices. Typically the dark current in a single layer device ranges around nano-amperes, whereas, dark current in the multilayer structures were in the micro-ampere

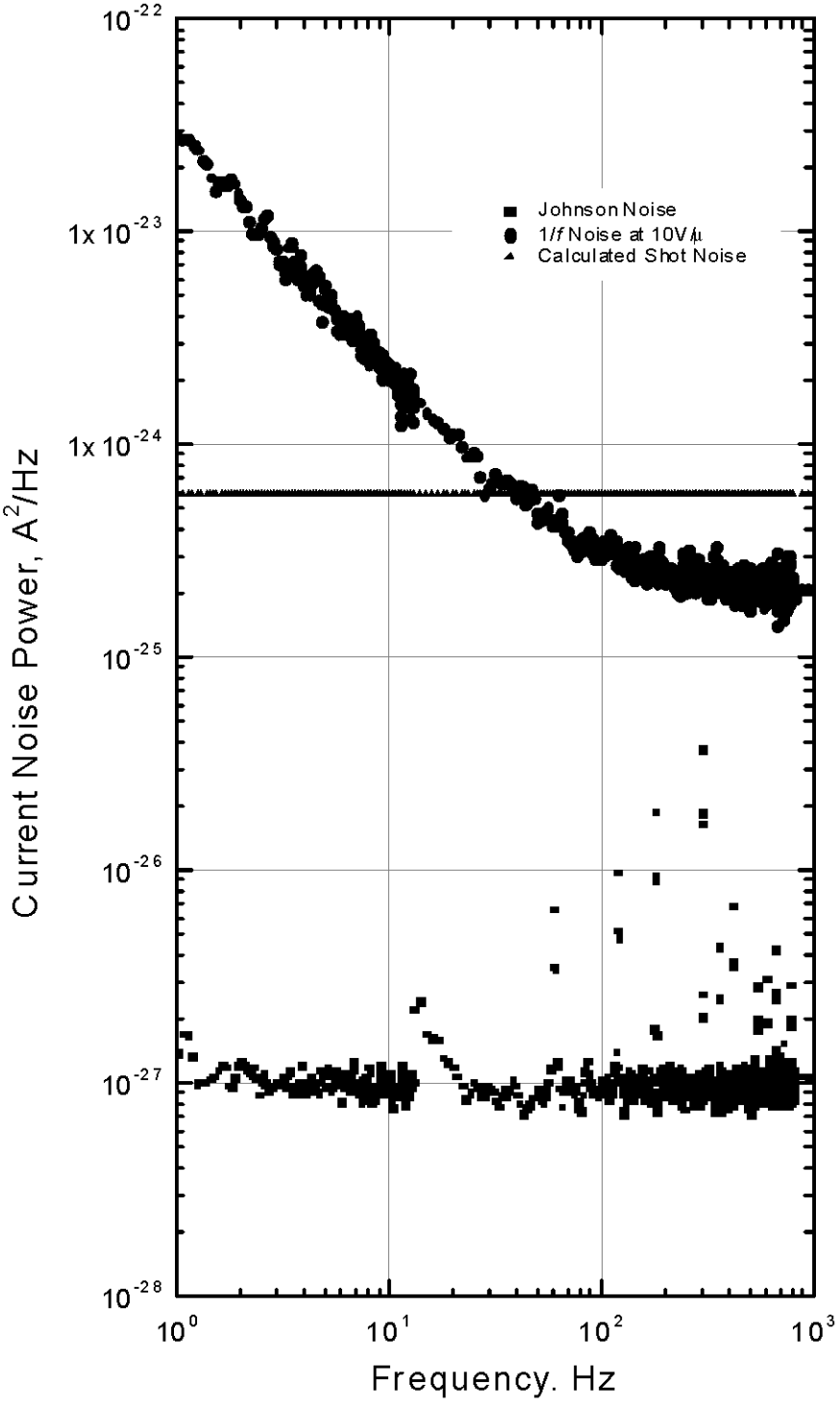

Figure 5.18: Plots of measured Johnson noise, measured excess noise and calculated shot noise for a multilayer sample. In this figure the sample is a p-i-n device.

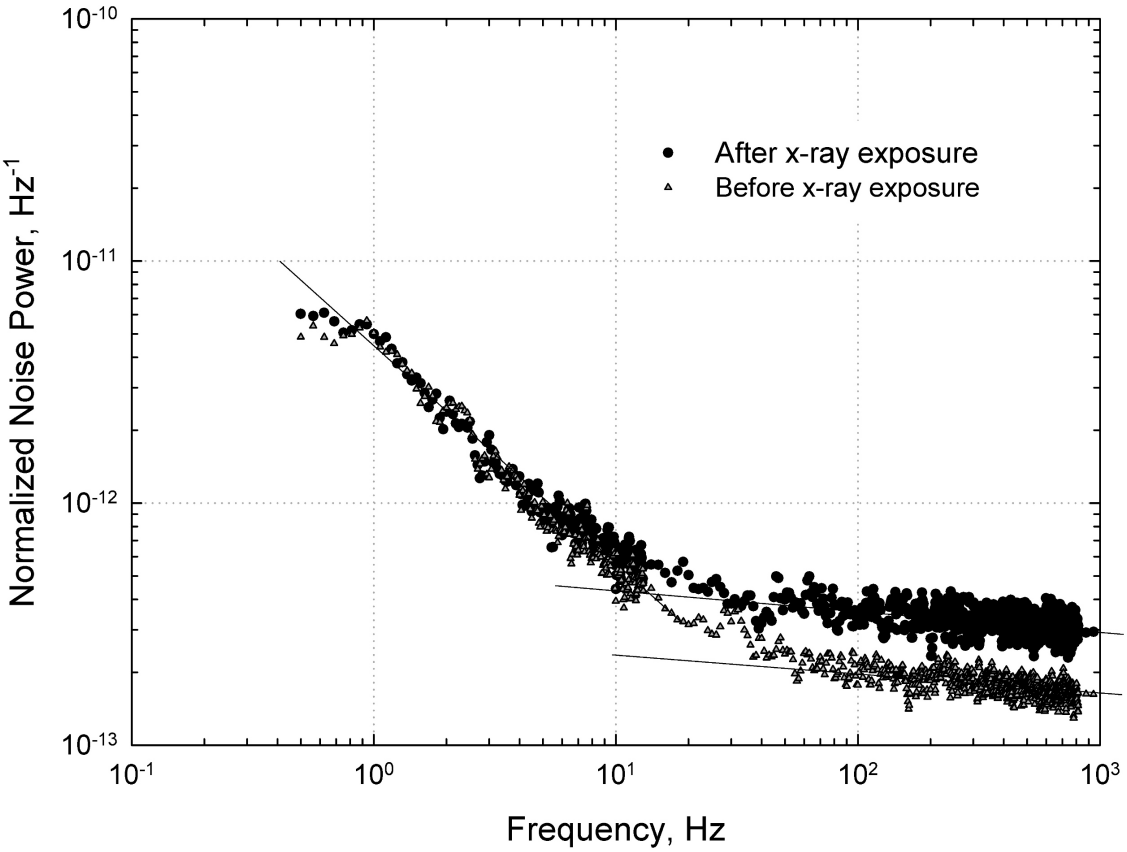

Figure 5.19: Normalized noise spectra of a p-i-n detector showing the effect of X-ray. 14 R of X-ray was exposed for a period of 5 minutes before the noise measurements were done.

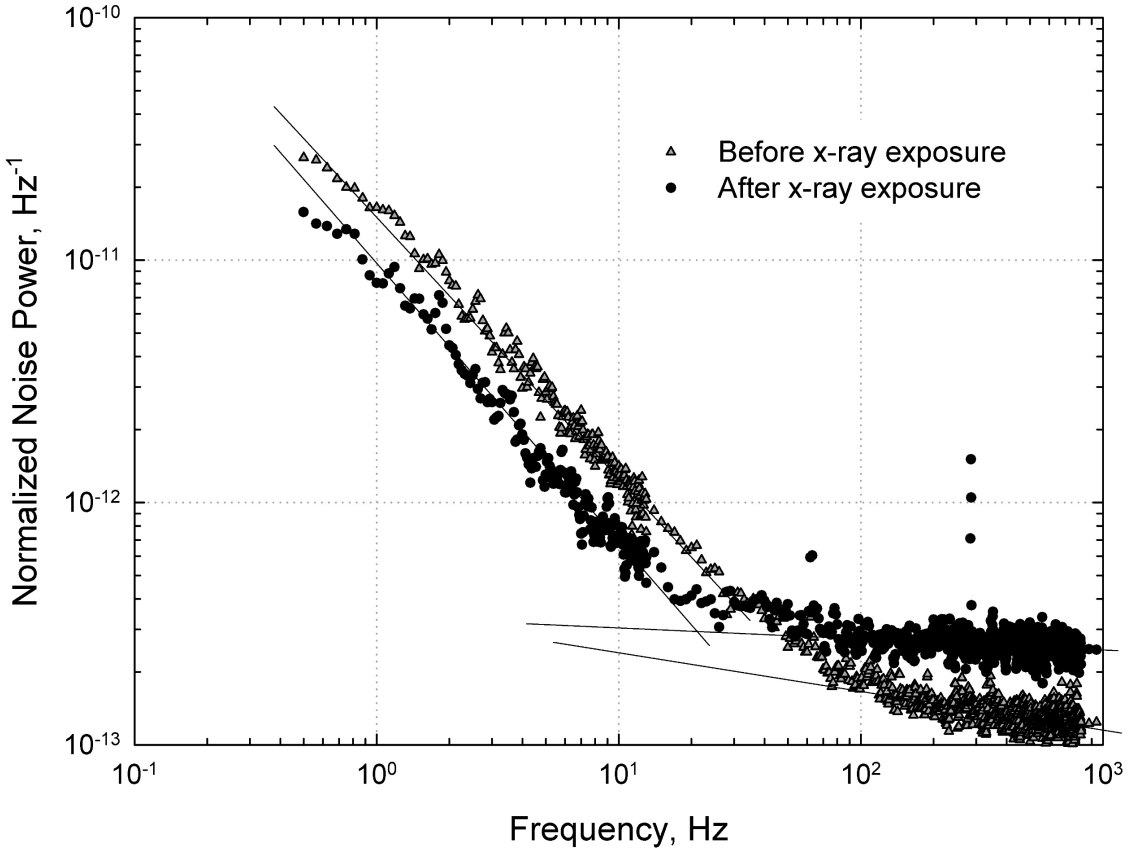

Figure 5.20: Normalized noise spectra of an n-i-p detector showing the effect of X-ray. 14 R of X-ray was exposed for a period of 5 minutes before the noise data were obtained.

range. Extra n-like or p-like layer were designed to trap the holes and electrons respectively. But the n-like layers seem to enhance the injection of electrons while the p-like layers did the same for holes. Decrease of the normalized noise might have to do with the enhanced injection, limiting the influence of the metal-semiconductor interface. Measurement of noise might approach the intrinsic noise of the bulk a-Se. The above is speculations from the noise measurements, but it is reasonable.

The multilayer samples were also exposed to X-rays to see if such exposure would change the noise properties. Electron hole pairs (EHP) are generated when X-rays are exposed on the photodetector that increase the number of carriers in the conduction and valance bands, resulting in an increase in the conductivity. During the X-ray exposure, the device current increased about a factor of 10^3. After exposure the current returned to the dark value after a certain period of time typically tens of minutes. Figure 5.19 shows that the magnitude and the slope of normalized noise power did not show any change below 50 Hz whereas the X-ray exposure increased the partial shot noise level. Since the dark current after exposure was allowed to relax back to its original value before the noise was measured, it is not clear why the shot noise level should increase. However, there might be another source for this noise above 50 Hz that does depend on X-ray exposure.

The effects of X-ray exposure were investigated for a second multilayer sample, this time a n-i-p sample. The results for this sample differ from the previous one. Figure 5.20 shows that the normalized noise power magnitude below 50 Hz decreases with X-ray exposure, $1/f$ noise dominates over the partial shot noise for these frequencies. The slope, however, remains almost the same before and after

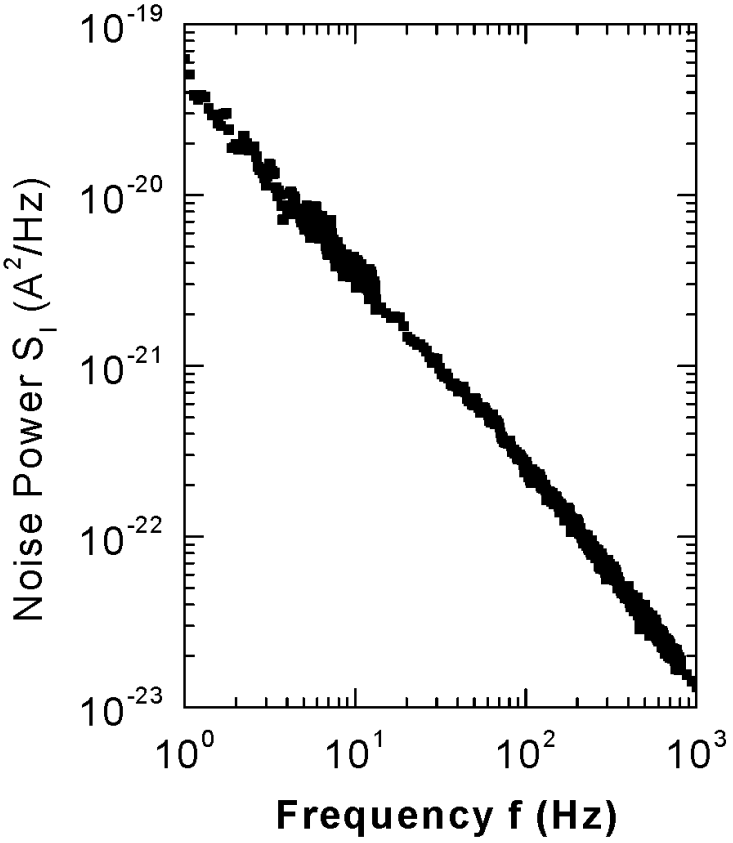

Figure 5.21: Noise power spectral density of a sample where the dark current is 192 nA. The sample is 60 μ thick with aluminum top and bottom electrodes.

X-ray exposures. Similar to the p-i-n structure, the partial shot noise became higher after the sample was exposed to X-rays.

5.6 Calculation of $1/f$ Noise Power

The total power in a pure $1/f$ noise signal is infinite. But the power over a given bandwidth is finite and serves as a measure of the magnitude of the noise. A calculation of the amount of power as a percent of the total dark current from

an arbitrarily chosen sample is shown in this section. The sample is 60 μm thick stabilized amorphous selenium with aluminum top and bottom electrodes. For an applied 400 V dc biasing the bias current was 192 nA. Over the frequency range 1 Hz to 1000 Hz the total noise power, shown in Figure 5.21 is

$$\therefore \int_{2\pi}^{2\pi\times 1000} S_I(\omega)d\omega = \int_{2\pi}^{2\pi\times 1000} \frac{c}{\omega}d\omega \tag{5.4}$$

where c is the noise power density at $\omega = 1$ rad/sec, ω_{max} and ω_{min} are the maximum and minimum frequency of measurement in radian respectively.

$$\begin{aligned} &= S_{I(\omega=1)} \left[\ln\left(\frac{\omega_{max}}{\omega_{min}}\right)\right] \\ &= 4\times 10^{-19} \left[\ln\left(\frac{\omega_{max}}{\omega_{min}}\right)\right] \\ &= 2.76\times 10^{-18} A^2 \end{aligned}$$

Hence, the integrated noise power is 2.8×10^{-18} A^2 for the measured frequency span. This amounts to fluctuations of about 1% in the average dark current.

5.7 SNR Calculations and the Detector Performance

This section shows an example of how the signal to noise ratio (SNR) of an actual detector can be calculated from the present work. Consider an integrating detector that has a fluctuating background signal - for example the dark current of an X-ray detector. The average background signal is removed by subtracting an initial integration without excitation from a second integration with excitation. Because of the fluctuations the background subtraction is not exact. The variance of the residual when the fluctuations have a $1/f$ spectrum, $S_I = S_o/f$ has been determined by T. Meyer [80] to be

$$\text{var} \simeq 8 S_o T_i^2 \ln 2 \tag{5.5}$$

where T_i is the integration time and assuming no delay between integrations. If the signal with excitation is βI_o where I_o is the dark current then the SNR is given by,

$$\text{SNR} = \frac{(\beta I_o)^2}{\text{var}} T_i^2 \tag{5.6}$$

For a typical chest X-ray the exposure and thus the integration time is 0.2 sec. Using the noise spectrum from Figure 5.21, $S_o = 4 \times 10^{-20}$ A^2/Hz and $I_o = 192 \times 10^{-9}$ A. Using these numbers the SNR of a detector made from this a-Se sample would be (20log β + 52)dB.

5.8 Summary

In this project experiments were undertaken to determine the nature of excess noise in amorphous selenium photodetector. Excess noise has been measured in different types of amorphous selenium samples including single layer and multilayer structures. Mostly the results are shown in normalized noise power plot so that the scaling with dark current is eliminated. In most samples the thickness of the amorphous selenium layer varied from 60μm to 200μm. In the first part of the chapter, excess noise of a single layered sandwich-type structure was presented using different types of metal contacts and different types of alloy compositions and various thicknesses of the bulk layer. Excess noise behavior was examined with the samples deposited at different substrate temperatures to observe how the number of trap centers controlled by the substrate temperature affects excess noise of the detector. Most of the temperature related experiments were limited by the low glass transition temperature of amorphous selenium. The influence of the surface was examined by cautious abrading the surface.

Excess noise in the multilayer structures was presented in the later part of this chapter. Both p-i-n and n-i-p samples were measured with similar results except that the slope of $1/f$ noise was 0.93 for p-i-n and 1.11 for n-i-p layer. X-ray exposures caused some change in the noise, especially the magnitude of noise power in the n-i-p structure.

Chapter 6

Summary and Conclusions

6.1 Goals

The primary objective of this research was to determine experimentally the behavior of excess noise in amorphous selenium that is used in Flat Panel Photodetectors. The secondary objective of this work was to try to determine the origin of the $1/f$ noise in the device. The $1/f$ noise in a-Se had not been reported previously and so there was no guidance as to what and how the noise would be present in a-Se. Indeed, the noise models of the a-Se X-ray detectors assumed Johnson or shot noise which we now know to be incorrect and on purpose of this work is to provide data for such modeling. The goals were largely met. Much experimental data was obtained which will be summarized below. The question of the origins of noise in any material or device is often difficult to answer. However, the data presented here points to the metal-semiconductor interface as the location which determines the noise.

6.2 Apparatus and Sample Preparation

Noise measurements in the a-Se samples are difficult because of the small bias currents. Typically the bias currents ranges between nano and pico amperes per square centimeter. In most of the noise measurements the noise currents remained within 1% of the bias currents. Measurements became even more difficult because of the longer current transients that occurred after each voltage was applied. Highly non-linear I-V characteristics complicated the noise analysis. Suitable apparatus was constructed to isolate the sample from external noise sources. Low-noise electronics were used so that the noise generated from the amplifiers does not affect the actual measurements.

With this equipment it is possible to obtain noise spectra from 500 mHz to 52 kHz, although depending on the sample, data could be obtained only to a lower frequency typically 1 kHz. Fluctuations as low as 10^{-13} A over the experimental bandwidth could be measured.

All the samples for the noise measurements except the multilayer samples were fabricated using the deposition facilities of the Electronic Material and Devices group at the University of Saskatchewan. Fabricating the sample in-house meant that samples could be quickly prepared and various parameters changed as necessary. Parameters that were altered included substrate temperature, alloy composition and metal of the electrodes.

Because a-Se relaxes significantly after deposition, samples were kept in the dark for 72 hours before measurements were made.

6.3 Results

Before the noise in the bias current can be measured, the I-V and I-t curves need to be determined. These curves are complicated for a-Se because of the long time transients and the non-linear current-voltage relation. Ideally noise should be measured with a constant bias current and this requirement necessitated a waiting period after the voltage was applied, at least five hours and in some cases up to 10 hours.

The noise I have measured is indeed $1/f^{\alpha}$ with α ranging from 0.77 to 1.4. Some samples showed single power law spectra and for these α was closer to one. Some samples showed more complicated noise spectra, including curvature and slope changes.

The effect of noise was investigated by changing various parameters of the a-Se samples. The results are not completely consistent but the metal of the electrode clearly has a large effect on both the magnitude and shape of the noise spectrum. Of the metals studied aluminum produced the least normalized noise and platinum the most, however, one must be aware that the currents for platinum electrodes are very small and the normalization factor is correspondingly large.

Alloy composition also had an effect showing a decrease in the normalized noise with the addition of arsenic. But chlorine had no effect on the magnitude of the noise spectra. The condition of the surface before the top electrode deposition also had a large effect on the magnitude of the normalized noise power. A roughened surface decreased the noise magnitude substantially. Investigation of samples with

different volumes showed that the noise does not scale with 1/V as it should. From these results, the conclusion is that the noise does not originate in the bulk of the amorphous selenium but is controlled by the contact interface region.

Indeed amorphous selenium is a "noisy" material. Since the noise appears to be generated at the interface, it is not meaningful to compare the noise power with that produced by other materials. Likewise it is not meaningful to compute a Hooge parameter for a-Se. However, as the calculation in chapter 5 showed, over a limited bandwidth of 1 kHz, the fluctuations for one sample amounted to 1% of the bias current. This level of noise is quite high.

The multilayered samples, n-i-p, proved quite interesting when in forward bias because the currents were substantially larger than for single layered samples and the normalized noise was substantially smaller. One possible explanation for these results is that the n and p layers are acting as carrier sources so that the current is not controlled by the metal interface. If correct then these measurement may be closer to the intrinsic noise of a-Se.

6.4 Suggestions for Future Work

Being the first report on the excess noise in amorphous selenium material, this work is surely an encouragement for researchers to study the noise characteristics more deeply and elaborately. In light of the experimental nature, this work has perhaps raised more questions than it has answered. I suggest the following avenues for additional theoretical and experimental research.

6.4.1 Other Metals Used as Electrodes

In this work the samples were prepared mostly with platinum, gold or aluminum electrodes, mainly because these are used in devices. Some metals such as silver and copper cannot be used because of electro-migration, but a more systematic study using a variety of metals would be useful especially to determine if there is a trend of the noise with work function, or to investigate those metals known to for selenides such as cadmium.

6.4.2 Investigation of RTN

This work focused mainly on the $1/f$ noise. However, for several samples random telegraph noise was present. RTN is fundamentally different from $1/f$ noise and usually is due to a different mechanism. This type of noise, if it can be produced consistently in a-Se samples, deserves study.

6.4.3 Noise Measurement at Lower Frequencies

For certain samples, the bias current is too low to reliably measure the $1/f$ noise such as the reverse biased multilayered devices. However, $1/f$ noise increases at lower frequencies, so if the frequency range can be extended, it might be possible to measure at least the magnitude of the $1/f$ noise in these difficult multilayered samples.

6.4.4 Noise Measurement with X-ray Exposures

The noise was measured after the multilayered devices were exposed in X-ray for a certain period of time. More interesting would be the noise in the photocurrent produced during X-ray exposure. This noise is of obvious importance to the X-ray detector manufacturers. However, such experiments would require a continuous X-ray source and considerable reconfiguration of the current apparatus used in this project.

6.4.5 Metal-Semiconductor Interface

A better theoretical understanding of noise in a-Se depends on a better theory of the metal-semiconductor interface. Further studies along of the interface are likely necessary before a true theory of noise in the a-Se samples can be developed.

References

[1] M. J. Yaffe and J. A. Rowlands, "X-ray detectors for digital radiology", *Physics of Medical Biology*, vol. 42, pp. 1–39, 1997.

[2] S. O. Kasap and J. A. Rowlands, "Direct conversion flat panel x-ray image detectors", *IEE Proceedings Circuits, Devices and Systems*, vol. 149, no. 2, pp. 85–96, 2001.

[3] G. S. Belev, *Electrical properties of amorphous selenium based photoconductive devices for application in X-ray image detectors*, PhD thesis, University of Saskatcheawn, January 2007.

[4] I. Blevis, D. Hunt, and J. Rowlands, "Measurement of X-ray photogeneration in amorphous selenium", *Journal of Applied Physics*, vol. 85, pp. 7958, 1999.

[5] M. H. Brodsky, *Amorphous Semiconductors, Topics in Applied Physics*, vol. 36, chapter 5, pp. 113–158, 2nd edition.

[6] J. A. Rowlands and S. O. Kasap, "Amorphous semiconductors usher in digital X-ray imaging", *Physics Today*, vol. 50, pp. 24–30, 1997.

[7] A. Varshneya, *Fundamentals of inorganic glasses*, Boston Academic Press, 1994.

[8] M. J. Buckingham, *Noise in Electronic Devices and Systems*, Market Cross House, EllisHorwood, 2nd edition, 1983.

[9] S. O. Kasap and J. A. Rowlands, *Optoelectronics and Photonics: Principles and Practices*, chapter X-ray photoconductors and stabilized a-Se for direct conversion digital flat panel X-ray image detectors, Prentice-Hall, Upper Saddle River, New Jersey, cd rom edition, 2001.

[10] M. Z. Kabir, *Modeling of X-ray photoconductors for X-ray image detectors*, PhD thesis, University of Saskatchewan, August 2005.

[11] J. A. Rowlands and J. Yorkston, "Flat panel detectors for digital radiography", *Handbook of Medical Imaging*, vol. 1, 2000.

[12] S. O. Kasap, *HandBook of Imaging Materials*, chapter Photoreceptors: the selenium alloys, pp. 329–372, Mercel Dekker, New York, 1991.

[13] S. O. Kasap, C. Haugen, M. Nesdoly, and J. A. Rowlands, "Properties of a-Se for use in flat panel X-ray image detectors", *Journal of Non-Crystalline Solids*, vol. 266-269, pp. 1163, 2000.

[14] R. A. Street, S. E. Ready, K. V. Schuylenbergh, J. Ho, J. B. Boyec, P. Nylen, K. Shah, L. Melekhov, and H. Hermon, "Comparison of PbI_2 and HgI_2 for direct detection active metrix x-ray image sensors", *Journal of Applied Physics*, vol. 91, pp. 3345–3355, 2002.

[15] G. Zentai, L. Partain, R. Pavlyuchkova, C. Proano, A. Taieb B. N. Breen, O. Dagan, M. Schieber, H. Gilboa, and J. Thomas, "Mercuric iodide medical imagers for low exposure radiography and fluoroscopy", *Proceeding of SPIE*, vol. 5368, pp. 200–210, 2004.

[16] Y. Eisen and A. Shor, "CdTe and CdZnTe room-temperature X-ray and gamma ray detectors and imaging systems", *Mat. Res. Soc. Symposium Proceedings*, vol. 487, pp. 129–144, 1997.

[17] F. N. Hooge, "$1/f$ noise is no surface effect", *Physics Letters*, vol. 29A, pp. 139, 1969.

[18] F. N. Hooge, "Discussion of recent experiments on $1/f$ noise", *Physica*, vol. 60, pp. 130, 1976.

[19] J. Mort, *The anatomy of xerography: Its invention and evolution*, McFarland and Company, 1989.

[20] M. Cutler, *Liquid Semiconductors*, chapter 1, pp. 113–158, Academic Press Inc., New York, 1977.

[21] M. Abkowitz, "Density of states in a-Se from combined analysis of xerographic potentials and transient transport data", *Philosophical Magazine Letters*, vol. 58, pp. 53–57, 1988.

[22] H. Z. Song, G. J. Adriaenssens, E. V. Emelianova, and V. I. Arkhipov, "Distribution of gap states in amorphous selenium thin films", *Physical Review B*, vol. 59, pp. 10607–10613, 1999.

[23] S. O. Kasap and J. A. Rowlands, "X-ray photoconductors and stabilized a-Se for direct conversion digital flat panel X-Ray image-detectors", *Journal of Materials Science: Materials in Electronics*, vol. 11, pp. 179, 2000.

[24] L. Benkhedir, M. S. Aida, and G. J. Adriaenssens, "Defect levels in the band gap of amorphous selenium", *Journal of Non-Crystalline Solids*, vol. 344, pp. 193–198, 2004.

[25] L. Benkhedir, M. Brinza, and G. J. Adriaenssens, "Electronic density of states in amorphous selenium", *Journal of Physics: Condensed Matter*, vol. 16, pp. S5253– S5264, 2004.

[26] N. Qamhieh, M. K. Benkhedir, M. Brinza, J. Willeken, and G. J. Adriaenssens, "Steady-state photoconductivity in amorphous selenium glasses", *Journal of Physics: Condensed Matter*, vol. 16, pp. 3827–3833, 2004.

[27] K. Koughia, Z. Shakoor, S. O. Kasap, and J. M. Marshall, "Density of localized electronic sates in a-Se from electron time-of-flight photocurrent measurements", *Journal of Applied Physics*, vol. 97, pp. 033706–1–033706–11, 2005.

[28] J. Marshall and A. Owen, "Drift mobility studies in vitreous arsenic triselenide", *Philosophical Magazine*, vol. 24, pp. 1281–1290, 1971.

[29] K. Koughia, B. Fogal, G. Belev, R. Johanson, and S. Kasap, "Density of states in the mobility gap of stabilized a-Se from electron time-of-flight photocurrent analysis", *Journal of Non-Crystalline Solids*, vol. 338-340, pp. 569–573, 2004.

[30] E. Emelianova, M. Benkhedir, M. Brinza, and G. Adriaenssens, "Analysis of electron time-of-flight photocurrent data from a-Se", *Journal of Applied Physics*, vol. 99, pp. 083702–1 – 083702–4, 2006.

[31] H. Naito, T. Iwai, M. Okuda, T. Matsushita, and A. Sugimura, "Computer simulation study of tail state distribution in amorphous selenium", *Journal of Non-Crystalline Solids*, vol. 114, pp. 112–114, 1986.

[32] A. R. Bulsara and L. Gammaitoni, "Tuning in to noise", *Physics Today*, vol. 49, no. 3, pp. 39–45, March 1996.

[33] T. M. Chen and A. M. Yassine, "Electrical noise and VLSI interconnect reliability", *IEEE Transactions on Electron Devices*, vol. 41, pp. 2165–2172, 1994.

[34] L. K. J. Vandamme, "Noise as a diagnostic tool for quality and reliability of electronic devices", *IEEE Transactions on Electron Devices*, vol. 41, pp. 2176–2187, 1994.

[35] B. J. Jones, "Low-frequency noise spectroscopy", *IEEE Transactions on Electron Devices*, vol. 41, pp. 2188–2197, 1994.

[36] S. B. Alexander, "Optical communication receiver design", *SPIE, OP*, 1997.

[37] A. Einstein, "Investigations on the theory of, the brownian movement", *Annalen der. Physik*, vol. 19, no. 4, pp. 371–381, 1906.

[38] J. B. Johnson, "Thermal agitation of electricity in conductors", *Physical Review*, vol. 32, no. 1, pp. 97–109, 1928.

[39] H. Nyquist, "Thermal agitation of electric charge in conductors", *Physical Review*, vol. 32, pp. 110–113, 1928.

[40] H. W. Ott, "Noise reduction techniques in electronics system", *Bell Telephone Lab.*, 1976.

[41] R. Sarpeshkar, T. Delbruck, and C. A. Mead, "White noise in MOS transistors and resistors", *IEEE Circuits Devices Mag.*, pp. 23–29, 1993.

[42] S. Kogan, *Electronic Noise and Fluctuations in Solids*, Cambridge University Press, Great Britain, 1996.

[43] F. R. Connor, *Noise*, Edward Arnold, London, 1979.

[44] J. B. Johnson, "The schottky effect in low frequency circuits", *Physical Review*, vol. 26, no. 1, pp. 71–85, 1925.

[45] B. Jacobson and J. G. Webster, *Medicine and clinical engineering: Physiological and clinical medicine*, Prentice Hall International Ltd, New Jersey, 1979.

[46] J. Selman, *The fundamentals of X-ray and radium physics*, Charles C Thomas Publisher, Illinois, USA, 1968.

[47] H. E. Johns and J. R. Cunningham, *The physics of radiology*, p. 732, Charles C Thomas Publisher, Springfields, USA, 1983.

[48] R. E. Johanson, M. Gunes, and S. O. Kasap, "Noise in hydrogenated amorphous silicon", *IEE Proceeding Circuits Devices and Systems*, vol. 149, pp. 68–74, February 2002.

[49] A. D'Amico, G. Fortunato, and C. M. V. Vliet, "Conductivity and noise in thin films of non-hydrogenated amorphous silicon thin films", *Solid State Electronics*, vol. 28, pp. 837–844, 1985.

[50] M. Baciocchi, A. D'Amico, and C. M. V. Vliet, "$1/f$ noise in amorphous silicon and hydrogenated amorphous silicon thin films", *Solid State Electronics*, vol. 34, pp. 1439–1447, 1991.

[51] J. Fan and J. Kakalios, "Conductance-noise fluctuations in hydrogenated amorphous silicon", *Physical Review Letters*, vol. 69, pp. 1097–1100, 1992.

[52] J. Fan, L. M. Lust, and J. Kakalios, "Conductance fluctuations in doped hydrogenated amorphous silicon", *Journal of Non-Crystalline Solids*, vol. 164-166, pp. 469, 1993.

[53] R. E. Johanson, D. Scansen, and S. O. Kasap, "$1/f$ conductance noise in n-type amorphous silicon", *Philosophical Magazine B*, vol. 73, pp. 707–714, 1996.

[54] M. Tabak and W. Hillegas, "Preparation and transport properties of vacuum evaporated selenium films", *Journal of Vacuum Science and Technology*, vol. 9, pp. 387–390, 1971.

[55] S. O. Kasap and B. Polischuk, "Application of the interrupted field time-of-flight transient photoconductivity to investigate sample inhomogeneities", *Canadian Journal of Physics*, vol. 73, pp. 96–100, 1995.

[56] S. Vaezi-Nejad and C. Juhasz, "Electrical properties of amorphous semiconductor selenium and its alloys: II. heterojunction meltilayers", *Semiconductor Science and Technology*, vol. 3, pp. 664–674, 1988.

[57] H. G. E. Beck and W. P. Spruit, "$1/f$ noise in the variance of johnson noise", *Journal of Applied Physics*, vol. 49, pp. 3384–3385, 1978.

[58] R. E. Johanson, M. Gunes, and S. O. Kasap, "$1/f$ noise in hydrogenated amorphous silicon-germanium alloys", *IEE Proceeding Circuits Devices and Systems*, vol. 150, no. 4, pp. 345–349, August 2003.

[59] S. H. Majid and R. E. Johanson, "$1/f$ noise in an amorphous selenium photodetector", *IEEE Proceedings of CCECE 2005*, p. 2278, May 2005.

[60] S. H. Majid and R. E. Johanson, "$1/f$ noise in stabilized amorphous selenium", *Journal of Non-Crystalline Solids*, p. 352, April 2006.

[61] S. H. Majid and R. E. Johanson, "Studies on excess noise in stabilized amorphous selenium used in X-ray photodetectors", *Journal of Non-Crystalline Solids*, p. 354, March 2008.

[62] S. Malik, A. K. Ray, and S. Bruce, "$1/f$ noise in langmuir-blodgett films on silicon", *Semiconductor Science and Technology*, vol. 20, pp. 1, 2005.

[63] R. E. Johanson and S. O. Kasap, "$1/f$ noise of amorphous indium oxide", *Journal of Vac. Science Technology*, vol. 20, no. 4, pp. 1027, May/June 2002.

[64] F. Z. Bathei and J. C. Anderson, "Electrical noise measurements in intrinsic amorphous-silicon", *Philosophical Magazine B*, vol. 55, pp. 87, 1987.

[65] F. Z. Bathei and J. C. Anderson, "Flicker noise in hydrogenated amorphous-silicon schottky diodes", *Philosophical Magazine B*, vol. 57, pp. 129, 1988.

[66] S. O. Kasap, M. Gunes, R. E. Johanson, Q. Wang, J. Yang, and S. Guha, "Conductance fluctuations in a-Si:H: effects of alloying and device structure", *Journal of Material Science*, vol. 14, pp. 693, 2003.

[67] M. Gunes, R. E. Johanson, S. O. Kasap, F. Finger, and A. Lambertz, "Conductance fluctuations in VHF-PECVD grown hydrogenated microcrystalline silicon thin films", *Journal of Material Science*, vol. 14, pp. 731, 2003.

[68] D. Scansen, *Excess noise in n-type hydrogenated amorphous silicon*, PhD thesis, University of Saskatchewan, Electrical Engineering, 1996.

[69] C. Parman and J. Kakalios, "Nonlinear $1/f$ noise in amorphous silicon", *Physical Review Letters*, vol. 67, pp. 2229, 1991.

[70] C. Parman, N. E. Israeloff, and J. Kakalios, "Conductance fluctuations in doped hydrogenated amorphous silicon", *Physical Review B*, vol. 47, pp. 12578, 1993.

[71] S. Purkiss and R. A. Collins, "Switching and polarity-dependent memory effects in Se-SnO_2 and Se-In_2O_3 thin film devices", *Journal of Applied physics*, vol. 46, 1975.

[72] R. E Johanson, S. O. Kasap, J. Rowlands, and B. Polischuk, "Metallic electrical contacts to stabilized amorphous selenium for use in X-ray image detectors", *Journal of Non-Crystalline Solids*, vol. 227-230, pp. 1359, 1998.

[73] *CRC handbook on chemistry and physics.*

[74] R. A. Collins and G. Jones, "Evidence for metal-ion diffusion during memory-switching in thin selenium films", *Journal of Physics D*, vol. 11, pp. L13, 1978.

[75] A. I. Popov, I. K. H. Geller, and V. K. Shemetova, "Memory and threshold switching effects in amorphous selenium", *Physics Status Solidi*, vol. 44, pp. K71, 1977.

[76] N. B. Lukyanchikova, *Noise Research in Semiconductor Physics*, Gordon and Breach Science Publishers, 1996.

[77] H. Fiedler and H. R. Beilich, "Influence of the substrate temperature on the dielectric relaxation", *Phys. stat. sol.*, vol. 52, pp. K157, 1979.

[78] E. Montrimas and B. Petretis, "Influence of the substrate temperature on the dielectric relaxation", *Journal of Non-Crystalline Solids*, vol. 15, pp. 96, 1974.

[79] J. A. Mullin, *Viscous flow and structure relaxation in amorphous silicon and amorphous selenium thin films*, PhD thesis, Harvard University, June 2000.

[80] T. Meyer, "$1/f$ noise and integrating detectors", *To be published*, 2009.